MICROFLUIDIC TECHNOLOGY FOR INTEGRATED THERMAL MANAGEMENT: MICROMACHINED SYNTHETIC JET

A Thesis

Presented to

The Academic Faculty

by

Yong Wang

In Partial Fulfillment

Of the Requirements for the Degree

Doctor of Philosophy in Chemical & Biomolecular Engineering

Georgia Institute of Technology

November 2003

MICROFLUIDIC TECHNOLOGY FOR INTEGRATED THERMAL MANAGEMENT: MICROMACHINED SYNTHETIC JET

Approved by:

Sue Ann Bidstrup, Committee Chair

Mark G. Allen

Dennis W. Hess

J. Carson Meredith

Marc K. Smith

Date Approved 11/11/03

ACKNOWLEDGEMENTS

There are many people that I must thank for their assistance with the investigation in this thesis. First of all, I would like to express my deepest gratitude to my advisors Dr. Sue Ann Bidstrup and Dr. Mark Allen for guiding me through the journey. Without their true mentoring and insightful suggestions, I would not have been able to complete this work. This gratitude is also extended to my committee members Dr. Dennis Hess, Dr. Carson Meredith, and Dr. Marc Smith for their useful suggestions.

I would like to acknowledge Dyneon for providing the fluoroelastomers used in this study. I would also like to express my sincere appreciation to Dr. Ari Glezer for his guidance of fluid mechanics and synthetic jets. Without his assistance and access to his laboratory of flow characterization equipment, this research could not have been completed. In particular I would like to thank the research engineers in Dr. Glezer's group, John Culp, Jelena Vukasinovic, Dr. Raghav Mahalingam, for their assistance with data collection and equipment training. Without their willingness to set their work aside and spend their time in the lab collecting my data, this work would have remained incomplete. A note of thanks also goes to Shuo Li, a PhD student from Dr. Smith's group, for helpful discussions on the computational fluid mechanics simulation.

I would like to thank all the past and current members of the Bidstrup and Allen groups for their friendship and support. A special note of appreciation goes to Dr. Guang Yuan and Yong-Kyu Yoon for their advice and assistance in this research project over the years. I also owe my thanks to Kimsey Pollard for solving my computer woes.

Most importantly, I must thank my parents and my wife, Hongyi Dang, for their love and support throughout my graduate school ordeal. My father Yunting Wang and my mother Jinjun Wang have always been there to encourage me and assist me when I need it. I owe all of my success in life to them. My wife Hongyi Dang always believes in me, stands by me and motivates me. Thanks to you all.

Finally, the financial support of the DARPA is also gratefully appreciated.

TABLE OF CONTENTS

LIST OF TABLES

LIST OF FIGURES

SUMMARY

This work presents the use of organic multilayer lamination of epoxy-glass printed wiring board material to produce microfluidic structures, and the exploitation of these structures along with integrated drivers to develop a synthetic-jet-based integrated cooling solution for electronic systems. Thermal management of electronic systems becomes more complex as the density and the compactness of the system increases. Traditional methods of cooling, such as fan/heat sink combinations, either become inadequate to remove the generated heat fluxes or are incompatible with the compact, low-profile design. Recently, synthetic jets have been suggested as alternatives for cooling of electronics systems.

Synthetic jets are formed when a rigid-wall cavity is bounded on one side by a flexible membrane and on the other side by an orifice. The vibration of the membrane results in the alternating entrainment and expulsion of air into and out of the cavity through the orifice hole, resulting in a directional jet emitted from the orifice. Due to the small-scale of vortical structures of the jet, enhanced heat transfer over that available from fans is possible. In addition to the higher heat transfer coefficients available from synthetic jets, they have the capability to be fabricated in a low-profile format.

This process has been combined with the synthetic jet to produce an active cooling substrate (ACS), in which the jet driver, ducting, and outlet ports for chip cooling are integrated in the thickness of the printed wiring board substrate. The electromagnetic actuator, which consists of a permanent magnet and a voice coil, is used to vibrate the laminated polymeric corrugated diaphragm. The driver is in fluidic communication with

a duct and orifice outlet formed in the printed wiring board during lamination by the process described above. To form a thermal testbed, a microfabricated silicon heater/sensor chip is integrated on the printed wiring board using standard packaging techniques.

Two prototypes of ACS devices, vertical and tangential, are developed. The fluid mechanics and thermal performance of these devices are characterized. A computational fluid mechanics software, Fluent, is employed to explore the synthetic jet fluid mechanics and heat transfer problem from the numerical solution perspective. These models provide a better understanding of the fluid physics and enable good predictions of the relationship between fluid mechanics and heat transfer. Based on the experimental and simulation results, a sophisticated methodology is developed for future engineering analysis to design new synthetic-jet-based microjet devices with optimal geometries to fulfill different application requirements.

Chapter 1

INTRODUCTION

Thermal management of electronic systems is of increasing concern as transistor density and power consumption increase. Typical thermal management solutions are modular in nature; e.g., a heat sink and/or fan area added to a heat-producing part. In this work, an integrated solution, the active cooling substrate (ACS) is proposed, in which the cooling functionality is included in the printed wiring board alongside the electrical wiring. The mechanism for cooling involves the use of synthetic jets embedded in the substrate. The utility of the active cooling substrate is demonstrated through quantitative measurements of the thermal performance of the instrumented platinum heater testbeds. Thermal management is enhanced through the additional heat convection mode introduced by the embedded synthetic jets in the active cooling substrate.

1.1 Thermal Management in Microsystem Packaging

Microsystem packaging plays an important role in the microelectronics industry. Without innovative packaging, the revolutionary advances taking place in integrated circuits (ICs) design and fabrication will be lost. Packaging provides the mechanical support and the environmental protection required by ICs. To function, electrical circuits must be supplied with electrical energy which is consumed and converted into thermal energy (heat). Because all circuits operate best within a certain temperature range, the packaging must provide an adequate means of heat removal.

When designing integrated circuitry, "zero real estate and zero power supply" are two major targets. Of course, the two "zeros" are impossible to be realized in practice. However, they do reflect the future trends in the microelectronics industry-compactness and low power. Compactness means more functional units are packed in a smaller area which results in the shrinkage of the device footprint. A low power supply means less power is consumed by the device which leads to a longer lifetime for batteries and to less heat generation. However, some functions may be suppressed due to a lower power supply. As an example, the clock frequency of a digital circuit may be reduced as the power supply is decreased. Therefore, there may be a limit on further reduction of the power supply. On the other hand, advanced fabrication technologies and more functionality demands are still pushing forward the system integration from large scale integration (LSI) to very large scale integration (VLSI), until today's ultra large scale integration (USL), and from single chip modules (SCM) to multi-chip modules (MCM). Thus, the net result is higher power density on chip. For example, Intel is still following the roadmap according to Moore's law (Moore, 1965), the doubling of transistors per square inch on integrated circuits every couple of years. The transistors on lead Intel microprocessors double every two years, the die size grows by 14% every two years, and the frequency doubles every two years. In terms of power consumption, the past 486 processor is about 2 Ws, the current Pentium processor is about 100 Ws, and the future processor in the year of 2008 is expected to be 10000 Ws (Gelsinger, 2001). Figure 1 presents an evolution summary of the heat-flux demands for a wide range of applications, from the hand-held equipments to high performance mainframes and supercomputers (Tummala et al., 1997). Hence, modern microeletronics thermal management is facing

considerable challenges in the wake of miniaturizing of components leading to higher demands on net heat flux dissipation.

As the chip power increases, its power distribution which is generated from local units is non-uniform due to difference in local functionality and switching activity. The non-uniformity of the power distribution adds additional challenges to thermal management. Hot spots inside the integrated chip eventually can cause unrecoverable changes in their electrical characteristics. The clock can be skewed due to performance variations in the buffer devices as chip temperature varies. The timing inaccuracy between units can be induced by temperature dependent device characteristics and parasitic component value changes. The temperature dependent electromigration issue in interconnects and contacts and mechanical failure in interconnects and packaging can also arise from the non-uniform temperature distribution. As another example, the high-power laser device, vertical-cavity surface-emitting laser (VCSEL) array, has increased diode laser wavelength with an increase in temperature. To have a high overall optical conversion efficiency, the temperature must be quite uniform throughout the diode array. The isothermality and temperature control allow the maintenance of a precise laser wavelength, high output efficiency and lower thermally induced stresses. Therefore, it is important to accurately consider the temperature gradient issues and eliminate hot spots on the chip surface.

Thermal overstressing is by far the most common cause of failure in modern electronic systems. In electronic packaging, the major causes of electronics failures can be generally divided as follows: 55% due to temperature, 20% due to vibration, 19% due to humidity and only 6% due to dust (Chiriac et al., 2001). Hence, the probability of

failure in electronic components is strongly dependent on the operating temperature. Efficient removal of heat from today's highly integrated ICs remains a major bottleneck (Tummala et al., 1997). There is a strong need to improve the current capabilities in thermal management and electronic cooling.

1.2 Cooling Techniques

In the past, a variety of cooling techniques have been developed to enhance heat transfer in the all three modes (i.e. conduction, convection and radiation). Thermal management of electronic systems can be divided into three primary stages of heat transfer between the integrated circuits and the environment into which the heat is ultimately rejected. The first stage is the local conduction path between integrated circuits and the surface of the package within which they are embedded. The second stage is the cooperative thermal management of the heat flux from a number of individual packages within the enclosure of an entire instrument. Finally, the third stage is the global rejection of heat to the ambient across the system enclosure. While the first stage is heat conduction limited, the latter two stages are dominated by heat convection (and to a lesser extent by radiation). Thus, thermal management technologies can be divided into two categories: (1) technologies for enhancement of heat conduction to overcome the thermal resistance between integrated circuits and the surface of their packages (e.g. thermoelectric devices, micro refrigerators and micro heat pipes); (2) technologies for enhancement of heat transfer between the electronic package and the ambient, either across the package surface (e.g. heat sinks) or using a form of a heat exchanger (e.g.

micro channels, spray cooling, and heat pipes). The technologies in each category can be either "passive" such as heat sinks or "active" such as micro channels.

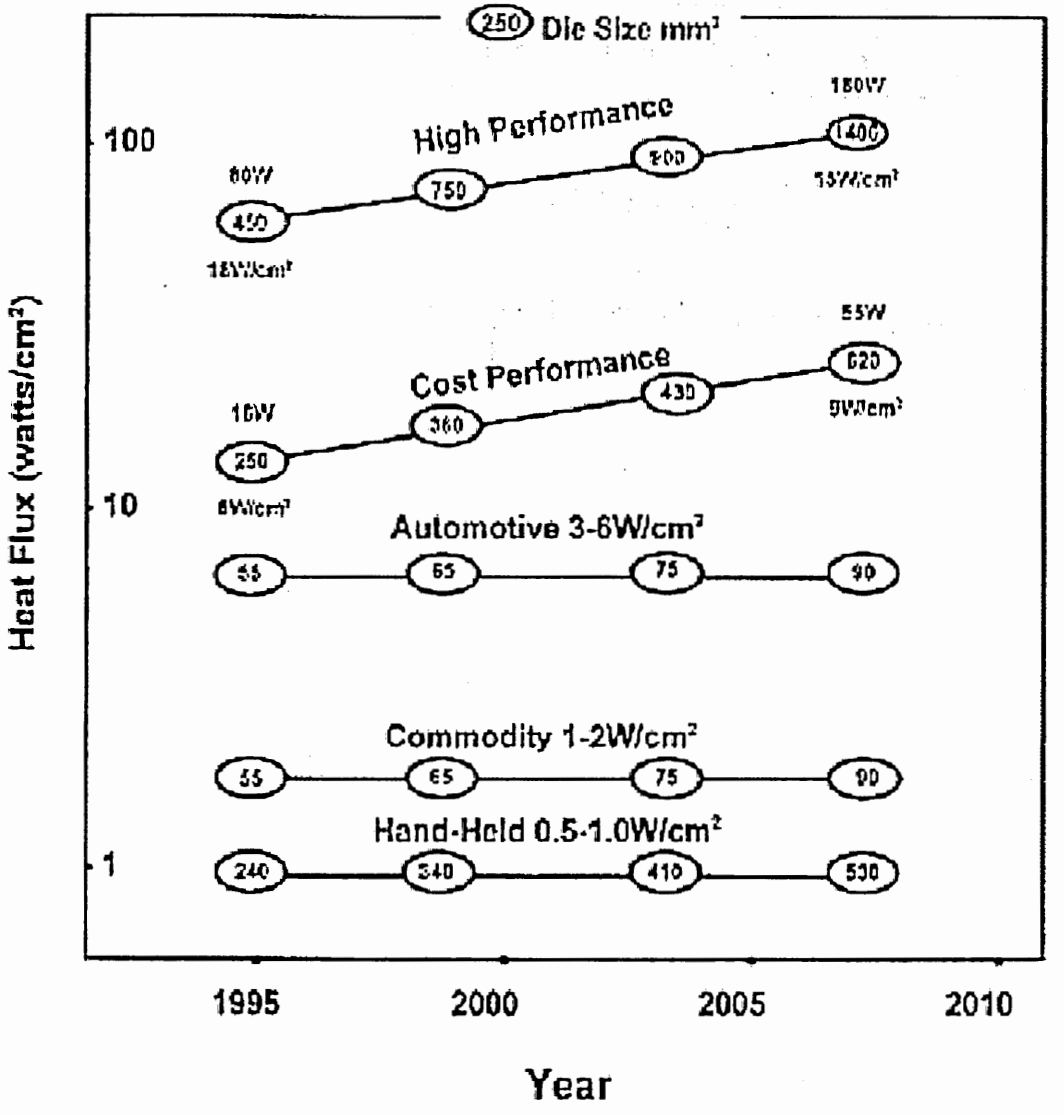

Figure 1. Evolution of the thermal-dissipation requirements

Fans are the common approach for cooling electronic equipment (Steinberg, 1991). There are four major types: propeller, tube axial, vane axial, and centrifugal blowers. These fans can be single phase, three phase, 60 cycles, 400 cycles, 800 cycle ac/dc, constant speed, variable speed, and flow rates from 1 cfm to several thousand cfm. The problems associated with fans include their low efficiency (e.g. about 80% for backward curved fan), loud noise and large size.

Thermoelectric devices such as InGaAs/InGaAsP superlattice thin film coolers have been integrated with InP p-i-n diodes to extract thermal energy from a heated stream (Fan et al., 2000). The advantage of these devices is that they can be fabricated on very small scales, and the power density is inversely proportional to the length of the thermoelectric leg. However, the operational efficiency of these devices is still an issue.

Micro-refrigeration involves the implementation of a full refrigeration flow cycle (Unger et al., 1996). The key component of this device is a micro-compressor that may be driven by an engine or externally supplied compressed air. One drawback of these devices is the need for external plumbing.

Micro-heat pipes are pipes which have been evacuated and, after a small amount of a working fluid has been inserted, are sealed (Steinberg, 1991). If heat is applied at the evaporator end, the fluid vaporizes and is transported almost instantaneously to the condenser end where the latent heat of vaporization is released as the vapor condenses back into liquid form. The liquid is then carried back to the evaporation end by capillary action. Therefore, no external power is needed for operation. Several important issues need to be addressed, including the formation of dry spots along the fluid path, the

critical balance between the opposing capillary and viscous forces, and the thermal resistance across the heat pipe enclosure where heat is absorbed and rejected.

Micro-channels are heat exchangers integrated in direct contact with the die (Sobhan et al., 2000). This technology increases the surface area for heat transfer and improves the heat transfer coefficient. However, this approach requires an external pump or compressor with plumbing and hence has a penalty associated with viscous losses. For a given channel characteristic cross-stream dimension and volume flow rate, these losses increase linearly with the channel length. This cooling technology also requires an efficient scheme for heat rejection to the ambient, which depends on the design and fabrication of a sophisticated heat sink.

Spray cooling relies on two-phase heat transfer within a closed-circuit flow system by spraying liquid droplets directly on a cluster of integrated circuits within a sealed enclosure (Wu et al., 1999). The flow circuit must include a pump, condenser, and control circuitry. The disadvantages of this technology are the complexity of the sealed liquid circuit, the device reliability, the cost, and the large power requirement to operate the cooling system.

Heat pipes operate on a closed two-phase cycle and have a heat transfer capacity that may be several orders of magnitude greater than the best solid conductors (Steinberg, 1991). Due to the relatively small thermal resistance of the heat pipe, its evaporator and condenser can be physically separated without causing a high temperature drop. Hence, heat pipes can operate in a nearly isothermal mode, while adjusting the evaporation rate to accommodate a wide range of power inputs and maintaining a relatively constant

source temperature. The main drawback of this technology is the possibility of liquid dry out in the pipe. In addition, some form of an airside heat exchanger on the condenser end is still needed.

Each cooling technology has its own strengths and weaknesses. When employed into a thermal management design, different application constraints and requirements need to be considered. Some common criteria for a thermal packaging are good compatibility with current packaging technologies, high efficiency, high reliability, low noise, low cost, and low power consumption. This research work proposes a micro electro mechanical system (MEMS) approach to realize pinpoint air spray cooling. This MEMS cooling device is based on synthetic jet technology.

1.3 Synthetic Jets

Synthetic jets are so called because they synthesize a jet from a train of vortex rings or pairs, formed from the external fluid, without net mass addition. The device which produces such a jet consists of a cavity with rigid side walls, an oscillating diaphragm and a rigid cap with an orifice. Figure 2 shows the basic synthetic jet concept. When the diaphragm is vibrated rapidly, air is repeatedly drawn into the cavity through the orifice and then ejected out of the cavity through the same orifice. As the outgoing flow passes the sharp edges of the orifice, the flow separates forming a vortex ring, which propagates normally away from the orifice plate. The vibration of the diaphragm results in a train of vortices, which are formed at the excitation frequency.

One vibration cycle can be divided into an impingement stroke and an intake stroke. On the impingement stroke, the diaphragm deflects upward to compress the fluid in the

cavity. The increase in pressure drives the fluid out through the orifice. On the intake stroke, the diaphragm deflects in the opposite direction, and the cavity acts as a sink to entrain the fluid back into it from all the directions.

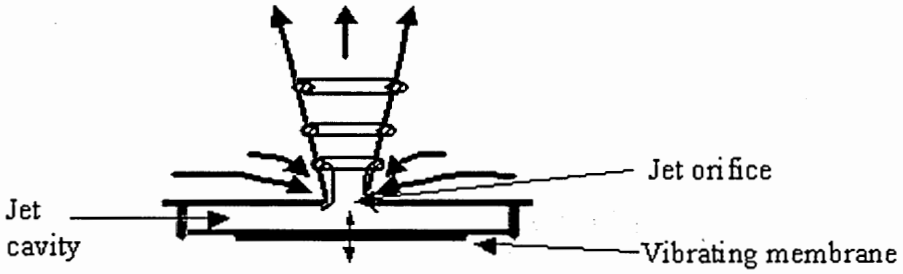

Figure 2. Schematic of a synthetic jet

In one vibration cycle, the cavity periodically works as a sink or a source which refills or discharges by the fluid. There is no net mass change within one cycle. The vibrating diaphragm produces momentum itself and adds the average 'effective' momentum to the downstream flow. If there is a control surface near the jet exit, the boundary layer of the control surface can be altered by the synthetic jet. During the intake stroke of the cycle, the jet draws the low momentum fluid in the boundary layer to the cavity. In the impingement stroke, the jet adds higher momentum to the flow boundary layer.

The concept of synthesizing a turbulent shear flow by controlled coalescence of its rudimentary coherent vortical structures (e.g. turbulent spots in a transitional boundary layer or vortex rings in a round jet) was proposed by Coles (1981) and was later tested in a flat plate boundary layer experiment (Savas et al., 1985). This turbulent flow forms because the shear flow is typically hydrodynamically unstable to these perturbations. Such instability leads to rapid amplification of the perturbations and a resultant large effect on the flow. Flow excitation can be effected using a variety of techniques including both external and internal acoustic excitation, vibrating flaps, unsteady bleeding or blowing, vibrating surfaces, and more recently zero mass flux synthetic jets. A number of investigations (Westerveldt, 1950 and Stuart, 1966) had been carried out into acoustic streaming using oscillating plates in resonance cavities and oscillating cylinders/plates in water and air, with jet velocities of up to 20 m/s in air and 3 m/s in water, reported. More recently, Jacobs et al. (1993) and Smith et al. (1998) had conducted more detailed studies on synthetic jets formed from an oscillating surface membrane.

A synthetic jet can be utilized in microelectronic thermal packaging because its two unique natures-vortex rings and zero-net-mass-flux. The train of the vortex rings has the ability to entrain more surrounding low momentum fluid into the jet core. More jet flow can carry away more heat. In addition, vortex rings induce more disturbances into the jet flow which facilitates the breakup of the boundary layer. Laminar flow exists in the boundary layer and heat conduction is the dominant heat transfer mode. With a thinner boundary layer, heat convection is enhanced with respect to heat conduction. Zero-net-mass-flux jets require no mass addition to the system, and thus provide means of

efficiently directing airflow across a heated surface. Because these jets are zero net mass flux in nature and are comprised entirely of the ambient fluid, they can be conveniently integrated with the surfaces that require cooling without the need for complex plumbing. This simple structure eases the integration of synthetic jet with current packaging components. Compared with other cooling techniques introduced previously, synthetic jets can provide efficient, on-the-spot, and on-demand cooling both at chip and package levels.

1.4 Research Objectives

Synthetic jets have seen widespread laboratory use in flow control (Rathnasingham et al., 1997 and Rediniotis et al., 1999). The jets actively modify the pressure distribution over an aerodynamic surface which leads to "dynamic virtual shaping". Flow separation manipulation could open new horizons in vehicle control and presents an exciting alterative over conventional control surfaces. The second widely used application is the mixing of combustion gases (Chen et al., 2000 and Wang et al., 2001). Fuel and oxidizer mixed with synthetic jets will alternately generate fuel-rich and fuel-lean combustion zones in the furnace. This is a promising low NOx combustion technology. Utility of synthetic jets in microsystem packaging to enhance thermal management is a newly emerging application.

In this research, the synthetic jet structure is proposed to be embedded into printed wiring board (PWB). The micromachined fluidic structure adds heat convection functionality to the PWB and forms an active cooling substrate (ACS). The fabrication of the ACS device is investigated. Instead of using the traditional piezoelectric materials,

a corrugated polymeric diaphragm is designed and optimized. Based on this polymeric diaphragm, an electromagnetic actuator is designed and optimized for high efficiency, low noise and low power consumption.

The fluid mechanics of a synthetic jet is well understood. However, the impact of a synthetic jet on heat transfer is still a challenging and unresolved problem. In this research, the fluid mechanics and cooling performance of the synthetic jet are characterized. The optimal jet operating conditions and the optimal cooling locations are determined. Dimensionless group analysis is applied to ascertain empirical correlations between fluid mechanics and heat transfer. To achieve a better understanding of the transport phenomena, computational fluid dynamics (CFD) software is used to simulate the synthetic jet behavior. In terms of this numerical investigation approach, some CFD fluid mechanics modeling of synthetic jets has been conducted previously (Rizzetta et al., 1999, Moran et al., 2000). This research is focused on coupling heat transfer with fluid mechanics and simulating this more complicated case.

The final goal of this research project is to develop a sophisticated methodology which facilitates the thermal management design through the synthetic jets cooling approach. Empirical correlations and CFD simulations are verified using experimental results. Both types of modeling can be applied in the future design as predictive tools. Under a particular cooling budget, a suitable synthetic jet structure will be designed and fabricated to meet the packaging requirements.

1.5 Outline

Chapter 2 of this thesis briefly reviews instrumentation used to characterize synthetic jet behavior. Two simulation tools are used to optimize some design work in this project. They are also introduced in this chapter. Chapter 3 discusses the ACS design concept and fabrication in great detail. Fluid and thermal analyses are performed, and the optimal operation conditions for the ACS are determined. Chapter 4 focuses on CFD simulations which provide a numerical approach to explore the complicated synthetic jet thermal management problem. Finally, Chapter 5 summarizes the conclusions drawn from the research.

Chapter 2

INSTRUMENTATION AND SIMULATION TOOLS

Laser Doppler vibrometry, particle image velocimetry, hot wire anemometer and infrared thermography have been used to characterize the diaphragm vibration, the microjets fluid behavior and cooling performance. Two simulation tools, ANSYS and Fluent, have been employed to model mechanical structure properties and transport phenomena. A brief introduction to the analysis instrumentations and simulation tools is provided in this chapter.

2.1 Analysis Instrumentations

The actuator is a critical component in generating the microjet. The vibration of the actuator diaphragm is evaluated by laser Doppler vibrometry. The synthetic jets generated at the downstream is investigated by a particle image velocimetry (PIV) which visualizes the entire flow pattern and a hot wire anemometer which pinpoint measures the velocity magnitude at particular positions. Cooling performance is explored by an infrared (IR) camera scanning technique.

2.1.1 Laser Doppler Vibrometry

Laser Doppler vibrometer is capable of measuring the magnitude of displacement for a moving object from a remote position using interferometer techniques. A Polytec Co. OFV-303 laser doppler vibrometer, a standard single point head interferometer, is used in

this study. The interferometer is built around a Helium Neon (HeNe) laser source and is almost completely self-contained.

By allowing the motion of the surface of interest to modulate the path lengths traveled by the laser beams, an interferometer can be used to detect vibrational signals of sub-nanometer amplitude. Interference is a phenomenon observed when two beams of light (from a common origin) are made to coincide. The resultant intensity after re-combination is seen to vary sinusoidally with the relative phase difference between the beams. In an interferometer, light from a laser source is divided at a beam splitter into two beams of approximately equal intensity. One beam exits from the "inner" interferometer cell, strikes the target, is coupled back into the interferometer and mixed with the reference beam. Each light beam, when impinging on photodetector, undergoes a phase shift determined by the distance that it has traversed (as shown in Figure 3). The phase shift can be related to the geometrical paths traveled by the beams. In this way, the displacement of vibrating surface is converted into a measurable phase difference and is accurately measured.

In the OFV-303 single point interferometer system shown in Figure 4, a linearly polarized HeNe laser is used as a light source, with its polarization oriented at 45 degrees to the horizontal plane of the source. A polarizing beamsplitter 1 splits the input beam into orthogonally polarized signal and reference beams. The signal beam, having passed through beamsplitter 1 and 2 and the focusing lens system, hits the measurement object. The special nature of beamsplitter 2 ensures that the returning beam is directed downward to beamsplitter 3. It combines here with the reference beam to generate the radio frequency (RF) modulated interference signals. Both output signals from

beamsplitter 3 are converted to electrical signals by photodiodes 1 and 2. The resulting output voltage constitutes the output signal of the interferometer and is transmitted to the processor controller where the RF signal processing is used to extract the velocity and displacement information. The resolution of the displacement in the most sensitive setting is ±8 nm.

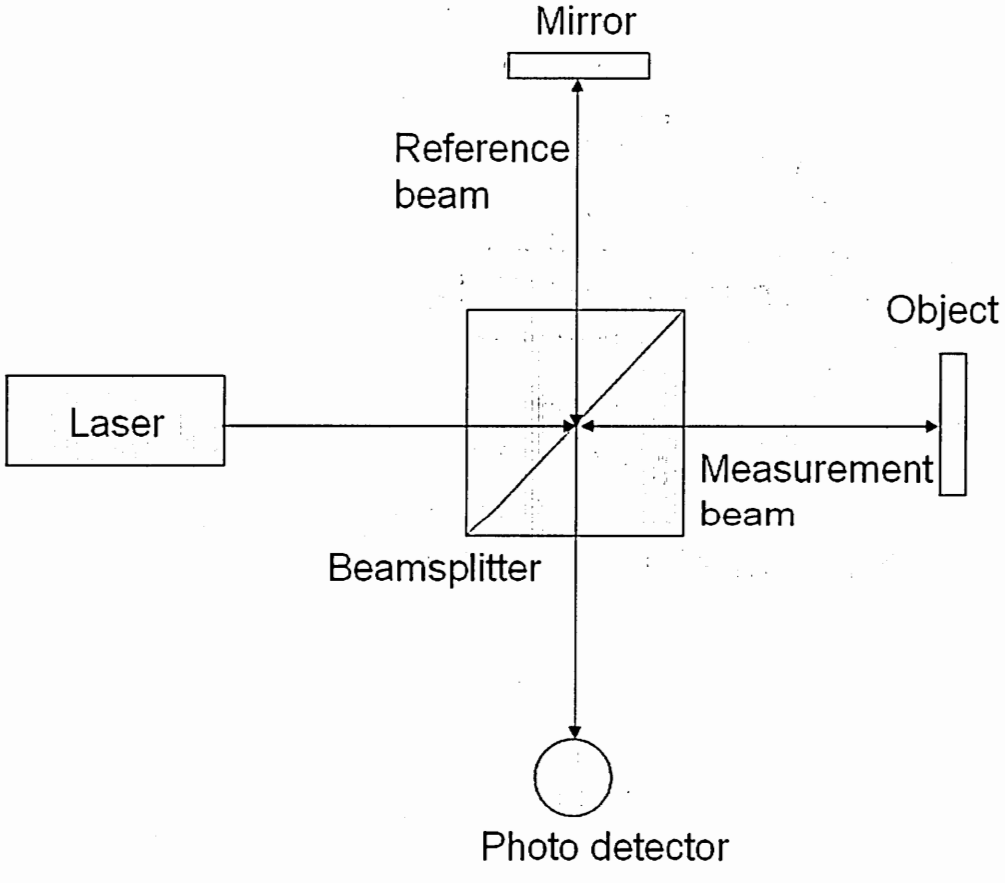

Figure 3. Schematic of an interferometer

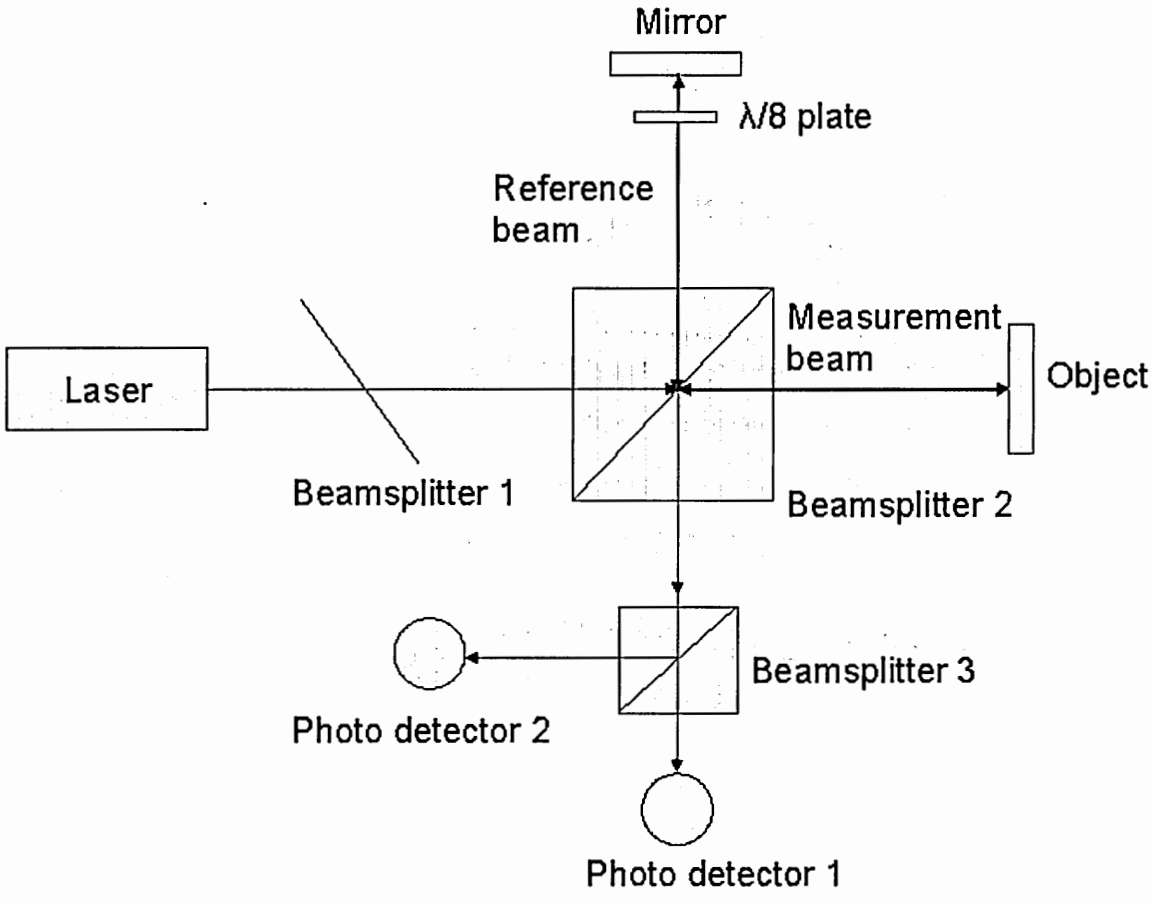

Figure 4. Layout of an OFV-303 laser Doppler vibrometer

2.1.2 Hot-wire Anemometer

A hot wire anemometer is basically a thermal transducer (Perry, 1982). An electric current is passed through a fine filament which is exposed to a cross flow. As the flow rate varies, the heat transfer from the filament varies. This in turn causes a variation in the heat balance of the filament. The filament is made from a material (e.g. tungsten) which possesses a temperature coefficient of resistance (i.e. if the temperature of the

filament varies, so does its resistance and hence the Joule heating). The variation of resistance is monitored and produces signals related to the variations in flow velocity or flow temperature. Therefore, the hot-wire method can be used for measuring the instantaneous velocities and temperatures at a point in a flow.

There are two modes of operation of a hot-wire system. The first is the constant current mode, in which case the current in the wire is kept constant and variations in wire resistance caused by the flow are measured by monitoring the voltage drop variations across the filament. The second is the constant temperature mode. Here the filament is placed in a feedback circuit which tends to maintain the wire at constant resistance and hence constant temperature. Fluctuations in the cooling of the filament are seen as variations in the wire current.

In this study, the constant temperature mode is used. The anemometer measures the fluid speed using a delicate probe (Dantec Co.) which consists of a 1 mm long, and 5 μm in diameter tungsten wire. This probe is heated to a temperature higher than the average temperature of the fluid. Using sophisticated circuitry, the anemometer stabilizes and maintains the probe temperature at a constant level throughout the measurement. Since the fluid flowing past the probe has a lower temperature than the probe, the wire is constantly being cooled by the fluid flow. The higher the velocity, the faster the rate of cooling. Since the anemometer must maintain the probe temperature at a constant level, it is therefore sensitive to the rate at which it is being cooled, i.e., the fluid velocity. This velocity is translated to a continuously changing voltage which has a nonlinear relationship with the flowing fluid. This voltage then undergoes signal conditioning, to filter out noise and improve the signal/noise ratio. After proper calibration of the probe

channels, it is possible to measure fluid velocities with an accuracy of 0.05% or greater, depending upon the measurement range and the quality of the calibration. In practice, the hot wire is calibrated by exposing to a series of flows with known characteristics. The resulting sensor readings are then recorded in a lookup table. Interpolation is used to evaluate intermediate readings during actual testing. The response time between the measurement and the instrument output is very short in comparison with other methods of fluid flow measurement and can reach a minimum of 1/2 microsecond. The major advantage of this mode is that the compensation for the thermal inertia of the filament is continuously adjusted automatically as its operating point varies. Thus, if one is taking a traverse of a wake, jet or boundary layer, there is no need for a special square wave calibration and compensator setting for each velocity. In reality, the constant temperature anemometer does not hold the wire exactly at constant temperature. The wire resistance has to vary by a small amount so as to give the amplifier a 'feedback' signal.

2.1.3 Particle Image Velocimetry

Particle image velocimetry determines the distance that particles have moved in the time between laser pulses. This enables the complete mapping of the velocity flow field external to the jet outlet. The system (TSI Inc.) consists of a pair of 50 mJ NdYag lasers, a system of lenses designed to create a sheet of arbitrary thickness and width, and a 1000×1000 pixel charge-coupled device (CCD) camera as shown in Figure 5. The measurement area within the flow field is defined by the position and physical dimension of a fan of laser light. With the illumination of two short duration laser flashes in the measurement area, a double-exposure of the flow field is captured (through the CCD camera to the frame grabber card) on the computer. Once the spatially displaced images

are stored in two separate frames, each velocity vector is extracted by performing mathematical correlation analysis on a cluster of particles within each interrogation region between the two frames (eliminating the problem of directional ambiguity). The seeding particles generated from the burnt incense in a closed chamber act as a tracking particle source. INSIGHT software (TSI Inc.) uses 2-frame cross-correlation to measure the distance which particles have moved between exposures on two image frames and then calculates the flow velocity. A square interrogation spot measuring 32 pixels on the side on a 64×64 grid is a tracking unit for distance measurement. The delay time between the two laser shots is chosen such that the maximum velocity of interest would result in motion across 25% of the interrogation area. In the system, lasers and camera can be locked to the driving signal of the actuator, and all data are averaged over at least 50 realizations (100 images).

2.1.4 Infrared Thermography

Infrared thermography has been used extensively in sensing thermal patterns on the heating surface of interest. Typically the analysis uses an infrared thermal scanning camera to record television-like thermal images on film or videotape. The information is then analyzed.

IR energy is emitted by all materials above 0 °K. Infrared radiation is part of the electromagnetic spectrum and occupies frequencies between visible light and radio waves. The IR part of the spectrum spans wavelengths from 0.7 micrometers to 1000 micrometers (microns). Within this wave band, only frequencies of 0.7 microns to 20 microns are used for practical, everyday temperature measurement. The property of a

body to emit radiation is called its emissivity. Different kinds of materials and gases have different emissivities, and will therefore emit IR at different intensities for a given temperature.

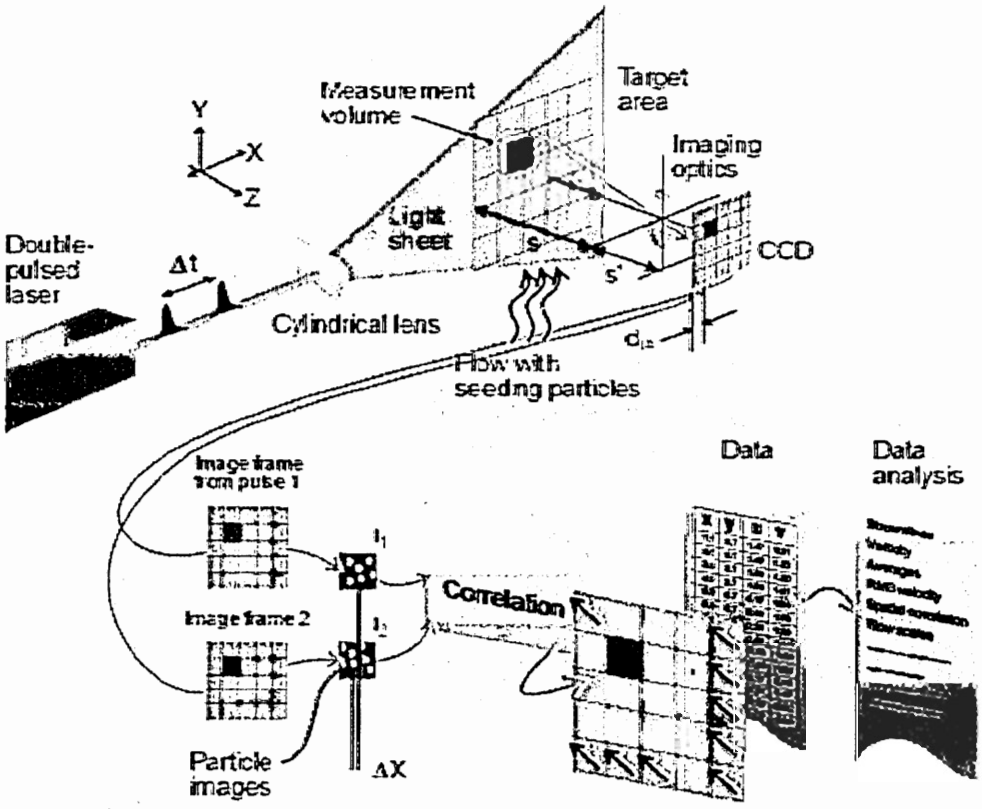

Figure 5. PIV flow diagram

Using specially designed sensors, IR imaging systems detect heat energy invisible to human eyes and convert this into a visible picture. The newly developed focal plane array (FPA) technology incorporates rows and columns of individual IR sensors which eliminates the requirement for scanners. Each IR sensor scans at the target and creates its own pixel of temperature image. In this research, ThermaCAM PM180 (Inframetrics Inc.) is used. The systems cooled PtSi detector delivers shortwave (3.4 μm to 5.0 μm) response required for wide range of basic and high temperature industrial applications. Its spatial resolution is 1.2 mrad (instantaneous field of view), and the thermal sensitivity can reach ±0.07 °C.

The advantage of the IR thermography technique is that an infrared camera is a non-contact device that detects infrared energy (heat) and converts it into an electronic signal, which is then processed to produce a thermal image on a video monitor and perform temperature calculations. Heat sensed by an infrared camera can be very precisely quantified, or measured, allowing to not only monitor thermal performance, but also to identify and evaluate the relative severity of heat-related problems. Here the IR camera is used to map the temperature contour on a heated surface.

2.2 Simulation Tools

Simulation tools are used in this study to model diaphragm motion and the resulting microjet flow. Finite element method (FEM) software, ANSYS, is used in diaphragm design to optimize its vibration behavior; finite volume method (FVM) software, Fluent, is used in microjet and fluidic structure design to maximize jet flow and enhance heat transfer.

2.2.1 ANSYS

ANSYS is a general-purpose finite element modeling package offered by ANSYS Inc. for numerically solving a wide variety of mechanical problems. These problems include: static/dynamic structural analysis (both linear and non-linear), heat transfer and fluid problems, as well as acoustic and electromagnetic problems.

In this study, ANSYS is used to simulate the mechanical behavior of diaphragm i.e. the displacement of diaphragm under certain force. Thus, it is possible to optimize the diaphragm structure design by maximizing the displacement and minimizing the applied force, which will help to reduce the input energy to the system.

2.2.2 FLUENT

Fluent is a computational fluid dynamics (CFD) simulation package produced by Fluent Inc. It is suited to perform flow and heat transfer modeling. This study uses Fluent to simulate the fluid mechanics and heat transfer of synthetic jets. GAMBIT is the preprocessor of Fluent which is also the product of Fluent Inc. By using GAMBIT, geometry of a physical model is drawn, meshing points are applied, and boundary surfaces are defined. The Fluent solver then is used to solve the problem with suitable fluid model. This software enables numerical results to be postprocessed into visual graphs. Once a simulation model is sufficiently robust to match experimental results, it can be used to predict the synthetic jet behavior and optimize the active cooling substrates design.

Chapter 3

Active Cooling Substrates

As a micro-electro-mechanical system, the active cooling substrate is the implementation of synthetic jets in the printed wiring board packaging component. This chapter describes the ACS design, fabrication and characterization.

3.1 Design Concept

Printed wiring boards (PWBs) are a composite of an organic (i.e. epoxy) and an inorganic (i.e. glass ceramic) material with external and internal wiring, allowing the electronic components to be mechanically supported and electrically connected. One of the goals of this study is to also incorporate fluidic channels into the PWB. This would result in an increase in the functionality of the PWB to include thermal management as well as electrical interconnection and mechanical support. Figure 6 shows the concept of an active cooling substrate (ACS) with fluidic functionality built in the PWB substrate. A heat carrier fluid, either in liquid state or in gas state, is driven through the fluidic passages and removes the heat generated by the thermally-active electronic devices.

To achieve this goal, two requirements must be met. The first requirement is that the fabrication technology to build the fluidic structures must be compatible with PWB manufacture. Figure 7 shows the basic steps of the lamination process for the formation of integrated fluidic channels in a PWB-compatible process. Multiple layers of printed wiring board are patterned either by mechanical drilling or laser cutting to form the

fluidic channels. These layers are then stacked, aligned, and laminated to form the final PWB structure with embedded fluidic functionality.

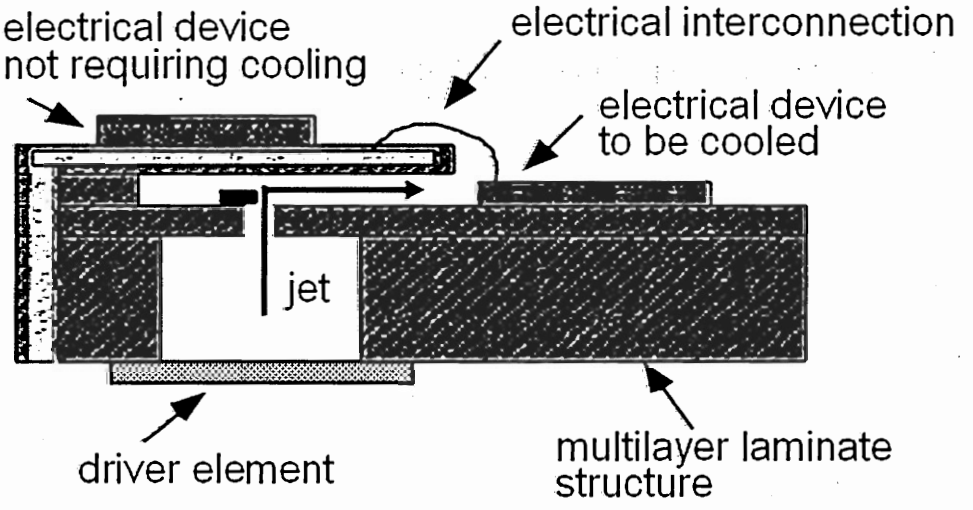

Figure 6. Schematic of the active cooling substrate

The second requirement is that the driver that creates the heat carrier fluid flow must have a low profile in order to fit within the thickness of the PWB. Typical PWB thicknesses are approximately 2 mm. Synthetic jets are an attractive approach to this problem since they can be fabricated within the thickness of a PWB. Figure 6 shows a schematic of the synthetic jet driver. A jet cavity is bounded on one side by a rigid plate bearing an orifice hole and on the other side by a flexible diaphragm. The vibration of the membrane results in the alternating entrainment and expulsion of air into and out of the cavity through the orifice hole as shown in Figure 6.

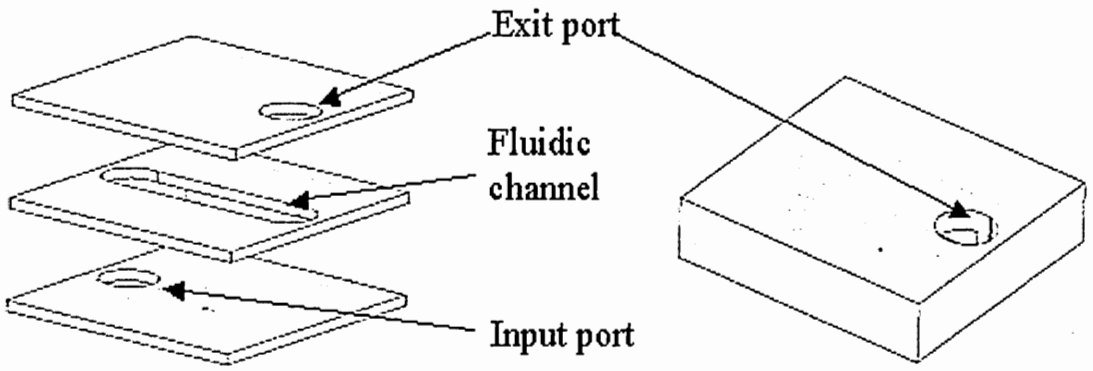

(a) (b)

Figure 7. Lamination process (a) patterned multilayers; (b) laminated PWB

Zero net mass flux is a main feature of synthetic jets, which means that no externally-supplied flow is needed to synthesize the jets. In addition, due to the small-scale vortical structures inherent in the synthetic jet, enhanced heat transfer is possible. The simple structure of the jet driver also lends itself to the design of low profile drivers.

The ACS can be fabricated by integrating synthetic jet technology into the PWB process as shown in Figure 7. Fluidic passages built into the ACS can vector the jet to the desired point on the PWB. The ACS can provide on-demand, pinpoint cooling of individual elements, multi-element cooling by jet positioning and vectoring, and cooperative, peristaltic-like pumping of ambient air over the die surface for efficient coupling to the global heat transfer. This methodology could prove advantageous over other thermal management technologies due to its simple structure without external plumbing, easy integration with circuitry, and high efficiency.

3.2 Diaphragm Material Selection

The integrated active cooling substrate is composed of two important components: (1) the actuator to generate the microjet; (2) the printed wiring board substrate with the fluidic passages which define the jet cavity and vector the microjet toward the hot electronics on board. In this study, two types of actuators are evaluated (i.e. piezoelectric actuators and electromagnetic actuators) which are distinguished by different diaphragm materials and excitation methods.

In the piezoelectric actuator, the vibrating diaphragm is either a piezo ceramic (e.g. Lead Zirconium Titinate-PZT) or a piezo polymer (e.g. polyvinylidene fluoride-PVDF). Piezoelectric materials can be used to convert electrical energy into mechanical energy. When a voltage is applied to a sheet of piezo film, it causes the film to change dimensions due to the attraction or repulsion of internal dipoles to the applied field. When one voltage polarity is applied, the piezo film becomes thinner, longer and wider. The opposite polarity causes the film to contract in length and width and becomes thicker. An alternating current (AC) voltage thus causes the film to vibrate. To obtain a sufficient air velocity, it is required to operate piezo ceramic disks under high frequencies (above 300 Hz) and large voltages (larger than 40 V_{rms}). At higher frequencies, the small-scale turbulent eddies present at the fluidic channel exit. The scale of the turbulent eddies is small and predominantly results in the high-frequency gas jet noise. At lower operation frequencies, the acoustic noise can be dramatically abated. On the other hand, a large voltage requirement means higher power consumption. Under current low power supply designs, this high voltage requirement may not be practical on the PWB. As a

result, the use of piezo ceramic actuators for the generation of the microjet would be unacceptable for cooling in many electronics applications. Therefore a piezo polymer is considered in the study.

Polyvinylidene fluoride (PVDF) is a thermoplastic fluorocarbon. PVDF can be made into a piezoelectric material by polarizing it in a manner similar to that used to produce electrets (Gallantree et al., 1976). This is achieved by heating up the polymer to about 100 °C, applying a large electric field (in excess of 60 MV/m), and then cooling with the field applied. Under the influence of the electric field, the dipoles of the β phase (the intrinsically piezoelectric crystal phase in PVDF) are able to rotate to give a net macroscopic polarization. This orientation of the dipoles is then frozen in place upon cooling, thus achieving a permanently piezoelectric material.

PVDF film with silver ink coating (Measurement Specialties Inc.) is obtained for this study. As found in a bimetallic strip, two sheets of piezo film are adhered together to form a bending element, or "bimorph". An applied voltage causes one film to lengthen, while the other contracts, causing the unit to bend. An applied voltage of opposite polarity bends the bimorph in the opposite direction. Under 150 V, the deflection is only about 0.5 mm in amplitude when one end of the strip is clamped and the other is free. Once the entire diaphragm is clamped on board with all the edge fixed, the displacement of the diaphragm center is indiscernible. Thus, the piezoelectric polymer film is not suitable to generate strong airflow.

The use of an electromagnetic actuator to generate airflow is also considered (Figure 8). There are three important parts in this kind of device: a flexible, elastic diaphragm; a

magnetic coil which can generate alternative magnetic field; a permanent magnet which offers a constant magnetic field. The latter two parts form the driving circuit to vibrate the diaphragm.

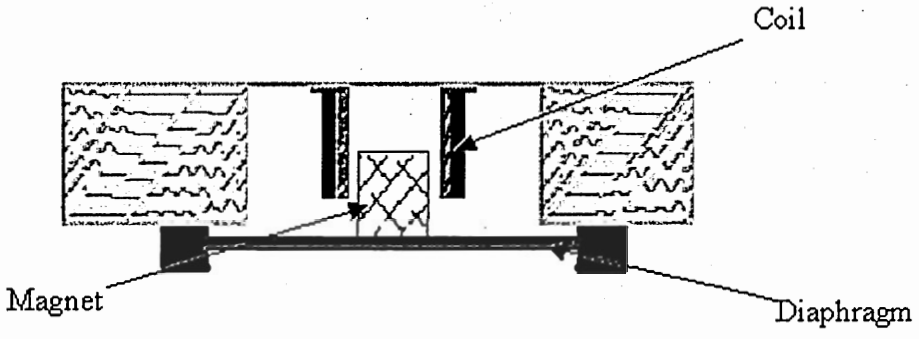

Figure 8. Electromagnetic actuator schematic

The diaphragm material must be flexible with a low Young's modulus, enabling a large displacement with a small applied force. In addition, to increase the efficiency of the device, air leakage must be prevented. Thus, the diaphragm is laminated on the printed wiring board (PWB) to insure tight contact. The polymer selected also must be able to survive a lamination process consisting of exposure to 4400 N force and 177 °C for 30 minutes.

The polymer materials used in the diaphragm fabrication are fluoroelastomers produced by Dyneon. Three formulations of this copolymer (shown in Table 1) are

specially formulated by Dyneon for this study and will be referred to as "A", "B", and "C". FE-5621Q (vinylidene fluoride hexafluoroproprylene polymer, 98% by weight and bisphenol AF, 2% by weight) and FC-2145 (1-propene, 1, 1, 2, 3, 3, 3-hexafluoro polymer with 1, 1, -difluoroethene) are the main compounds in the fluoroelastomers. The mechanical properties for each elastomer investigated are listed in Table 2. From the tensile modulus data, material B and C are stiffer than material A. This is achieved by increasing the total level of curing agent and by altering the filler composition.

This class of polymers has the advantage of both being able to survive the lamination process as well as being able to be molded into a variety of shapes. All the characteristics of the fluoroelastomers fit the electromagnetic actuator design requirements. Hence, this polymer is selected and used as the diaphragm material for the actuator.

Table 1. Formulations of Dyneon Fluoroelastomers

Formulation (parts by weight)	A	B	C
FE-5621Q	70	100	100
FC-2145	30		
N-990 Medium Thermal Carbon Black	10		
N-774 Semi-Reinforcing Furnace Black		8	8
Calcium Hydroxide	6	6	6
Elastomag^{TM} 170 Magnesium Oxide	3	3	3
50% Bisphenol AF MB Cure Agent			1.32
FX-5166 Cure Accelerator			0.375

Table 2. Material properties of Dyneon Fluoroelastomers

Fluoroelastemer		A	B	C
Press Cure at 350 °F	Tensile modulus, MPa	9.05	9.18	9.60
	Elongation to break, %	365	233	176
	Tensile modulus at 50% elongation, MPa	0.896	1.29	1.72
	Tensile modulus at 100% elongation, MPa	1.29	2.44	4.07
Post Cure 16 hours a t 450 °F	Tensile modulus, MPa	11.4	10.3	9.47
	Elongation to break, %	311	204	134
	Tensile modulus at 50% elongation, MPa	0.986	1.22	1.99
	Tensile modulus at 100% elongation, MPa	1.46	2.46	5.49

3.3 Polymeric Corrugated Diaphragm Structure Design

The Dyneon fluoroelastomer has a low Young's modulus of about 10 MPa. To obtain a larger displacement for a given force, it is proposed that concentric circular corrugations be molded into the polymeric diaphragm. A corrugated structure can increase the linear deflection range of the diaphragm and reduce the residual stress left during the diaphragm fabrication. Hence, diaphragms with mechanical sensitivities of approximately one order of magnitude higher deflections can be achieved compared with the corresponding flat diaphragm. The corrugated polymeric diaphragm consists of a rigid center, some circular corrugation structures and a circular mounting rim as shown in Figure 9. The rigid center where the electromagnetic force is applied on the diaphragm must not bend appreciably under load and be sufficiently large in diameter to prevent bulging of the unsupported area of the diaphragm. The mounting rim is designed to laminate the diaphragm onto the PWB substrate. To optimize the corrugation structure, an analytical characteristic equation and an FEM simulation tool, ANSYS, have been used to investigate the deflection of the diaphragm. Parameters related to the dimensions of the corrugated diaphragm (i.e. diaphragm diameter, corrugation thickness and corrugation depth) have been considered.

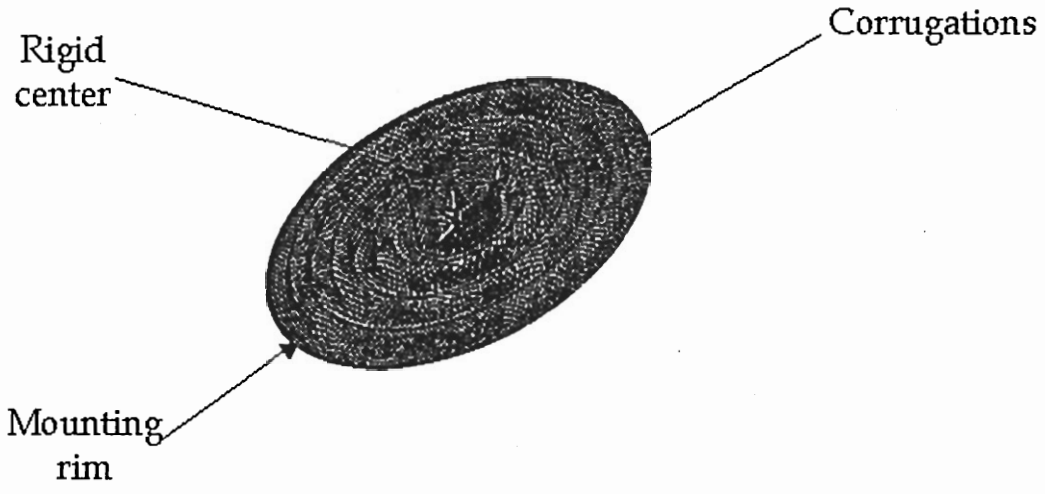

Figure 9. Schematic of a corrugated diaphragm

Heat carried away by the flow media can be determined by the following equation:

$$q = \dot{m} C_p \Delta T = \rho Q C_p \Delta T \tag{1}$$

where q is the heat flow rate, C_p is the specific heat of the flow media, ΔT is the temperature difference at the exit and entrance of the heating zone, $\dot{m}$ is the mass flow rate. If the flow density ρ is considered constant, the mass flow rate $\dot{m}$ can be calculated as the product of density ρ and volumetric flow rate Q. Based on Equation (1), to enhance heat convection over a hot electronic component, the volumetric jet flow rate must be maximized. An increase in the volumetric flow rate has two effects: first, a greater jet flow will carry away more heat; second, a more powerful jet flow will entrain

more induced airflow which also removes more heat. Equation (2) presents the volumetric flow rate (Q) during impingement strokes for synthetic jets under the assumption that air compressibility is ignored (an assumption that is valid when the velocity is significantly less than the velocity of sound):

$$Q = \Delta V \cdot (2f) = \frac{\pi}{3} \cdot (b^2 + ab + a^2) \cdot (\frac{D}{2}) \cdot (2f) = \frac{\pi}{3} \cdot (b^2 + ab + a^2) \cdot D \cdot f \qquad (2)$$

ΔV is the volume change during diaphragm vibration from rest position to full impingement position which is approximated as a frustum of a cone; b is the rigid center radius; a is the diaphragm radius; D is the peak-to-peak deflection of the diaphragm; f is the operation frequency, which is normally selected to be the resonance frequency where the deflection is largest.

The geometry of a diaphragm plays an important role in modifying the volumetric flow rate. It will affect every variable in Equation (2). The diaphragm dimensional impact on vibration frequency will be discussed later in this section. Obviously, changes in the size of rigid center or diaphragm will dramatically change the volumetric flow rate. The size of the diaphragm is limited because of the device application that requires integration with small and compact electric components. Therefore, the diaphragm size is a set parameter defined by its application. In addition, by the limit of our laboratory's molding technology and material properties, the thickness of the corrugation structure (h) can not be less than 0.1 mm. The other important adjustable geometry parameters are the

radius of rigid center b and the depth of corrugation H which can affect deflection D in Equation (2).

From the energy cost perspective, it is advisable to obtain maximum diaphragm displacement with a smaller driving force, namely a smaller coil driving current. The resistance to a loading force is due to both bending and tensile forces. The bending effect is linearly proportional to the diaphragm displacement. The tensile forces are negligible at low displacement but become more significant at large displacement. The tensile effect is proportional to the third order of the diaphragm displacement. Based on the method of superposition, Giovanni (1982) related static force with corrugated diaphragm deflection by the following characteristic Equation (3):

$$F = \left(\frac{\pi Eh^3}{a^2} K_F A_F\right) \cdot \left(\frac{D}{2}\right) + \left(\frac{\pi Eh}{a^2} L_F B_F\right) \cdot \left(\frac{D}{2}\right)^3 \qquad (3)$$

where F is the static force applied on the diaphragm, E is the material elasticity modulus. A_F is the flexural force coefficient, and B_F is the tension force coefficient which are functions of the ratio h/H. A_F decreases as h/H increases, while B_F increases as h/H increases. K_F is the bending stiffness coefficient, and L_F is the tension stiffness coefficient which depends on the ratios of both b/a and h/H. K_F and L_F increase as b/a increases or h/H increases. The stiffness and linear range of the corrugated diaphragms may be increased by the depth of the corrugations. The shape and number of corrugations have a small effect on the stiffness of the diaphragm. ANSYS is also used

to model the deflection under an applied force to check the results from the characteristic Equation (3). An axisymmetric physical model of the diaphragm is drawn and meshed into triangular elements. The edge of the diaphragm is fixed, and a force is loaded at the diaphragm center. The deflection of the entire diaphragm can be simulated. In ANSYS, a nonlinear large deflection model is used to calculate the load-displacement relationship as shown in Equation (4):

$$\{q_{i+1}\} = [K]\{u_i\} \tag{4}$$

$$[K] = [K_0(u_{i+1})] + [K_G(u_{i+1})] \tag{5}$$

where $\{q_{i+1}\}$ is a vector of external nodal forces, and $\{u_i\}$ is a vector of nodal displacements of the structure. $[K]$ is a stiffness matrix which consists of two terms as shown in Equation (5). $[K_0\ (u_{i+1})]$ is the structure stiffness matrix, and $[K_G\ (u_{i+1})]$ is the structure geometrical stiffness matrix. In small displacement simulation, only $[K_0\ (u_{i+1})]$ is considered and maintained constant under different loads. In large displacement simulation, $[K_G\ (u_{i+1})]$ is taken into account as well which represents the geometry nonlinearity and varies with the compressive axial loads. The nonlinear nature of a large deflection analysis requires an iterative solution. For any given loading configuration and a load step, the program must iterate while updating the stiffness matrix, $[K]$ and the displacement vector, $\{u_i\}$ until the change in displacements is sufficiently small.

From Equation (3) and ANSYS, an optimized geometry can be obtained from the energy cost view (i.e. the optimal values for rigid center radius b, depth of corrugation H). However, since the final goal is to maximize volumetric flow rate, the effect of diaphragm geometry on resonance frequency has to be considered as well to maximize the product of D and f. Resonance frequency can be calculated by the following equation:

$$f = \frac{1}{2\pi}\sqrt{\frac{k_s}{m}} \tag{6}$$

where m is the mass of the diaphragm, and k_s is derived from Equation (7) as:

$$k_s = \frac{\pi E h^3}{a^2} K_F A_F \tag{7}$$

To increase the resonance frequency, b should be enlarged to achieve larger K_F, also it can enlarge the b^2 and ab terms in Equation (2). However, this will reduce deflection under a certain force. Considering both the energy view and the frequency view, once the frequency falls into some desired range (i.e. tens of Hz, or hundreds of Hz), the optimal rigid center radius (b) is obtained. Then the other optimal dimensions can be

determined as well. Based on the design principles discussed above, two diaphragm prototypes have been optimized and employed in different ACS microfluidic structures.

The first prototype, diaphragm I, is utilized in a *vertical* microjet device (shown in Figure 10(a)). The outer diameter (OD) of diaphragm I is set to be 16 mm, then the rigid center diameter is optimized to be 5 mm. There are three 90-degree triangular corrugation structures on the diaphragm with a corrugation depth of 2.0 mm and a diaphragm thickness 0.1 mm. This diaphragm has a resonance frequency of about 40 Hz. The entire diaphragm is made from fluoroelastomers.

The second prototype, diaphragm II, is a hybrid diaphragm which is made from two different materials (fluoroelastomer and epoxy prepreg) and is used in a *tangential* microjet device (shown in Figure 10(b)). Diaphragm II is a modification of diaphragm I. It has an OD of 33 mm, which is larger than diaphragm I, to obtain larger periodical volume change. A low-density material epoxy prepreg is selected to build a rigid center instead of the elastomer because it is much stiffer. As a result, less material is needed which will make a thinner rigid center, dramatically reduce the total mass of the diaphragm and as well the force to drive it. The epoxy prepreg is cut into circular sheet with 24 mm in diameter and glued at the opened center of the diaphragm surrounded by elastomer corrugation structures. Diaphragm II has one and a half 60-degree triangular corrugation structures with 2.2 mm in depth and 0.2 mm in thickness. This diaphragm has resonance frequency of about 100 Hz.

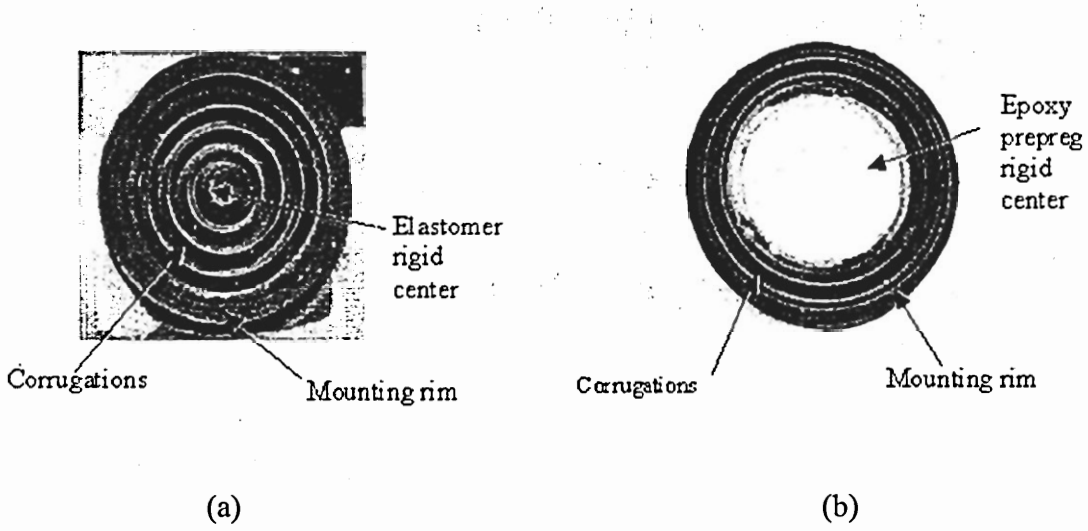

Figure 10. Structures of diaphragms (a) diaphragm I (b) diaphragm II

To fabricate the diaphragm, a molding technology is used. An aluminum mold is built into two parts. Dyneon fluoroelastomer pellets are fed into the gap between the two parts of the mold, and cured under 4448-N force and at 177 °C for 30 minutes. Then the mold is separated and diaphragm is removed. Diaphragm II involves the formation of a corrugated ring with an opened center. The rigid center disk for the diaphragm is cut from an epoxy prepreg sheet and glued to the corrugated ring using a cyanoacrylate glue.

After the diaphragms are fabricated, they are assembled with the coil and magnet into the PWB substrate. Then their mechanical properties can be tested. The results will be discussed in the following sections.

3.4 Vertical ACS Device

In the vertical ACS configuration, the synthetic jet is vertical to the outlet plane. A schematic of the device is shown in Figure 11. The magnet is mounted on the vibrating

diaphragm, and the coil is fixed on the substrate. During the course of the diaphragm molding process, a small flat magnet is buried in the rigid center of the diaphragm I. Another samarium-cobalt (Sm-Co) magnet is then placed on the diaphragm using the attractive force between those two magnets. This Sm-Co magnet has a cylinder shape with 3.2 mm in diameter and 3.2 mm in height. A coil with 4.2 mm in inner diameter and 4.1 mm in height is wound by using 0.125 mm diameter copper wire; the total resistance is approximately 8 ohms. The coil is glued in the substrate cavity. With an applied AC current to the coil, the magnetic force between coil and magnet drives the magnet through the stationary coil and vibrates the diaphragm. Figure 12 shows an assembled vertical ACS device. The actuator vibration, microjet fluid mechanics, and cooling performance are investigated.

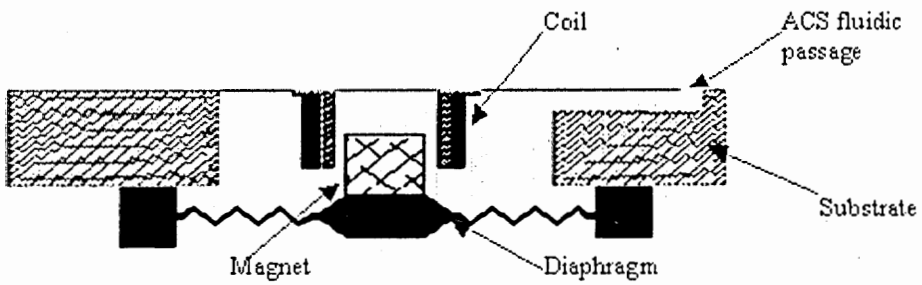

Figure 11. Schematic of a vertical ACS device

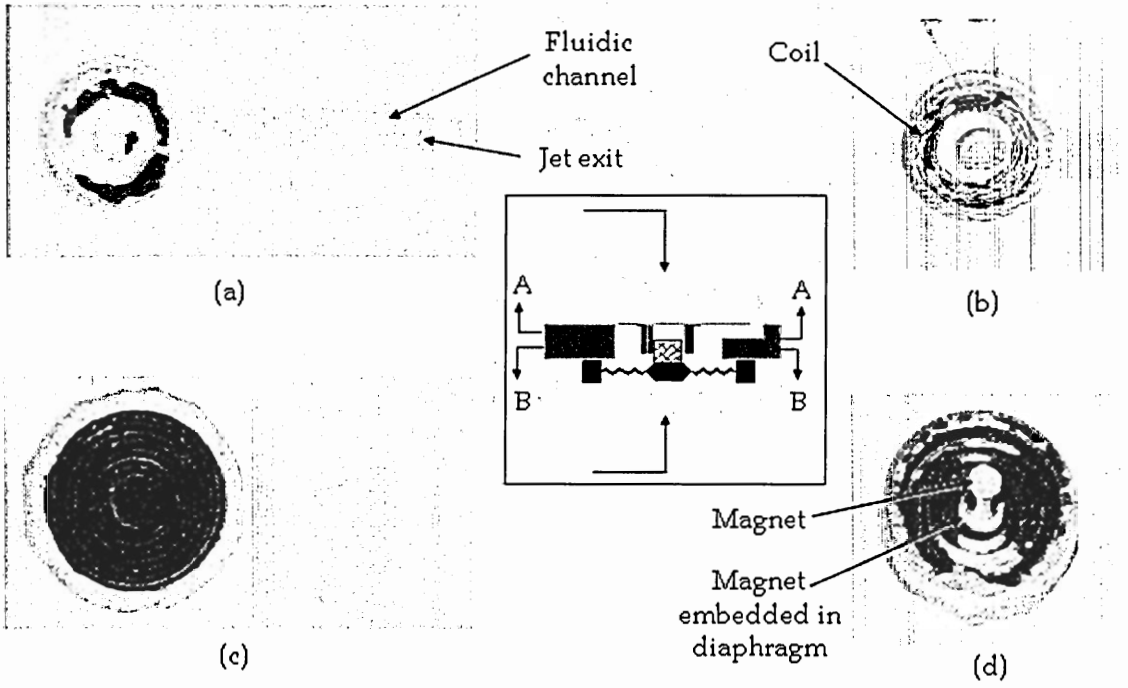

Figure 12. Assembly of a vertical ACS device (a) top view of vertical ACS (b) A-A cut view of vertical ACS (c) bottom view of vertical ACS (d) B-B cut view of vertical ACS

3.4.1 Diaphragm I Excitation

Displacements of the actuator diaphragms are studied under both static force and dynamic force. These results help to determine the optimal operation conditions and to verify the use of simulation tools (i.e. ANSYS or the theoretical characteristic equation) to optimize diaphragm design.

As mentioned in Section 3.2, there are three formulations of the Dyneon fluoroelastomers which have different tensile moduli. Using these elastomers and the same mold designed for diaphragm I, three different diaphragms are fabricated. Their

property comparisons will be discussed later. Diaphragm I-A refers to a diaphragm I made with copolymer A; diaphragm I-B refers to diaphragm I made with copolymer B; diaphragm I-C refers to diaphragm I made with copolymer C.

The deflection of diaphragm I-A is studied by first applying static force. The force is generated by loading a mass on the diaphragm. The deflection is measured using a microscope. The results are shown in Figure 13. ANSYS modeling (as explained in section 3.3) and the theoretical characteristic equation results are also compared with the experimental results. As the applied force increases, the deflection increases as well. Below 0.013 N, deflection is in a linear regime. It is observed that the experimental results are in good agreement with the predictions from ANSYS modeling and the characteristic equation up to 0.013 N. In actual use, the diaphragm is operated in this linear regime (i.e. $F<0.013$ N). Both tools are satisfactory for design and optimization of the diaphragm in the linear regime under static mode.

In the characteristic Equation (3), the first order term dominates in small deflection regime and the third order term dominates in large deflection regime. The ANSYS simulations more closely represent the data than the characteristic equation in large deflection regime because ANSYS offers a comprehensive set of nonlinear laws (i.e. large displacement models) to accurately simulate the nonlinear large deflections under external forces.

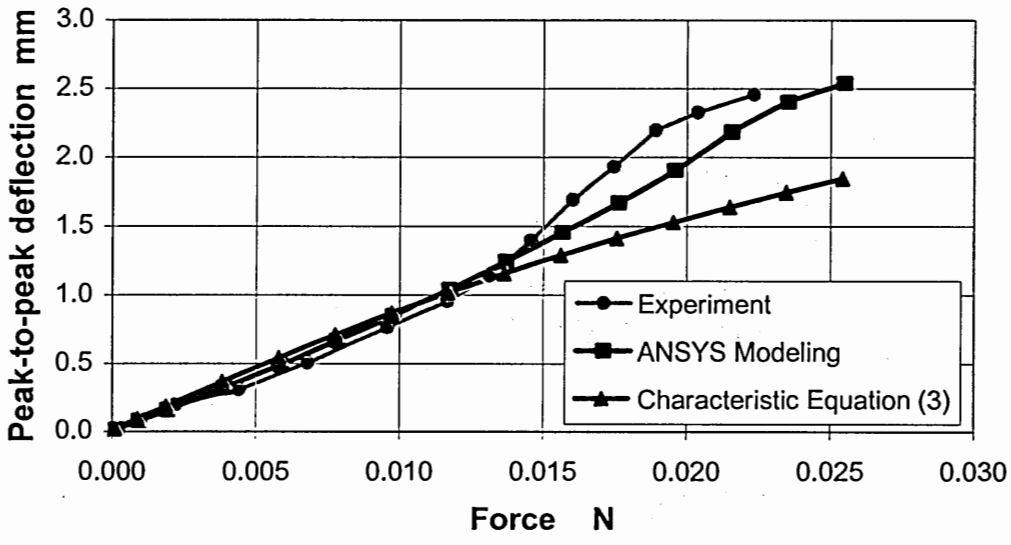

Figure 13. Deflection vs. static force of diaphragm I-A

When driven by an electromagnetic force, the diaphragm operates in a dynamic mode. In this case, the frequency response can be studied to find the optimal operation frequency. Figure 14 shows the experiment performed on diaphragm I-A with microjet outlet size of 4.09 mm in diameter, the coil driving current is 180 mA. The peak-to-peak deflection is measured by laser vibrometer. Experimental data are drawn in logarithm and decibel scales. For this diaphragm, the resonance frequency is 40 Hz. After the resonance frequency is exceeded, the deflection magnitudes decay with the slope of -40 dB/decade, indicating a second order harmonic system. Physically, the quality factor is the ratio of the stored energy and the dissipated energy in the system. From the data in Figure 14, the quality factor can be calculated by the ratio of resonance frequency and 3 dB-decay bandwidth. The quality factor is approximately 2 for this system. This low value indicates that significant energy is dissipated in the "spring" vibration system.

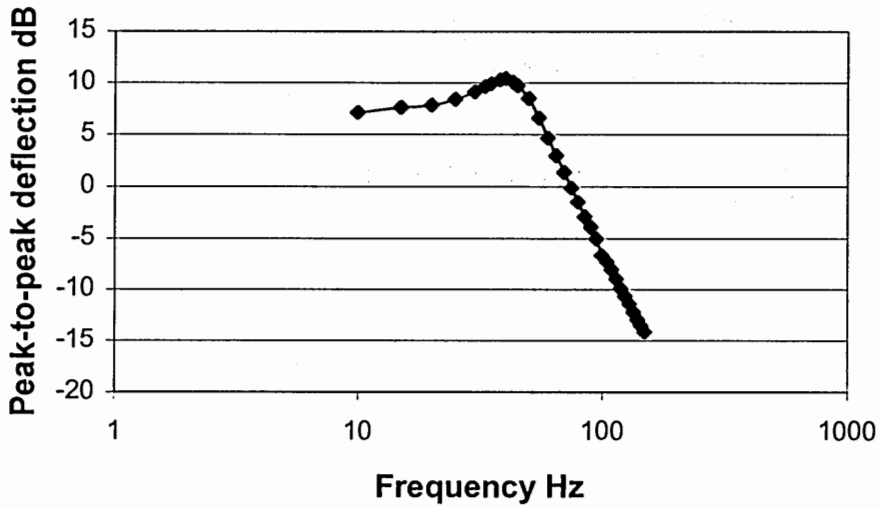

Figure 14. Frequency responses of diaphragm I-A in log-dB scale

The type of material used in the diaphragm will also affect the volumetric flow rate. The modulus of the material affects the deflection and frequency in Equation (2). If the material is stiffer, then a smaller deflection under a certain force and larger resonance frequency will occur. In this study, three different elastomer materials are made into diaphragm I-A, B, C respectively which have the same geometry and are operated at the same conditions. From Figure 15, the resonance frequency of the diaphragms increases as the modulus of the polymer increases. Diaphragm I-A has resonance about 40 Hz; I-B 50 Hz; I-C 90 Hz. At the same time, the maximum deflection also decreases with increasing modulus. Diaphragm I-A has maximum deflection about 3.3 mm; I-B 2.2 mm; I-C 0.7 mm. With the same device geometry and the same operation conditions, the outlet flow rate should be proportional to the product of frequency and deflection

(Equation (2)). To obtain the largest flow rate at the outlet, diaphragm I-A is the best choice.

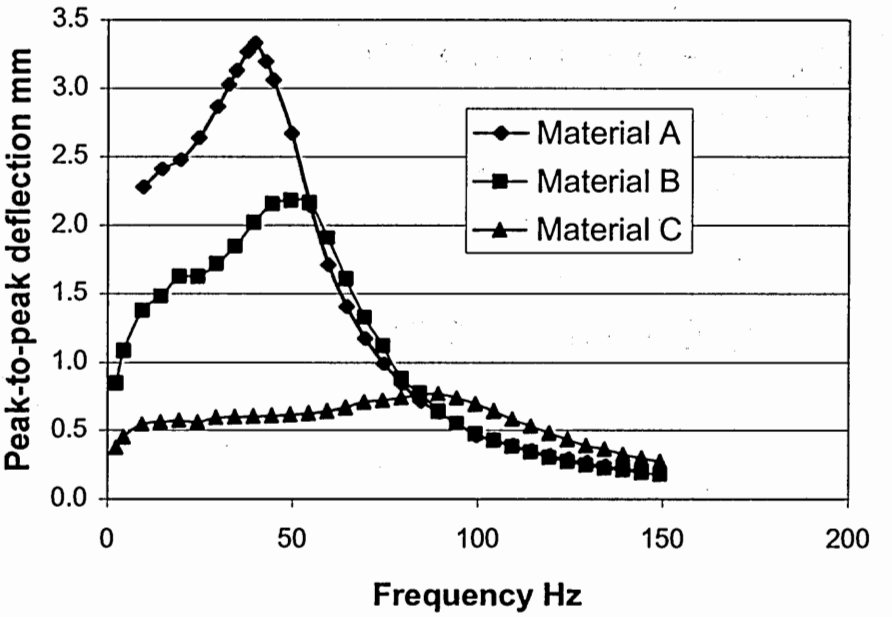

Figure 15. Frequency responses of diaphragms made from different materials

The pressure load can also affect deflection and resonance frequency. When the diaphragm vibrates, the air in the cavity is alternately pushed out and drawn in. Therefore, the pressure within the cavity varies during operation, resulting in a damping effect on the diaphragm. To observe the loading effects, the diaphragm I-A is placed in the cavity with different outlet orifice sizes. Table 3 shows this series of experiments

which are performed under the same electromagnetic force with the coil driving current 180 mA. From Table 3, the loading effect is observed when the outlet orifice size is smaller than 2.72 mm in diameter, for which the deflections begin to depend on the orifice diameter. For orifice sizes larger than 2.72 mm, diaphragm deflections are similar at the resonance frequency about 40 Hz; therefore, loading effects can be ignored.

Fatigue tests are also performed on diaphragm I-A. The integrated ACS is continuously vibrated at its resonance frequency for over two weeks. No obvious mechanical properties changes (i.e. yielding or breaking) occurred during this time period.

3.4.2 Vertical ACS Fluid Mechanics Characterization

The fluidic characterization is performed in the vertical ACS with a jet outlet diameter of 4.09 mm, operating at 50 Hz with a coil driving current of 180 mA. The diaphragm (with dimensions given in section 3.3) is made from elastomer material A. The fluid mechanics of the microjet is investigated by using PIV and hot-wire anemometry.

A sequence of PIV images of the velocity flow field at the jet outlet is taken phase-locked to the actuator driving signal at 18 equal time intervals. The measurement setup is shown in Figure 16. The images begin with the upward motion of the actuator diaphragm ($t/T=0$; t is operation time, T is period) which results in the ejection of fluid from the jet cavity (Figure 17(a)). The evolution of the synthetic jet can be divided into two distinct domains. Near the jet exit plane, the flow is dominated by the time-period formation and

advection of discrete vortex rings which ultimately undergo transition to turbulence, slow down and lose their coherence.

Table 3. Frequency responses of diaphragm I-A under different loading conditions

Outlet orifice diameter (mm)	Peak-to-peak deflection at resonance (mm)	Resonance frequency (Hz)
4.09	3.328	40
3.78	3.328	40
3.25	3.328	40
2.72	3.232	40
2.51	3.264	40
2.20	3.059	40
1.52	2.602	35

Each image shows the flow field captured by the camera on the 2-D symmetric plane of the device. X-axis is right above the outlet in horizontal direction. Y-axis is normal to the outlet. The physical size of each image is 17 mm wide and 17.2 mm high. The outlet orifice is located at position of (5 mm, 0 mm) point. The front end of the fluid slug that is ejected out of the orifice and leads to the formation of the vortex ring is apparent at time $t/T=0.055$. Some traces of the previous vortex ring are still discernible above $y=10$ mm. In subsequent images ($0.111<t/T<0.444$), the new vortex ring continues its rollup as it is advected downstream. This represents the impingement stroke.

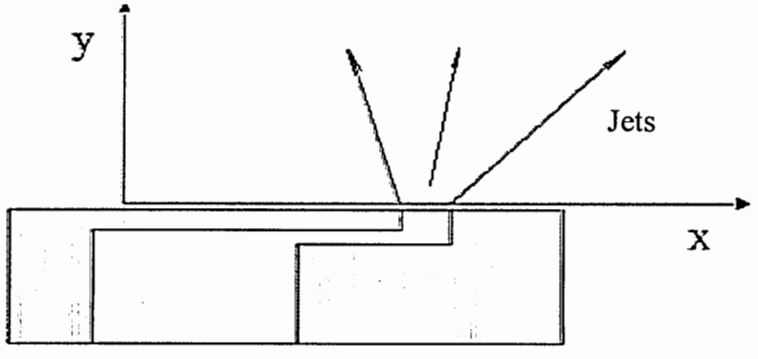

Figure 16. Schematic of vertical ACS PIV measurement setup

At $0.5<t/T<0.944$, the jet undergoes the intake stroke where air near the outlet is pulled into the cavity. At the same time, the cores of the vortex ring still have high axial momentum, continue the upward motion. In addition, the vortex ring begins to exhibit

small-scale motions and undergoes a transition to turbulence which is accompanied by a reduction in their advection velocity. The transition process begins with the onset and rapid amplification of a spanwise instability of the primary vortex that leads to the formation of normally spanwise-periodic, counter-rotating, streamwise vortex rings that are wrapped around the cores of the primary vortices and ultimately lead to a cellular breakup of their cores.

Due to the effect of the channel which vectors the jet into horizontal direction, the jet is not normal to the outlet surface; the flow is tilted at an angle to the jet outlet. This also causes the unsymmetrical vortex ring where the left-hand side of the vortex is much larger than the right-hand side.

A hot-wire anemometer is used to measure the velocity magnitude of the synthetic jet at some position above the outlet. The magnitude of the phase-averaged centerline velocity in one period at a position of 0.8 mm above the outlet is shown in Figure 18. Actually, the velocity magnitude right at the outlet is of great interest due to the zero-net - mass-flux feature of synthetic jets. However, the closest position of 0.8 mm above the outlet is selected as the measurement position because of the size of the orifice, which is not large enough to accommodate the hot-wire probe without outlet blockage. Another reason for keeping the wire out of the orifice is to prevent the hot-wire from heating up the air in the channel and greatly changing the flow field.

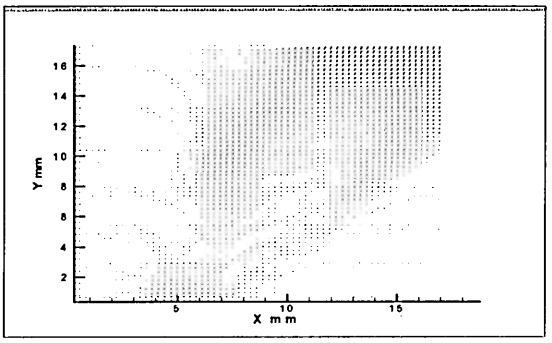

(a) *t/T=0*

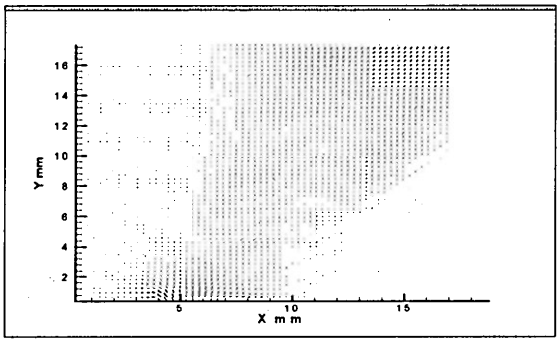

(b) *t/T=0.056*

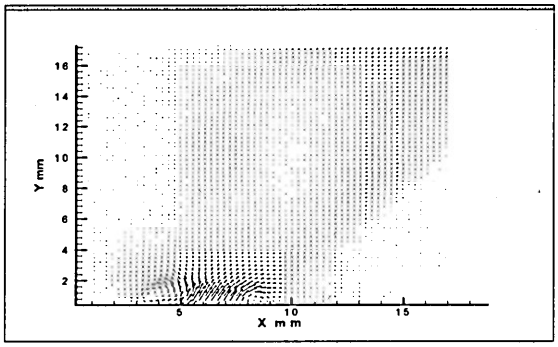

(c) *t/T=0.111*

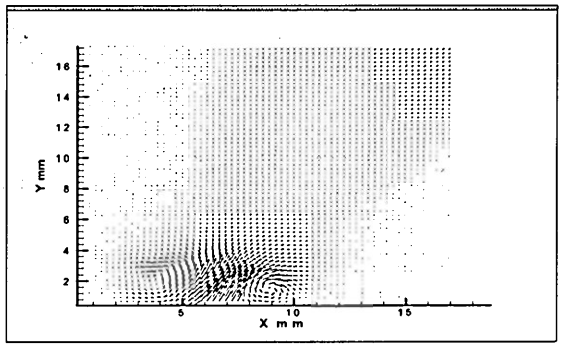

(d) *t/T=0.167*

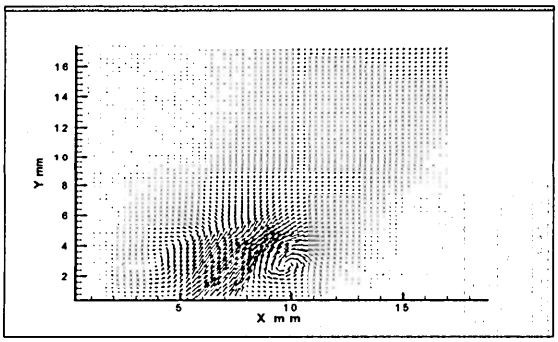

(e) *t/T=0.222*

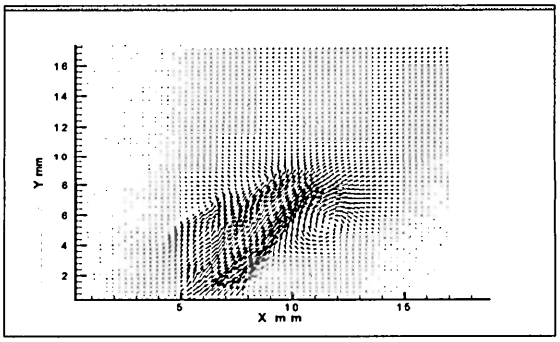

(f) *t/T=0.278*

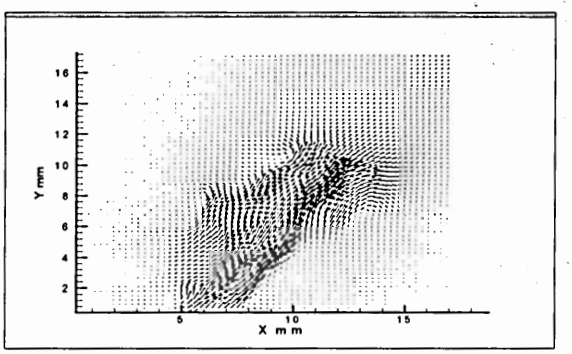

(g) *t/T=0.333*

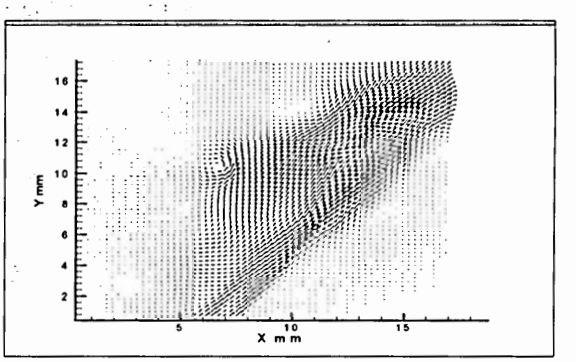

(h) *t/T=0.389*

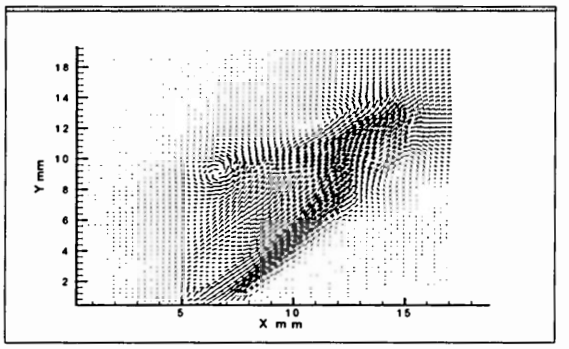

(i) *t/T=0.444*

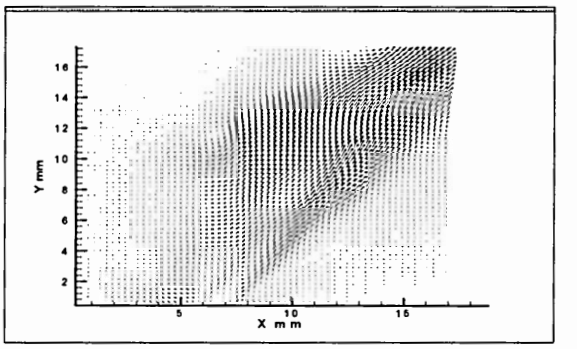

(j) *t/T=0.5*

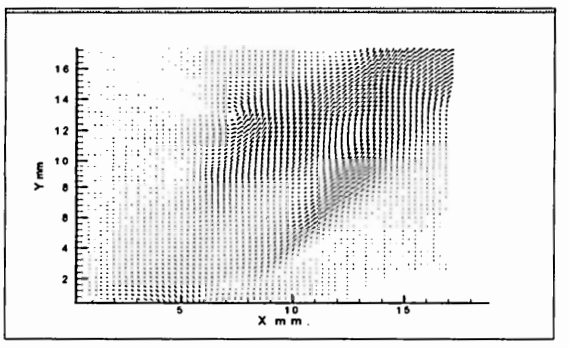

(k) *t/T=0.556*

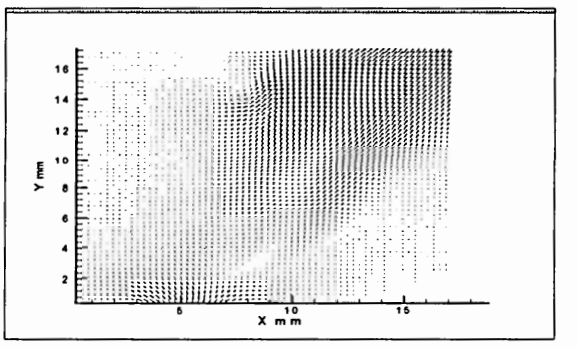

(l) *t/T=0.611*

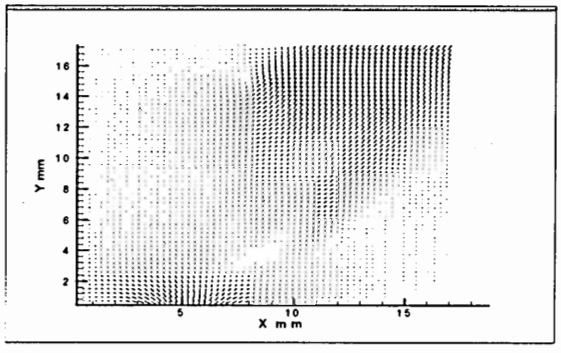

(m) *t/T=0.667*

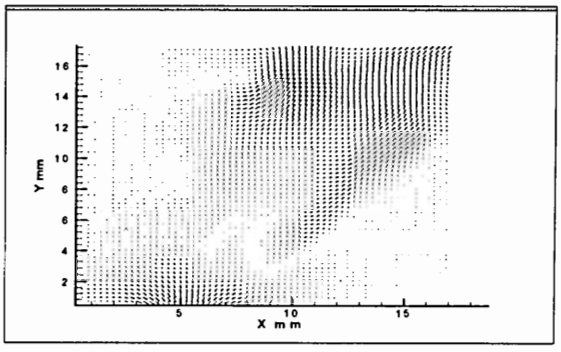

(n) *t/T=0.722*

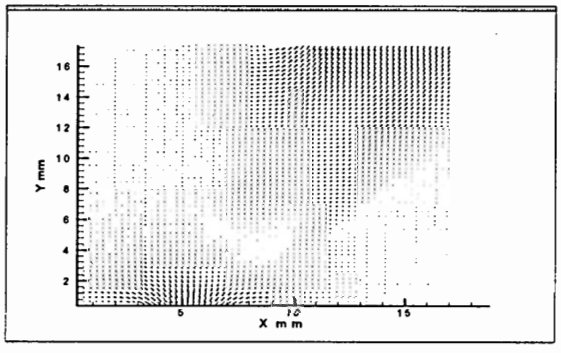

(o) *t/T=0.778*

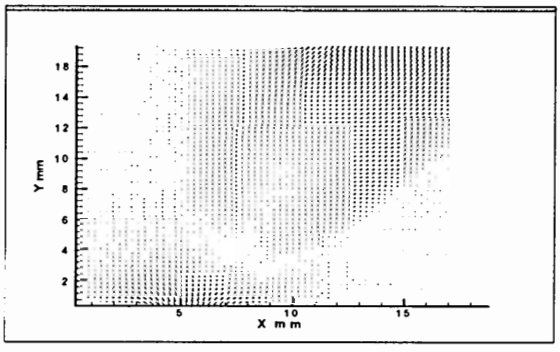

(p) *t/T=0.833*

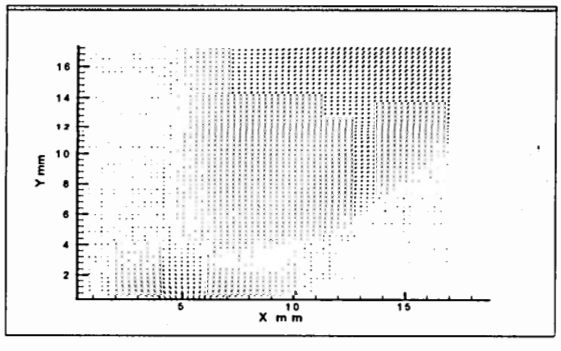

(q) *t/T=0.889*

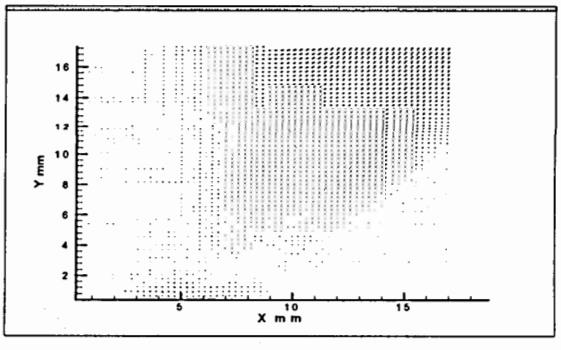

(r) *t/T=0.944*

Figure 17. Phase-locked PIV images of vertical ACS in X-Y plane taken at 18 equal intervals during the actuator cycle

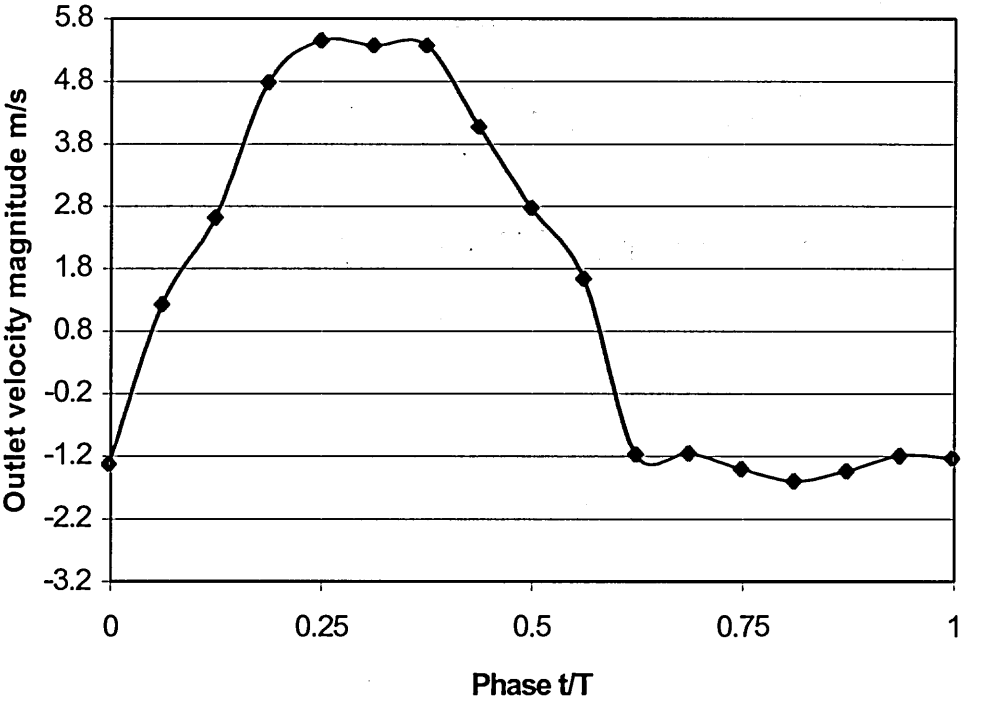

Figure 18. Phase-averaged centerline velocity magnitude in one cycle at the position of 0.8 mm above the outlet, orifice diameter=4.09 mm, frequency=50 Hz, and coil driving current 180 mA

Phase $t/T=0.25$ and $t/T=0.75$ are the full impingement and full intake points, respectively. The peak centerline velocity at the 0.8 mm away from the exit is about 5.5 m/s during the impingement stroke; the peak centerline velocity is about 1.6 m/s during the intake stroke. The time-averaged velocity is 1.46 m/s away from the outlet. For a synthetic jet, the outlet average velocity over time should be zero due to its zero-net-mass-flux nature. However, downstream of the exit, the average velocity may not be zero. At the impingement stroke, as the jet propagates streamwise, the centerline velocity decreases due to the entrainment of the low momentum air into the jet core (Figure 19). At the intake stroke, the centerline velocity magnitude also decreases as the hot-wire measurement point moves further away from the jet exit because the ACS only draws the air surrounding the exit back to the cavity which has less effect on the flow region farther away from the exit. Therefore, the time-averaged velocity varies with the distance to the jet outlet. The average velocity over time decays to zero due to the loss of the jet kinetic energy. The difference between impingement and intake peak velocity as shown in Figure 18 indicates that at some distances away from the exit, there exists a net jet flow to carry away the heat. The larger the effective net flow, the better the cooling performance.

The impingement peak velocity as a function of orifice diameter is measured at the position 0.8 mm above the outlet by a hot-wire anemometer. The results are shown in Figure 20. At the smallest orifice diameter of 1 mm, the phase-averaged impingement peak velocity is 16 m/s. As the orifice diameter increases, the sensitivity of peak velocity to outlet size decreases. From the above pressure load study (Table 3), at large diameters, the deflection is relatively independent of orifice size. Utilizing this feature, one large orifice can be divided into several smaller ones, each is connected to the cavity with a

separated channel and an individual hot component. Therefore, one multi-port active cooling substrate can fulfill multiple-point-cooling tasks.

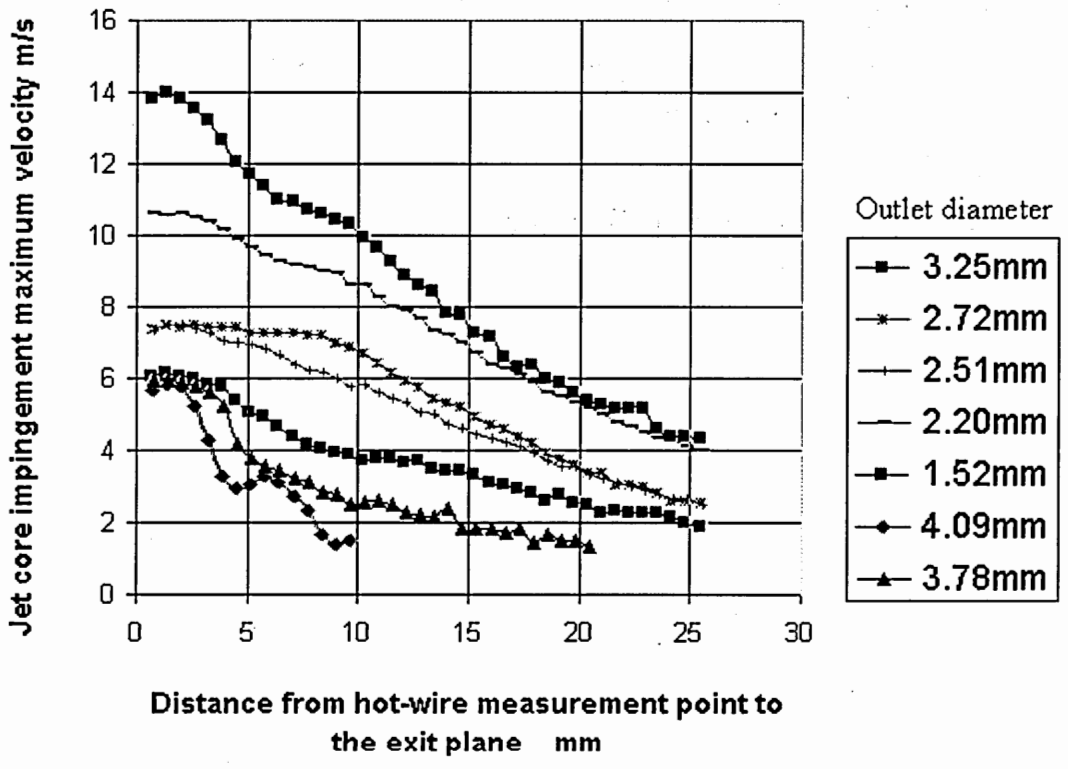

Figure 19. Jet core impingement maximum velocities vs. measurement positions for different orifice diameters

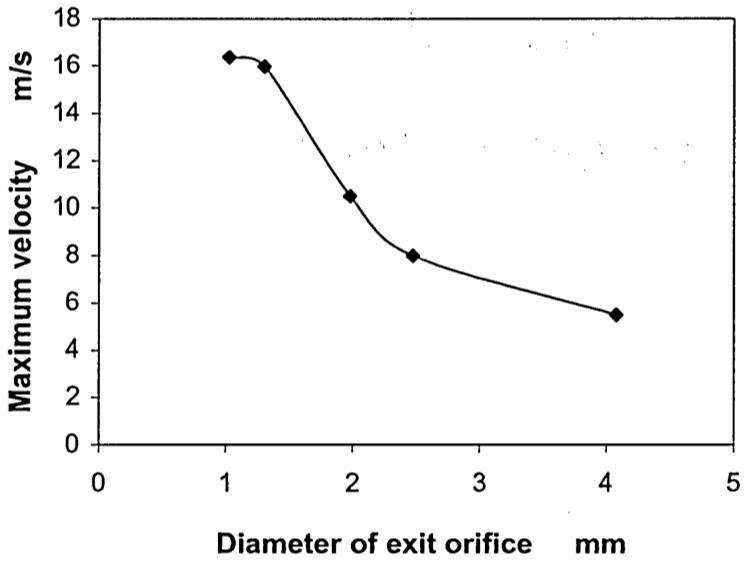

Figure 20. Outlet peak velocity magnitude vs. exit orifice size from hot-wire measurement

3.4.3 Vertical ACS Cooling Performance Test

Cooling performance is tested with constant temperature mode by using vertical ACS with the largest orifice diameter of 4.09 mm. A circular kapton heater mounted with heat sink is placed 0.8 mm away from the jet exit as the heat source (Figure 21). The heater temperature is measured by a surface attached thermocouple. The cooling performance test process is shown in Figure 22, in which first the heater is heated to a steady temperature of 70 °C. At time equals 3100 s, the jet is turned on until the temperature drops to another steady value 58 °C at time equals 4200 s. The second portion of the test involves increasing the power to the heater to reach the former steady temperature of 70 °C while the jet is operating. The increased power 0.08 W/cm^2 is equal

to the heat removed by the jet. The heat removal is low and needs to be improved. The main problem is the volumetric flow rate at the jet exit which is not sufficient to carry away the heat. A larger diaphragm diameter and higher excitation frequency are required to maximize the volumetric flow rate which can correspondingly increase the fresh air entrainment to enhance heat convection.

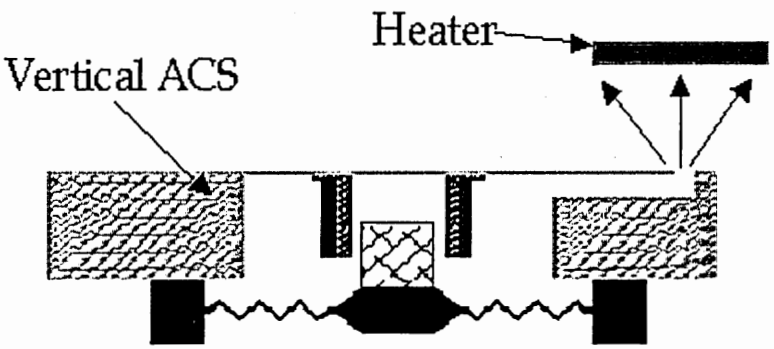

Figure 21. Vertical ACS cooling performance test setup

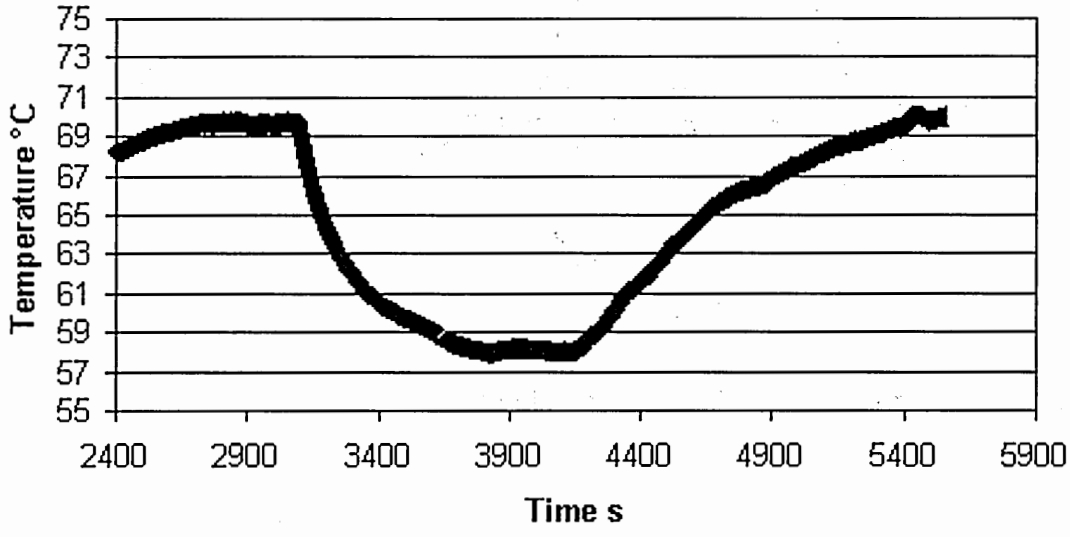

Figure 22. Vertical ACS cooling performance test process

3.5 Tangential ACS device

In the vertical ACS device, the microjet is generated vertically. The heat generating components have to be placed above the jet outlet which results in larger dimensions in the vertical direction (see Figure 21). This is not favorable due to a thicker packaging substrate. Therefore, an even lower profile design, a tangential ACS, is proposed (Figure 23). With this design, synthetic jets are generated tangentially over the substrate. Hence, the hot electronic components can be arranged in the same plane as the substrate.

In the tangential ACS design, diaphragm II with an epoxy rigid center is used. A self-supporting coil is glued on the rigid center. This coil is wound using 0.08 mm diameter copper wire with a 21 mm inner diameter and 3 mm in height. The coil has resistance of approximately 12 ohms. A 20-mm diameter Sm-Co magnet sits in the

center of a permalloy back iron. The back iron is glued at the center of substrate cavity, which has a circular recess to hold the magnet. The circular recess is 22 mm in diameter and 4 mm in depth. A permalloy lid covers the magnet. Therefore, the back iron and lid form a closed constant magnetic circuit with the permanent magnet located in the middle of the back iron. The magnet and the coil are aligned so that the coil can be driven to move in the gap between magnet and back iron after the application of AC current to the coil. The tangential ACS has a rectangular orifice of 10 mm×1 mm. Figure 23 shows the schematic of the tangential ACS design, and Figure 24 presents the fabricated ACS assembly. The vibration of diaphragm II, fluid mechanics and cooling performance of the tangential microjets are explored in the similar manner as the vertical ACS device.

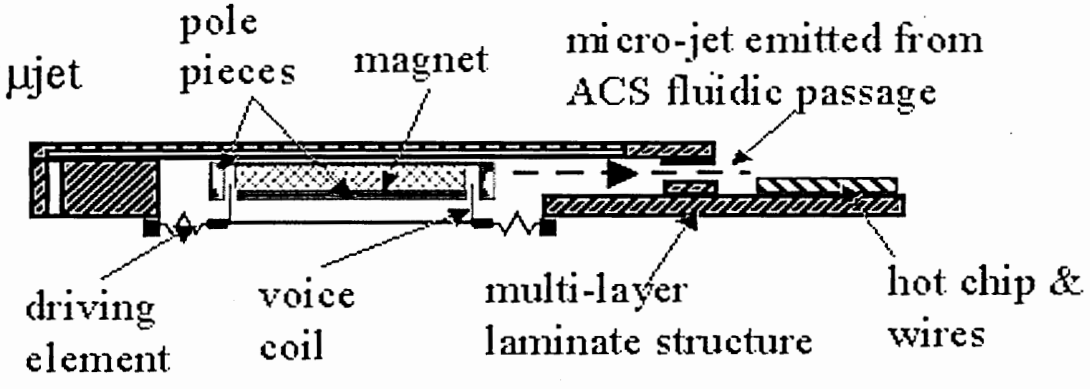

Figure 23. Schematic of a tangential ACS device

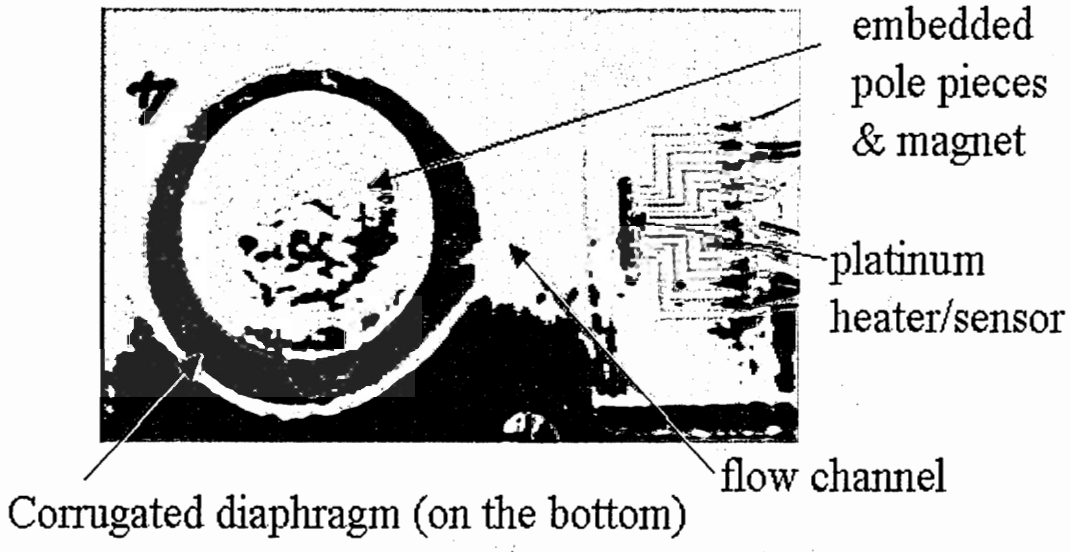

Figure 24. Assembly of a tangential ACS device

3.5.1 Diaphragm II Excitation

The deflection of diaphragm II is investigated in both the static and dynamic modes. Static mode characterization is carried out using a displacement force test station (Model 921A by TRICOR System Inc.). In this test method, a force is applied on the diaphragm by a cylindrical tip with the diameter of 2 mm and the height of 5 mm, and the displacement is measured by the movement of the tip. The results are shown in Figure 25. ANSYS simulations are also performed to provide a comparison with the experimental results. ANSYS is a finite element method (FEM) simulation tool. Due to the axis-symmetric structure of the diaphragm, a simplified 2-D model is applied to the simulations which demonstrate the cross-section cut plane of the diaphragm from the center to the outer edge as shown in Figure 26. Approximately 500 triangular meshing elements are used to grid the entire structure. Two boundary conditions are applied: one

is on the center edge which is free to move under certain forces; the other is on the outer edge of the diaphragm which is fixed without any freedom to move. The large displacement model is selected to perform the simulations. Under this scenario, different forces are added upon the center of the diaphragm, and the deflections of the diaphragm are calculated by the FEM model. In addition, the deflections calculated by characteristic Equation (3) are shown in Figure 25. As the applied force increases, the displacement increases as well. Below 0.1 N, the diaphragm is operating in a linear regime. It is observed that the experimental results are in good agreement with the predictions from ANSYS modeling and the characteristic equation up to 0.1 N. In actual use, the diaphragm is mainly operated in this linear regime (i.e. $F<0.1$ N); hence, both tools are satisfactory for design and optimization of the diaphragm in the linear regime under static mode.

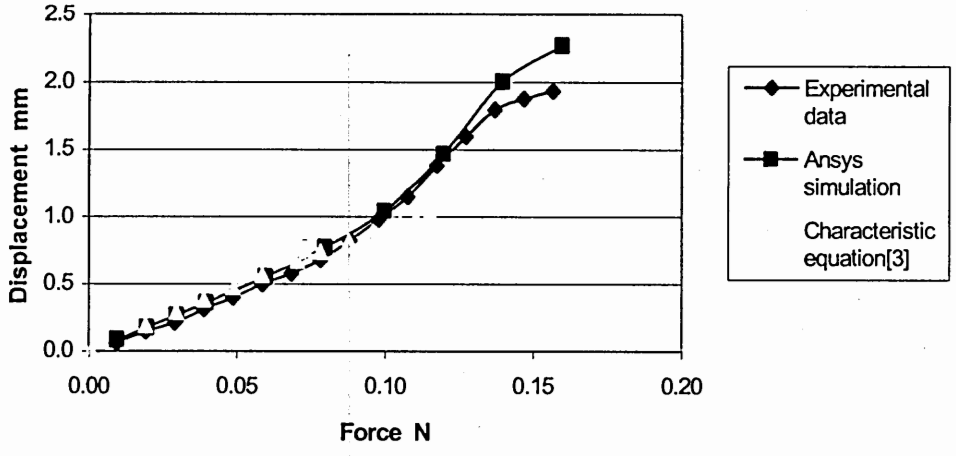

Figure 25. Displacement vs. static force of Diaphragm II-A

Figure 26. ANSYS simulation model

When driven electromagnetically, the diaphragm operates in a dynamic mode. In this case, the frequency response can be studied to find the optimal operation frequency. A laser doppler vibrometer is used which is capable of measuring a moving displacement from a remote position using interferometry techniques. Figure 27 shows the frequency response to the deflection and the phase shift. The coil driving current is maintained constant at 70 mA RMS which is much smaller than the vertical ACS driving current (180 mA); thus, the electromagnetic driving force is kept constant and the consumed driving power is 0.06 W. Deflection magnitudes are plotted on a logarithmic scale. From the figure, the frequency of 100 Hz is selected to be the optimal operation frequency. At this frequency, the deflection is approximately 0.5 mm. Above this frequency, the deflection magnitudes decay at a slope of –40 dB/decade, indicating a second order over-damped system.

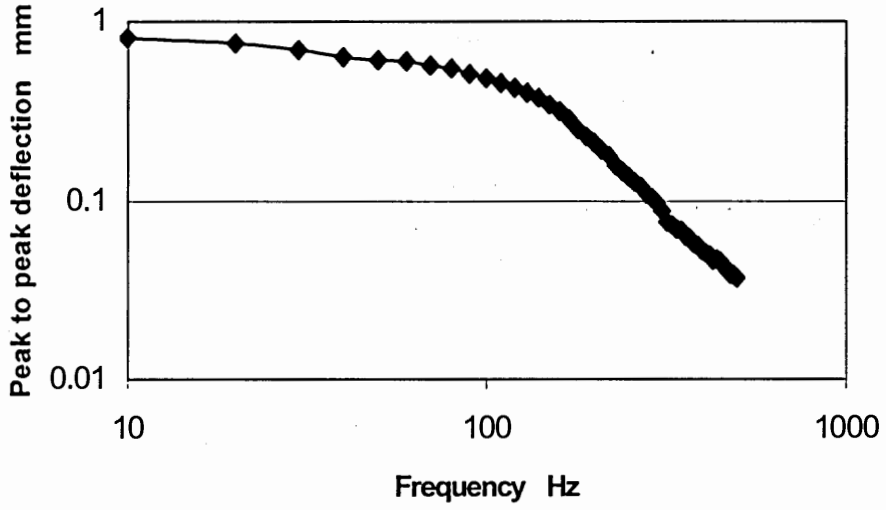

(a)

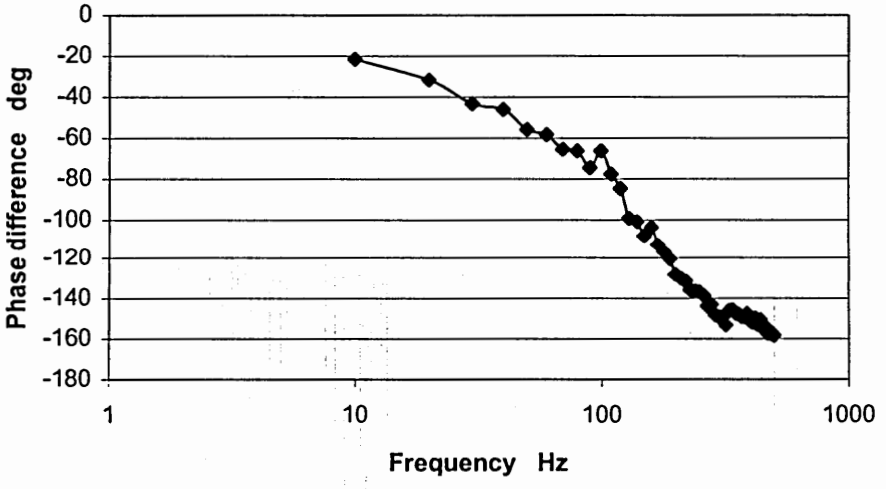

(b)

Figure 27. Frequency response of diaphragm II (a) deflection vs. frequency (b) phase difference vs. frequency

Three different diaphragm II are fabricated as II-A, II-B and II-C, molded with fluoroelastomers A, B and C respectively (see Table 1). These three types of diaphragm II are vibrated at the same driving current of 70 mA with a fluid channel outlet of 10 mm×1 mm. Figure 28 presents the deflections under different frequencies. The deflection magnitude is drawn in decibel scale. At the frequencies around 100 Hz, diaphragm II-A has much larger deflection than diaphragm II-B and II-C. Therefore, material A is the best material to generate the strongest jet under the same operation conditions. This conclusion is the same as that drawn from diaphragm I vibration test. Therefore, fluoroelastomer A is used for all the diaphragm fabrication for the tangential ACS.

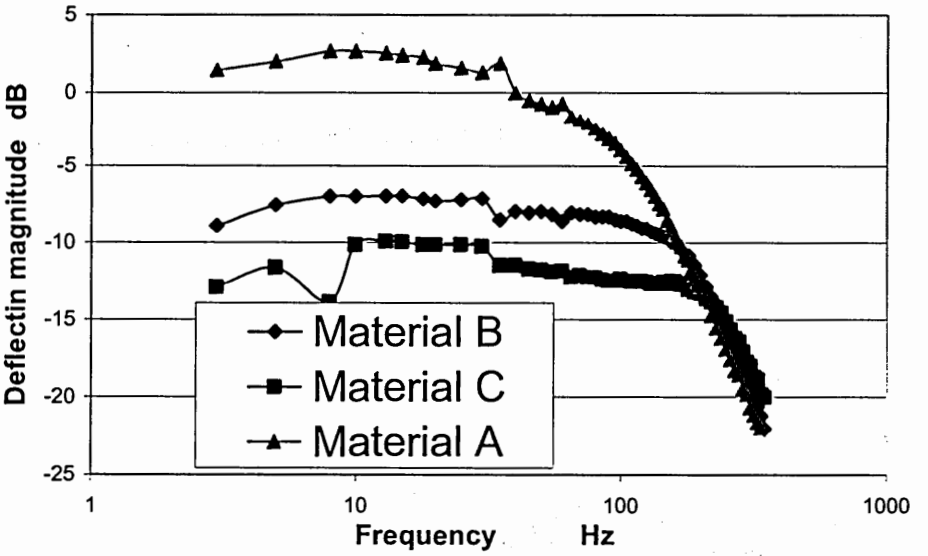

Figure 28. Influence of materials on diaphragm II

The loading effects on the diaphragm deflection are explored at the constant driving current of 70 mA with different fluidic channel exit dimensions as shown in Figure 29. All the rectangular channels have the same thickness of 1 mm, while different channel widths. As can be seen in Figure 29, there exits a loading effect. As the channel width decreases, the deflection magnitude decreases which means the loading effect becomes significant. However, this loading effect decays as the driving current frequency increases.

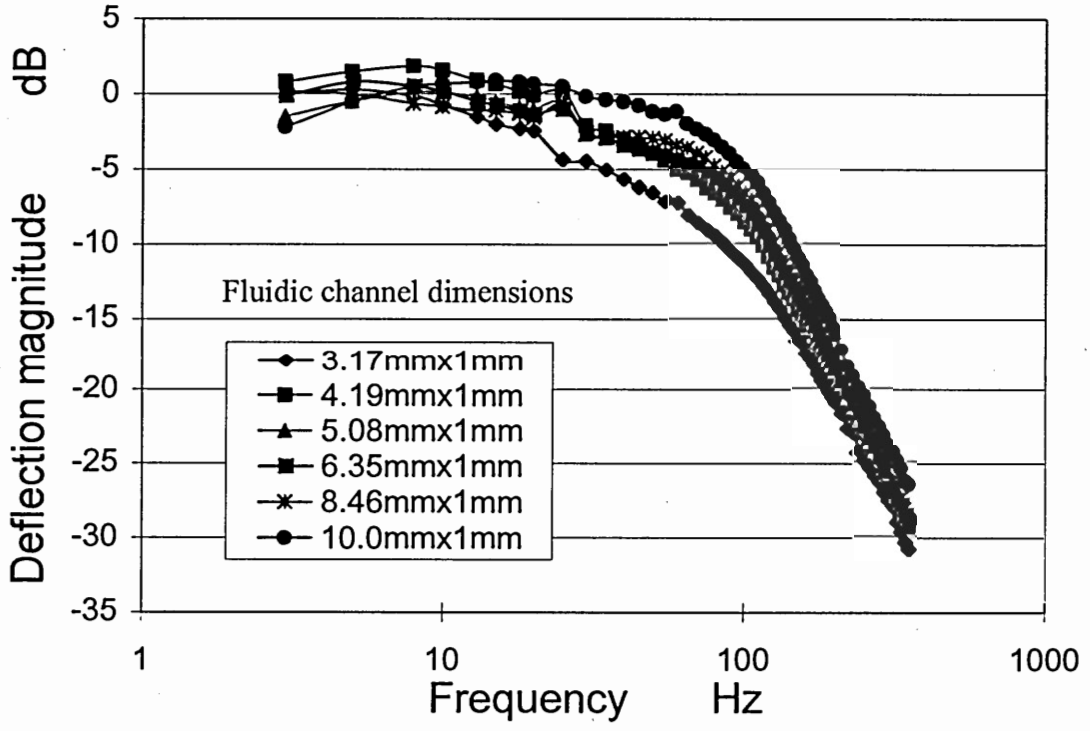

Figure 29. Frequency responses of diaphragm II-A under different loading conditions

3.5.2 Tangential ACS Fluid Mechanics Characterization

A schematic of the orientation for the PIV results is shown in Figure 30. The PIV images of airflow field for the tangential ACS in one period are shown in Figure 31. The microjet is operated under 100 Hz and coil driving current 70 mA. One vibration cycle is divided into 18 time steps; therefore, 18 images are captured in one period. Each image is on the symmetric plane of the device with Y-axis vertical to the outlet plane, X-axis parallel to the outlet. The center of the outlet is located at (3.5 mm, 19 mm). On the left side of x=3.5 mm is the board boundary on which heater is located; therefore, at $x \leq 3.5$ mm, the velocity is zero.

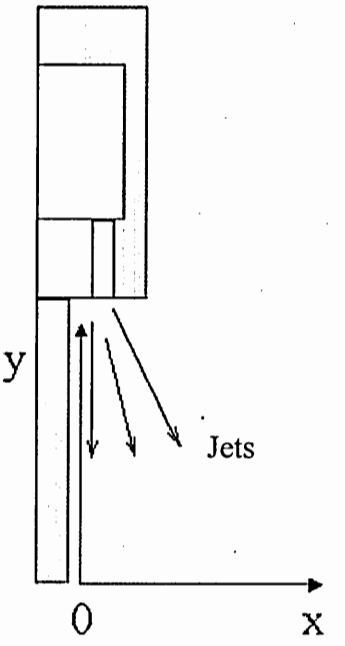

Figure 30. Schematic of tangential ACS PIV measurement

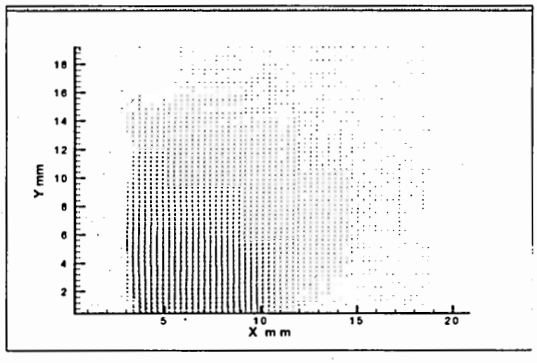

(a) *t/T=0*

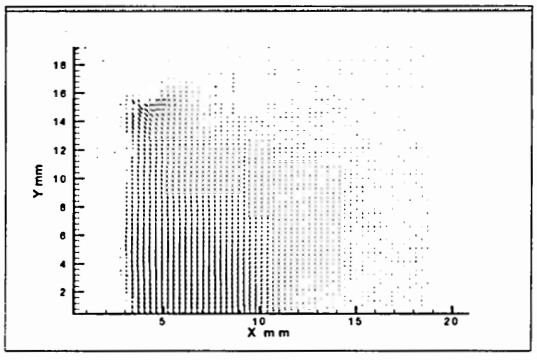

(b) *t/T=0.056*

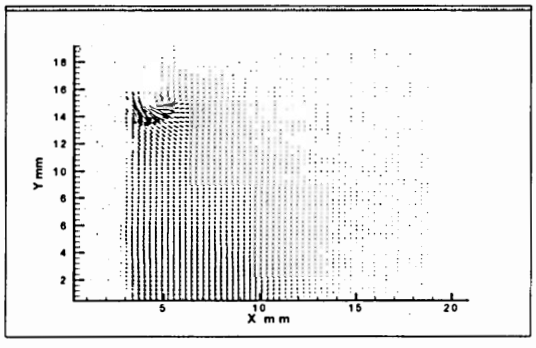

(c) *t/T=0.111*

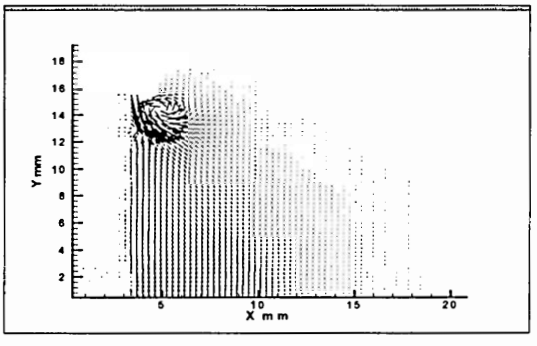

(d) *t/T=0.167*

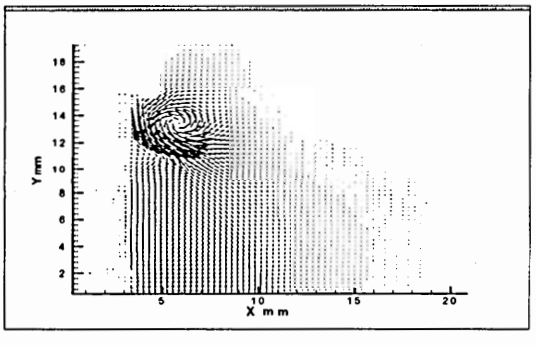

(e) *t/T=0.222*

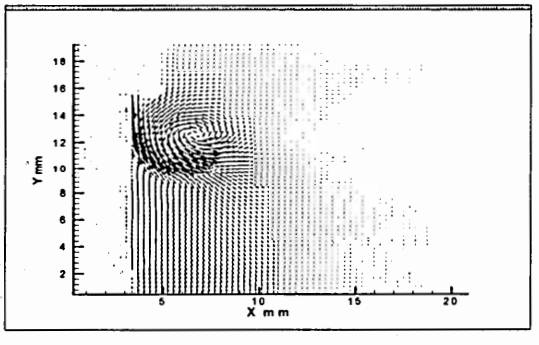

(f) *t/T=0.278*

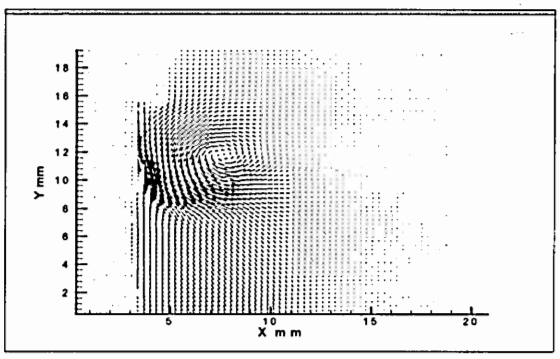

(g) *t/T=0.333*

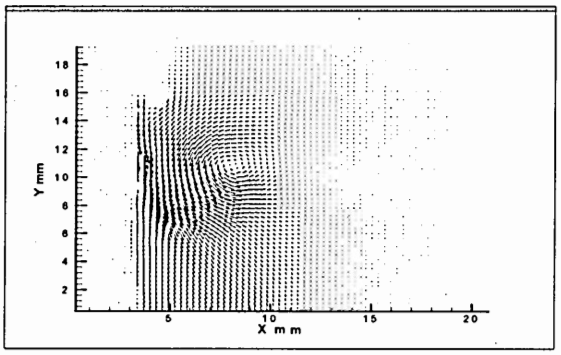

(h) *t/T=0.389*

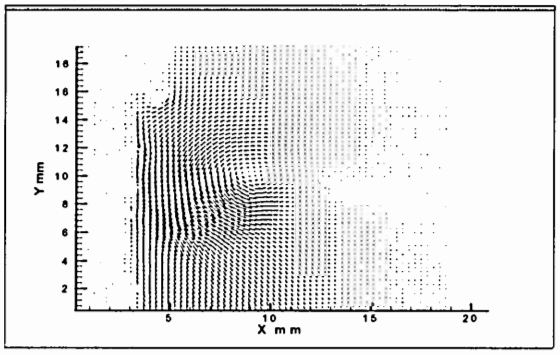

(i) *t/T=0.444*

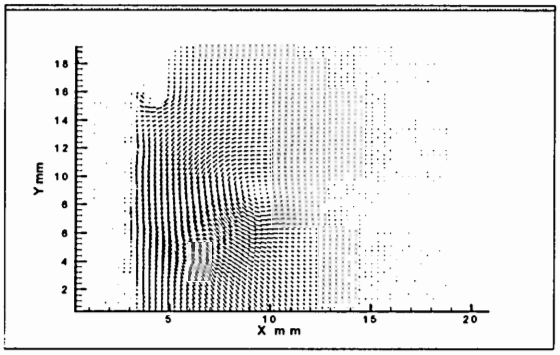

(j) *t/T=0.5*

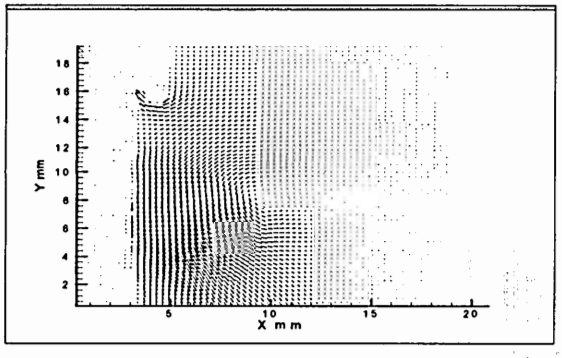

(k) *t/T=0.556*

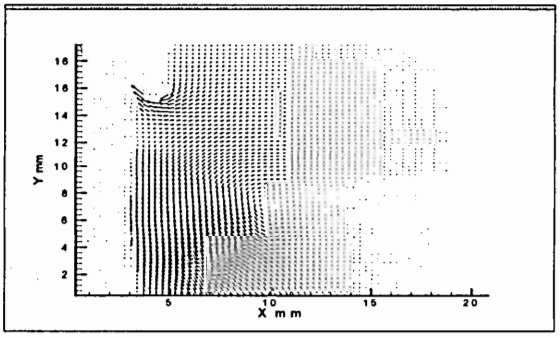

(l) *t/T=0.611*

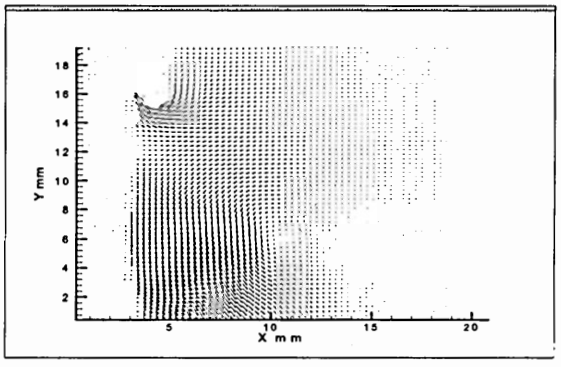

(m) *t/T=0.667*

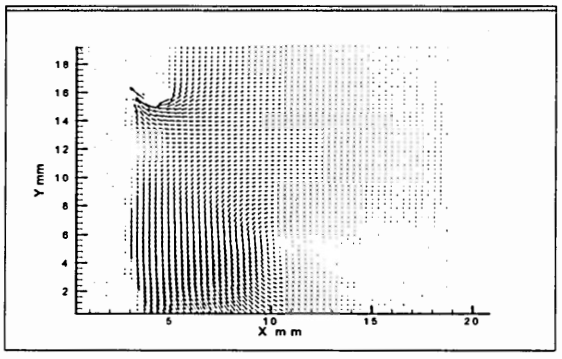

(n) *t/T=0.722*

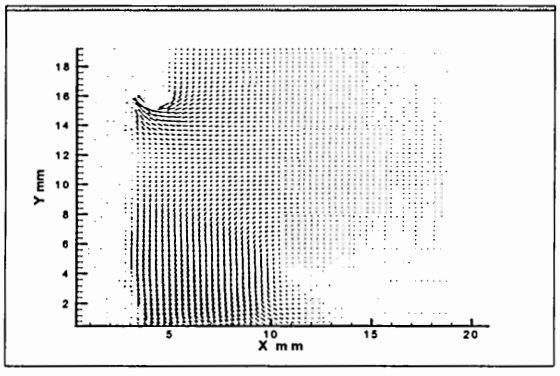

(o) *t/T=0.778*

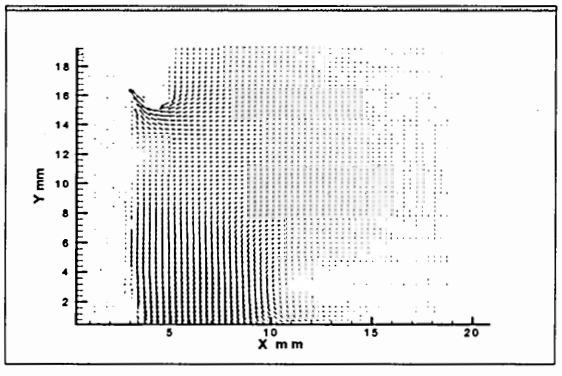

(p) *t/T=0.833*

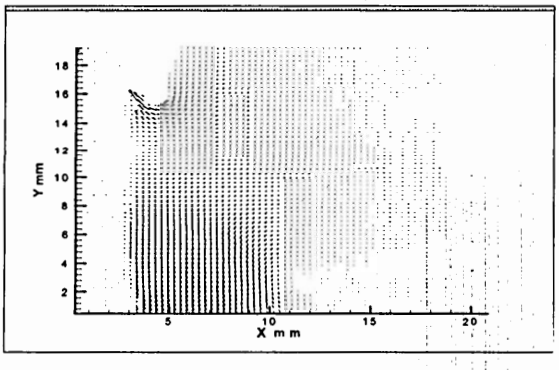

(q) *t/T=0.889*

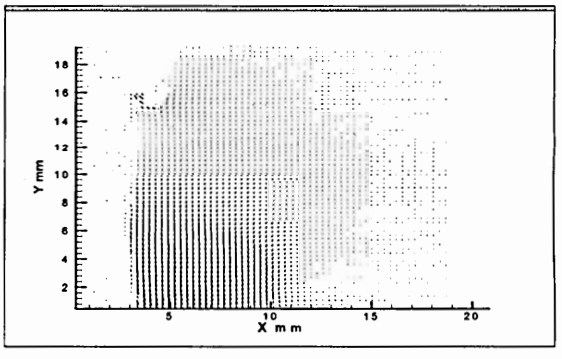

(r) *t/T=0.944*

Figure 31. Phase-locked PIV images of tangential ACS in X-Y plane taken at 18 equal intervals during the actuator cycle

Unlike the vertical ACS jet, there is only one vortex formed instead of a vortex ring. From $0<t/T<0.5$ is the impingement stroke. The vortex is formed, rolls downward, and later breaks up at the end of the impingement stroke. From $0.55<t/T<0.94$ is the intake stroke. Another vortex tries to form at the outlet due to the intake air, while the primary vortex transits into turbulence and advects downstream. The velocity magnitude decreases as the distance from outlet increases.

The jet output velocity magnitude is measured by hot-wire anemometry at a position of 0.8 mm from the jet outlet. The microjet is operated at 100 Hz and at a coil driving current of 70 mA. Figure 32 illustrates the phase-averaged centerline velocity in one cycle. At the full impingement position, the positive peak velocity is about 14 m/s. At the full intake position, the negative peak velocity is about 5 m/s. The time-averaged velocity is approximately 2.7 m/s. The magnitude differences between these two maxima indicate the amount of air that is carried away from the channel exit. Therefore, it is desirable to have a larger difference between the two maxima which will result in greater net heat dissipation by the air jet.

3.5.3 Tangential ACS Cooling Performance Test

The cooling performance is tested in a constant temperature mode. The heat-emitting source is a platinum film heating element array fabricated on a silicon chip (Yoon et al., 2001). This 8 mm×1.2 mm array has 100 elements (Figure 33). The heater chip itself is calibrated to be a temperature sensor because of the linear relationship between its resistance and temperature. The characterization curve is shown in Figure 34. When the characterization is conducted, the heater array is placed in an oven. A very

small current is supplied through the heater array. The voltage across the elements in the middle portion of the heater is measured. Then, the resistance is calculated under different temperatures. When the heater is applied to monitor a certain chip temperature, the same middle portion which has been calibrated should be used to calculate the resistance and then determine the corresponding temperature.

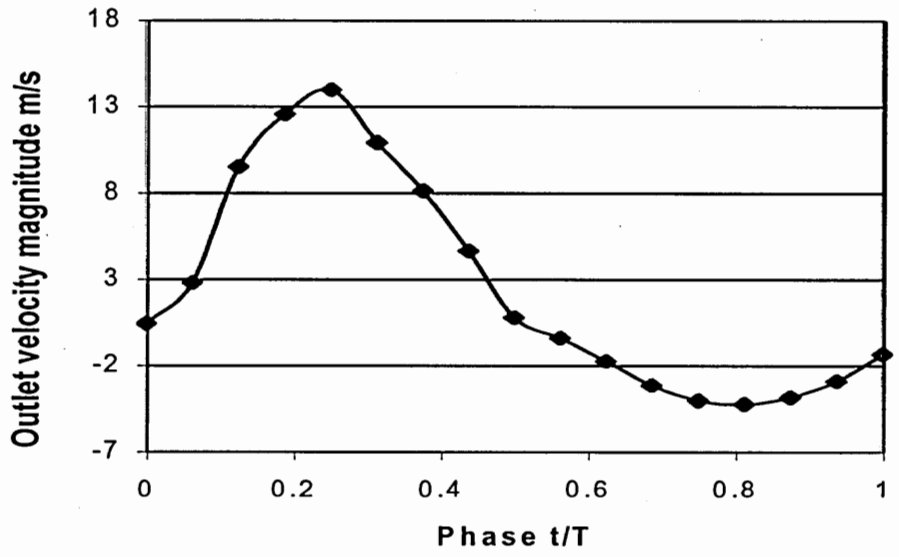

Figure 32. Phase-averaged centerline velocity during one cycle of the tangential ACS

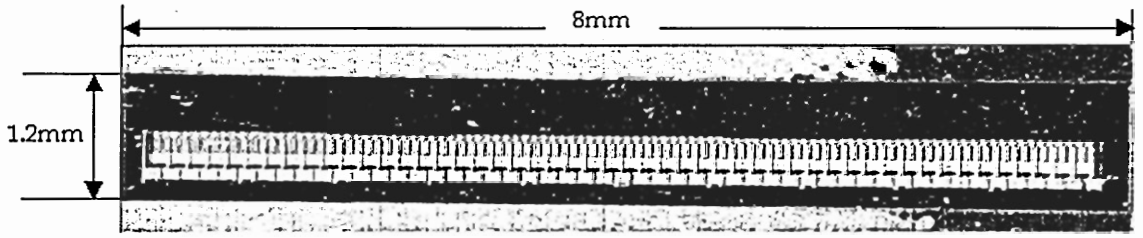

Figure 33. Pt heater/sensor array

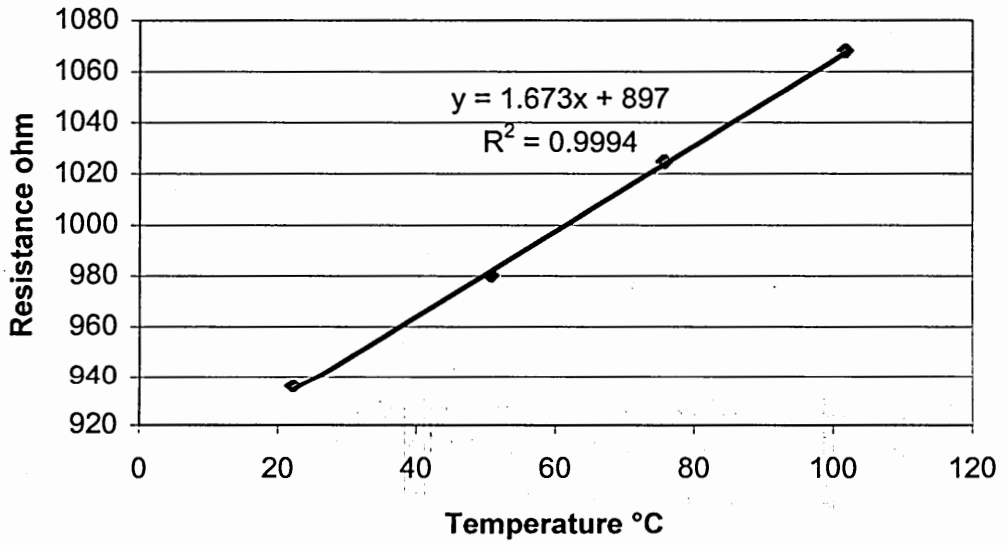

Figure 34. Calibration curve of the heater array

The cooling performance measurement is shown in Figure 35, in which first the heater is heated to a steady temperature of 100 °C. Then the jet is turned on until the temperature drops to its new steady-state value of approximately 70 °C. The third step of the test involves increasing the power to the heater to reach the former steady temperature of 100 °C while the jet is operating. All the heater temperatures are identified by the measurement of the heater resistance. Based on the increased power input to the heater array, a heat flux removal of 3.6 W/cm^2 is achieved at a coil power consumption of approximately 60 mW. Without surface enhancement (e.g. heat sinks), at temperature differences of up to 80 °C, traditional air forced convection achieves surface heat flux of 1 W/cm^2 (Kim et al., 1996) with a power consumption of 480 mW. The tangential ACS offers cooling performance within the same order of magnitude as conventional fans. In addition, there are advantages of the ACS device which include real estate issues, power requirements and the zero-net-mass flux feature.

3.5.4 A Comparison of the Vertical ACS and the Tangential ACS

Two ACS prototypes are presented in this chapter. They have different orientations which cause different synthetic jets generation phenomena. This section compares their structures and functions.

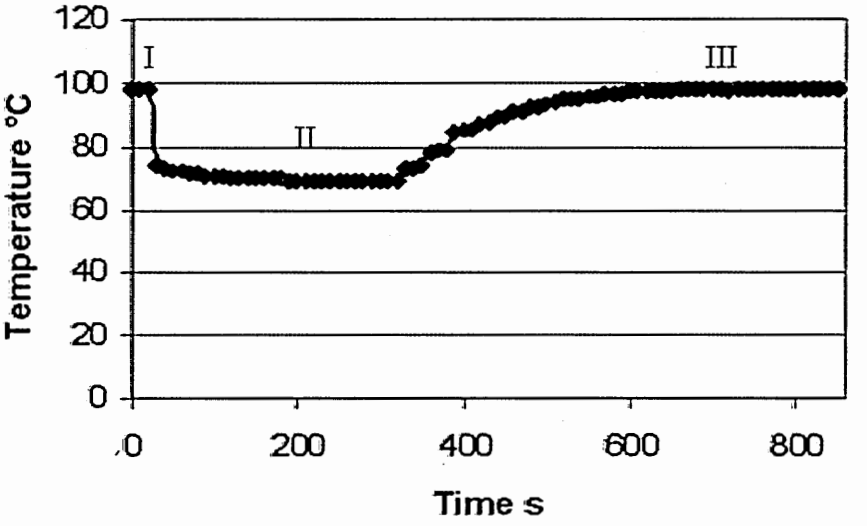

Figure 35. Tangential ACS cooling performance test process

In diaphragm II, the outer diameter is enlarged from 16 mm to 33 mm and the rigid center is enlarged from 5 mm to 24 mm compared with Diaphragm I. In addition, the rigid center material is replaced by the low density epoxy prepreg, and the self-supporting coil instead of the magnet is mounted on the diaphragm which helps to maintain a low mass diaphragm system. The corrugation structure is changed as well. All these variations on the diaphragm design result in a larger diaphragm surface area and a higher resonance frequency. Diaphragm II has a resonance frequency of 100 Hz which is 100% greater than the resonance frequency for Diaphragm I. Based on the diaphragm dimensions, the resonance frequency and the deflection at resonance, the volumetric flow rate during the impingement stroke of the synthetic jets can be calculated by equation (2). The vertical ACS has a volumetric flow rate of 1.49×10^{-5} m^3/s, and the tangential ACS has a volumetric flow rate of 6.43×10^{-5} m^3/s. Another advantage of the diaphragm II is

the dramatic reduction on the required driving current. The vertical ACS requires a driving current of 180 mA, and the tangential ACS only needs about 70 mA. Hence, the power consumption is greatly reduced with the tangential ACS device.

As discussed before, maximizing the jet volumetric flow rate is critical to the heat removal. The volumetric flow rate includes the initial jet flow rate generated from the ACS actuator and the entrained jet flow rate from the device surrounding environment. The jet in the vertical ACS develops vortex rings at the exit and entrains the surrounding air from all the directions. The jet in the tangential ACS only generates one vortex at the exit due to the compact space. However, this weakness is compensated by the larger initial jet flow rate in the tangential ACS. A comparison between vertical ACS and tangential ACS is summarized in Table 4. In conclusion, the tangential ACS has a more compact design and has better cooling performance.

3.6 Tangential ACS Optimization

There are two important structures of an ACS device: the actuator and the fluid channels in the printed wiring board. The actuator design has been discussed in detail in the previous sections. The fluidic channels embedded in the PWB can also affect the linear velocity at the exit and determine the synthetic jet flow pattern at downstream. In this section, the impact of different fluidic channel sizes on the cooling performance of the tangential ACS is explored.

Table 4. Comparisons between vertical ACS and tangential ACS

Device properties	Vertical ACS	Tangential ACS
Diaphragm OD (mm)	16	33
Rigid center size (mm)	5	24
Rigid center material	Fluoroelastomer	Epoxy prepreg
Actuator arrangement	Stationary coil, Moving magnet	Stationary magnet, Moving coil
Resonance frequency (Hz)	50	100
Deflection at resonance (mm)	3.16	1
Volumetric flow rate (m^3/s)	1.49×10^{-5}	6.43×10^{-5}
Cooling performance (W/cm^2)	0.08	3.6
Power consumption (mW)	259	60

3.6.1 Tangential ACS Testbed

An active cooling substrate testbed has been designed to investigate the outlet dimensional effects. The testbed has one tangential ACS device with six different rectangular fluidic channels connected to the center cavity (Figure 36). The channel dimensions are listed in Table 5. The distance from cavity center to the exit is 31 mm. The thickness the channel is 1 mm. Variations of the channel width will change the hydraulic diameter D_h which is defined by Equation (8):

$$D_h = \frac{2t_h w}{t_h + w} \tag{8}$$

where t_h is the channel thickness and w is the channel width. D_h can influence the exit linear velocity, and the Reynolds number based on this length scale. The advantage of the testbed design is to ensure the same electromagnetic drive and the same cavity structure are applied in each case study. The only changing factor is the channel dimension. When one channel is under test, the other channels are blocked by room temperature vulcanizing (RTV) silicone. When another channel is expected to be tested, the rigid cavity top cover can be removed and the channel to be tested can be opened by simply removing the RTV. The top cover plate can be resealed by glue or RTV. Based on the prior tangential ACS research (section 3.5), a coil driving current consisting of a sine wave AC current with the root mean square magnitude of 70 mA and frequency of

100 Hz is applied. The total power consumption is about 60 mW. To characterize the microjet cooling performance, a standard silicon based platinum heat array is used. The rectangular heater array is 8 mm×1.2 mm which is the same heater used in the tangential ACS cooling performance test. The heater chip functions as a heat generating component to mimic the thermal output of an integrate circuit and as a temperature sensor since the heater resistance is a direct function of temperature.

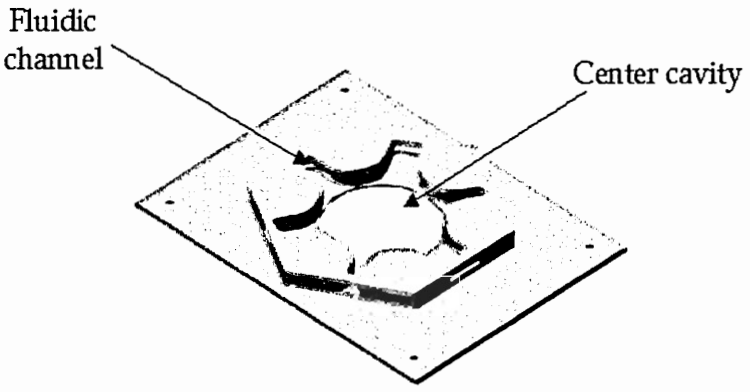

Figure 36. Tangential ACS testbed substrate

Table 5. Different fluidic channel dimensions

Channel Exit Number	Channel Width (mm)	Hydraulic Diameter (mm)
1	8.46	1.79
2	5.08	1.67
3	6.35	1.73
4	3.175	1.52
5	10	1.82
6	4.19	1.62

3.6.2 Testbed Fluid Mechanics Characterization

The velocity downstream of each testbed channel exit is measured by a hot-wire anemometer. For each exit, five different measurement positions are selected. They are located at 0.80 mm, 4.23 mm, 6.35 mm, 10.16 mm and 15.24 mm away from the channel exit. Figure 37-42 present the centerline velocity magnitude in one cycle at different channel exits downstream. Some basic trends can be observed from the plots. The centerline velocity magnitude decreases as the distance from the exit is increased. For different channel dimensions, the linear velocity decreases with an increase in the channel width because the same ACS operation conditions are applied in each case study. In one vibration cycle, the peak impingement velocity is normally larger than the peak intake velocity which indicates net jet flow propagation downstream. At some locations, the intake velocity is too low and is flattened because it is smaller than the sensitivity of the hot-wire measurement. In that case, the velocity is approximated as 1 m/s.

The local average velocities can be calculated by Equation (9):

$$u = \frac{\int_0^T u_0(t)dt}{T} \tag{9}$$

where T is the vibration period, $u_0(t)$ is the centerline velocity at each time step. The calculated average velocities are listed in Table 6. Based on the hydraulic diameter D_h

(Table 5) and the local average velocity u (Table 6), the local Reynolds number Re can be calculated by Equation (10):

$$\mathrm{Re} = \frac{D_h u \rho}{\mu} \tag{10}$$

where ρ is air density and μ is air viscosity at room temperature (22 °C). The calculated local Reynolds numbers are listed in Table 7.

3.6.3 Testbed Cooling Performance Test

The cooling performance is tested in a constant temperature mode. First, the heater is ramped to a steady temperature of 100 °C (I). Then the ACS jet is turned on until the temperature drops to its new steady-state value of approximately 70 °C (II). The third step of the test involves increasing the power to the heater to reach the former steady temperature of 100 °C while the jet is operating (III).

The chip temperature is determined by the resistance measurement. The temperature distribution on the ACS is simultaneously mapped by an infrared camera as shown in Figure 43 and 44. Figure 43 is the top view (the side with the heater attached) of the temperature contour; Figure 44 is the bottom view (the side only has PWB without the heater) of the temperature contour. For the measurements shown in Figure 43 and 44, the heater is located at 0.8 mm away from the channel 1 exit. Similar cooling performance tests are conducted at the other exit locations as designed in Table 6.

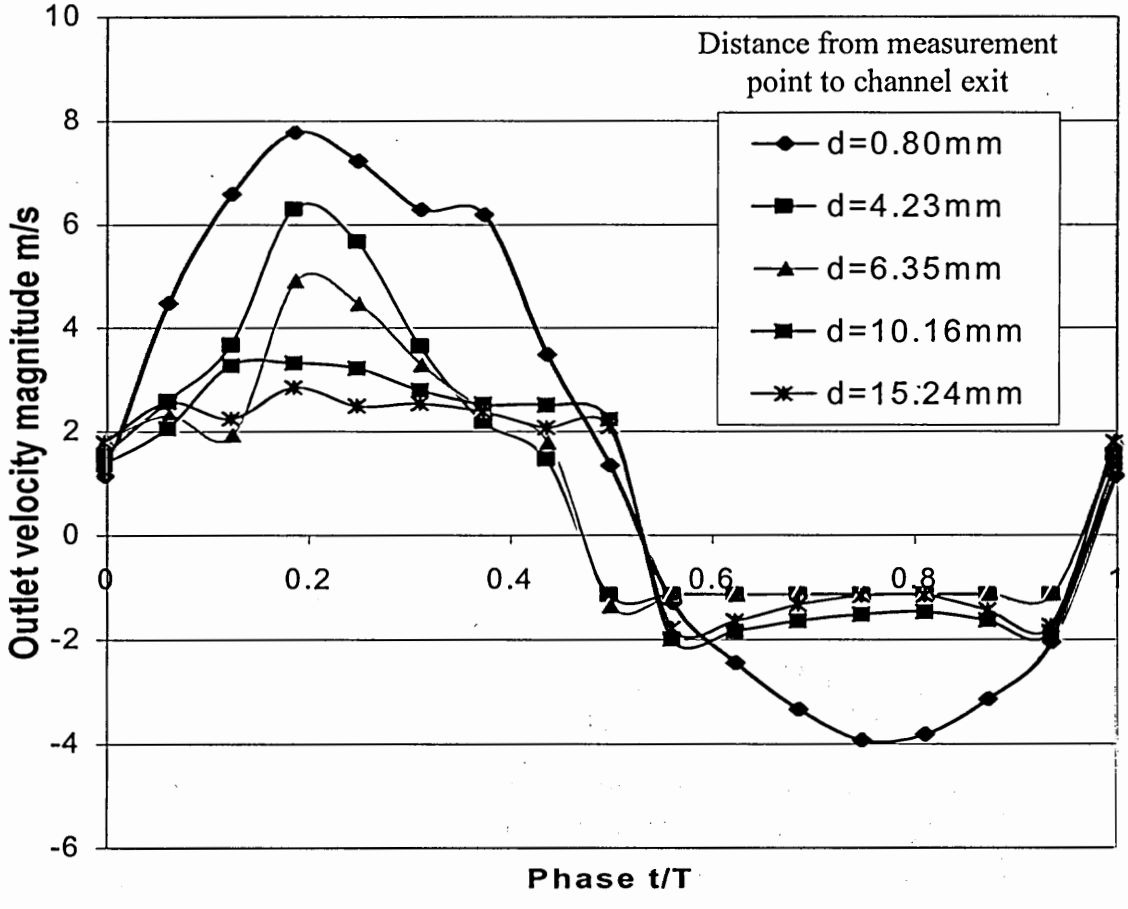

Figure 37. Phase-averaged centerline velocity during one cycle at the exit of fluidic channel 1 (w=*8.46* mm)

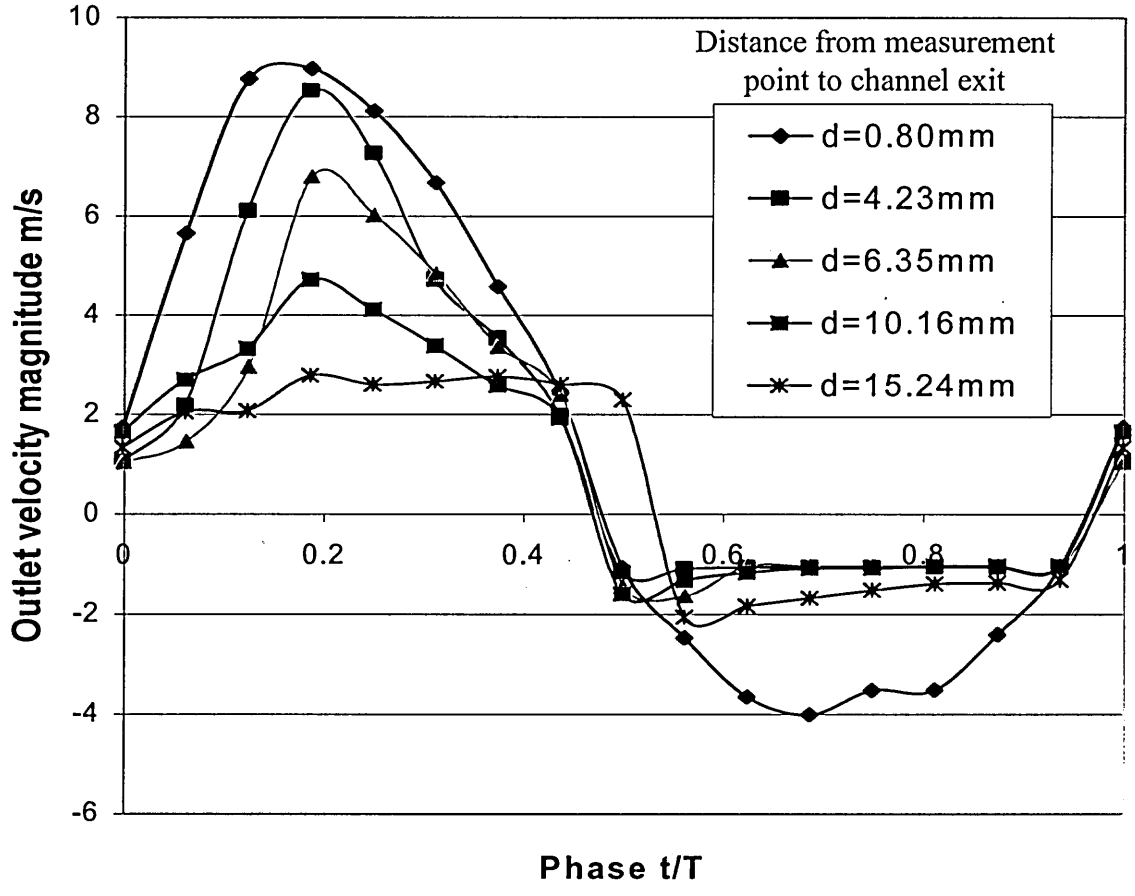

Figure 38. Phase-averaged centerline velocity during one cycle at the exit of fluidic channel 2 (w=5.08 mm)

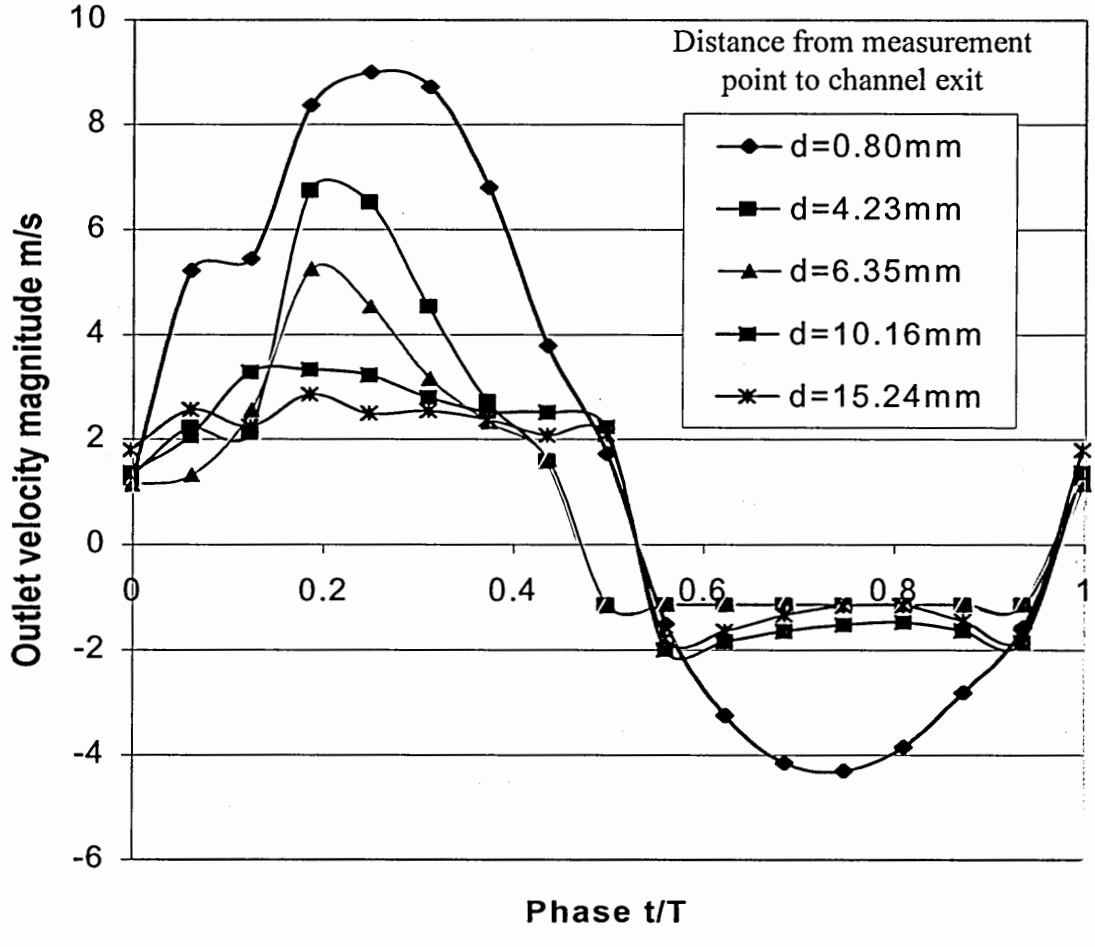

Figure 39. Phase-averaged centerline velocity during one cycle at the exit of fluidic channel 3 (w=*6.35* mm)

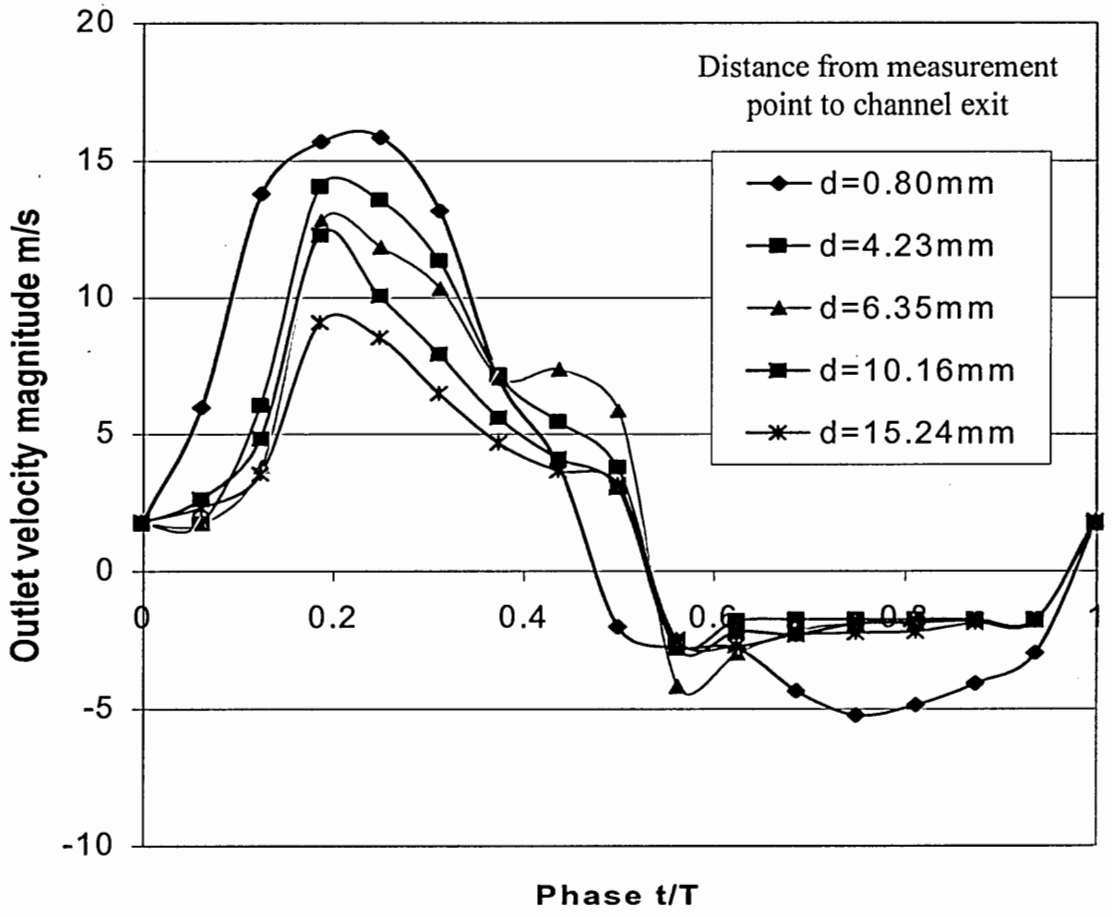

Figure 40. Phase-averaged centerline velocity during one cycle at the exit of fluidic channel 4 ($w=3.175$ mm)

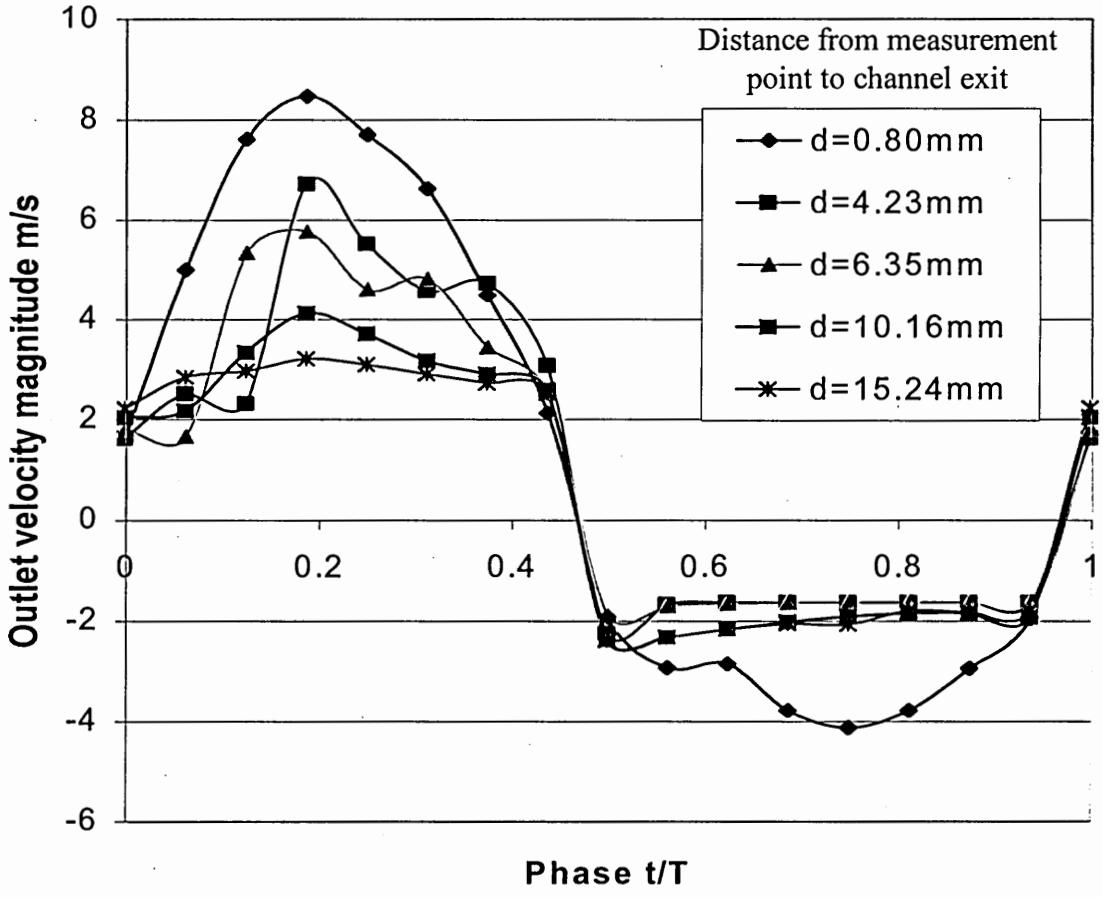

Figure 41. Phase-averaged centerline velocity during one cycle at the exit of fluidic channel 5 ($w=10$ mm)

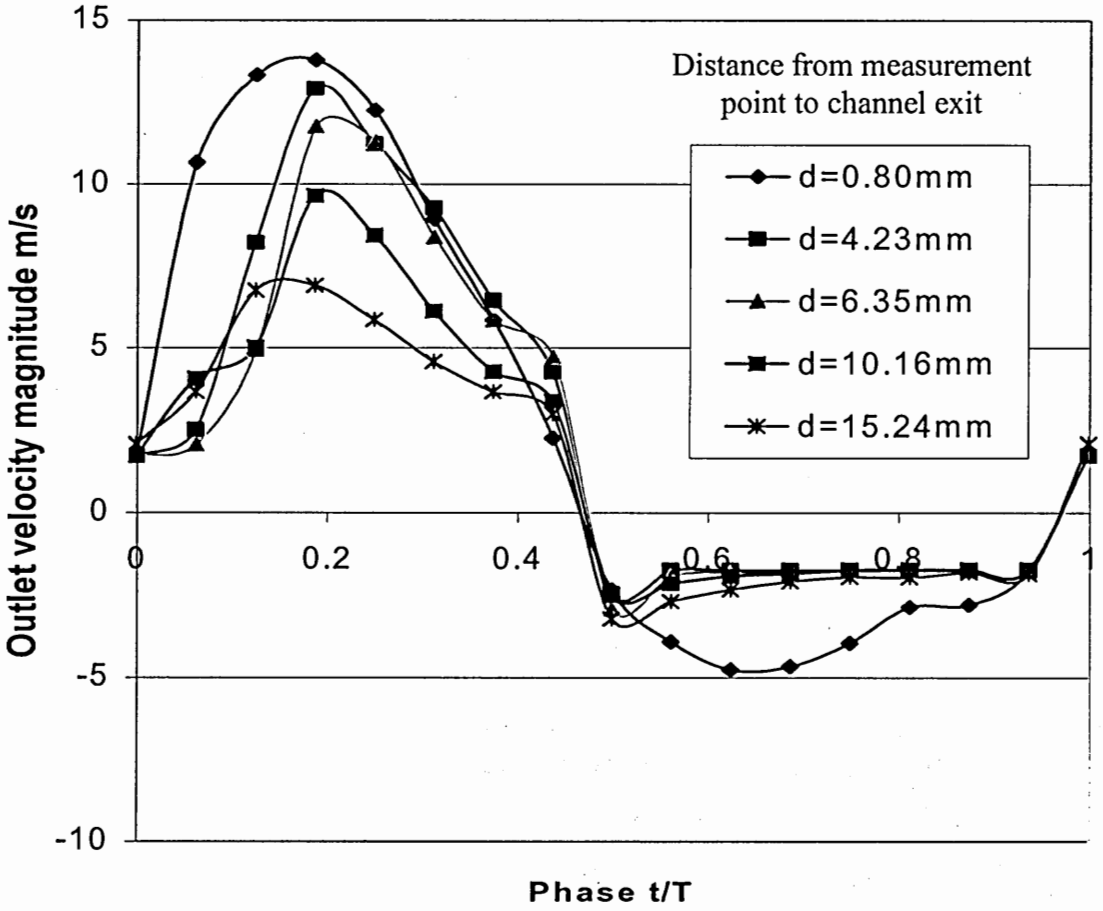

Figure 42. Phase-averaged centerline velocity during one cycle at the exit of fluidic channel 6 (w=*4.19* mm)

Table 6. Average centerline velocities at different exit locations

Fluidic Channel Number	Channel Width (mm)	0.80 mm to Channel Exit (m/s)	4.23 mm to Channel Exit (m/s)	6.35 mm to Channel Exit (m/s)	10.16 mm to Channel Exit (m/s)	15.24 mm to Channel Exit (m/s)
1	8.46	1.53	1.10	0.80	0.68	0.67
2	5.08	1.47	1.69	1.24	0.92	0.61
3	6.35	1.77	1.13	0.80	0.58	0.39
4	3.175	3.02	3.22	2.94	2.29	1.72
5	10	1.19	1.09	0.98	0.46	0.38
6	4.19	2.71	2.59	2.2	1.71	1.15

Table 7. Local average Reynolds number

Fluidic Channel Number	Channel Width (mm)	0.80 mm to Channel Exit	4.23 mm to Channel Exit	6.35 mm to Channel Exit	10.16 mm to Channel Exit	15.24 mm to Channel Exit
1	8.46	171.0295	122.9624	89.42716	76.01309	74.89525
2	5.08	153.528	176.5049	129.5066	96.08553	63.70888
3	6.35	191.148	122.0323	86.39456	62.63605	42.11735
4	3.175	287.0808	306.0928	279.476	217.6871	163.503
5	10	135.2366	123.8722	111.3713	52.27634	43.1848
6	4.19	273.4928	261.3824	222.0237	172.573	116.0578

The temperature can also be measured by a thermocouple. However, to map the temperature distribution, a large number of the thermocouples are needed. A thermocouple has a pair of metal wires which have high thermal conductivity. If a large number of thermocouples are placed on board, they will dissipate a significant amount of heat and result in measurement errors. Another drawback of thermocouples is the impact on the jet flow development due to the intrusions of the thermocouples into the flow field. Compared with thermocouples, the infrared thermography is a non-invasive measurement technique.

A ThermaCAM PM180 (Inframetrics Inc.) infrared camera is used. It has the sensitivity of ±0.07 °C. When infrared camera is used, the measurement material emissivity must be determined. Since the PWB board surface is partially covered by copper traces, the emissivity is not uniform on the entire surface. In the experiment, a thin electrical insulation tape is used to cover the board surface. The dark tape has the known emissivity value of 0.95. The infrared camera measurement technique is verified by using a thermocouple.

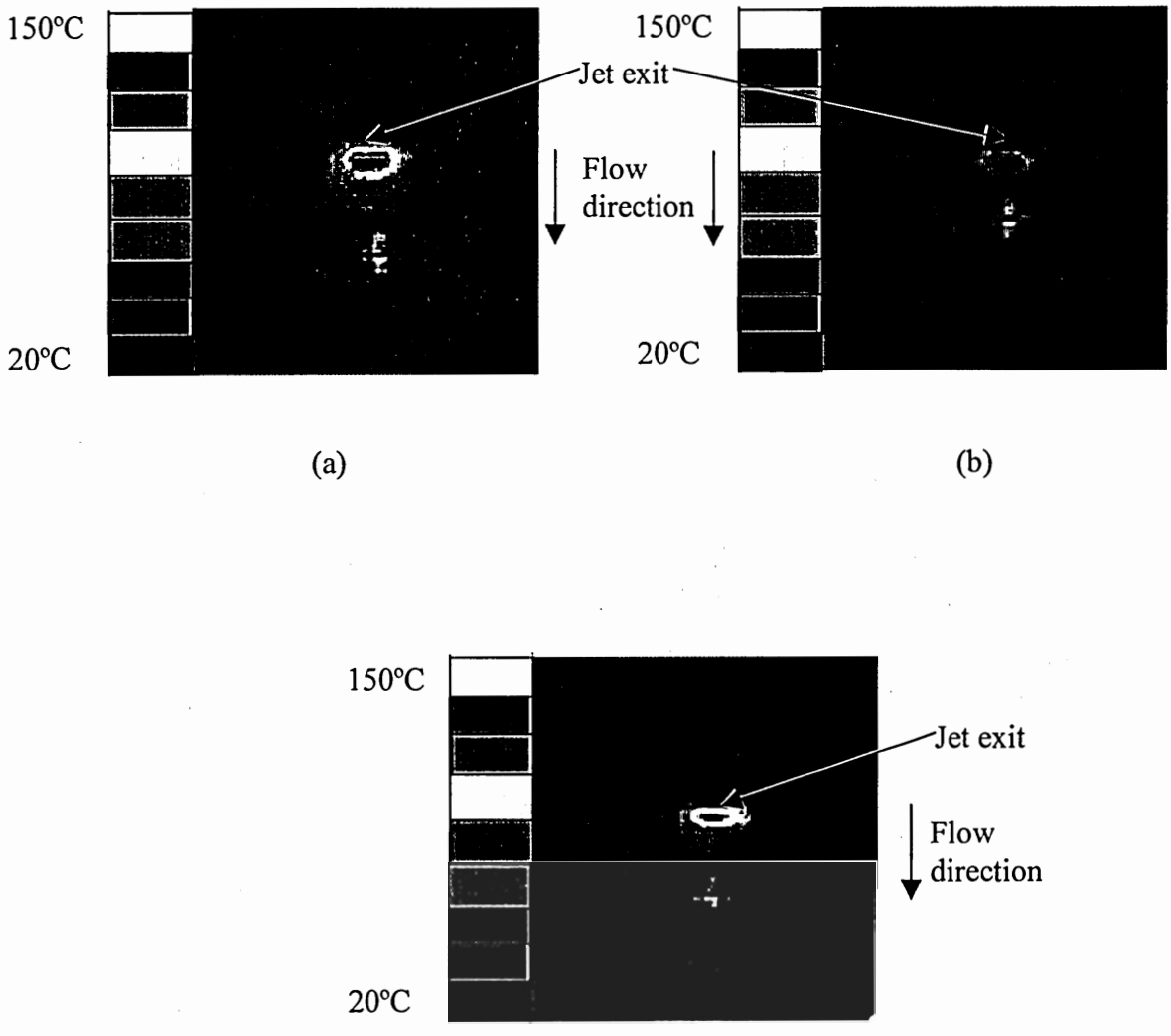

Figure 43. Temperature distribution on PWB substrate top surface in one cooling test cycle (a) state I: without jet, heater at 100 °C (b) state II: with jet, heater at 70 °C (c) state III: with jet, heater at 100 °C

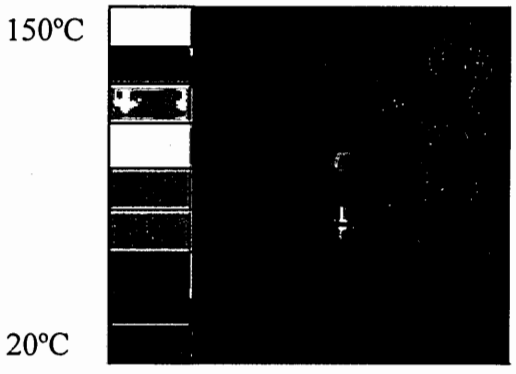

(a)

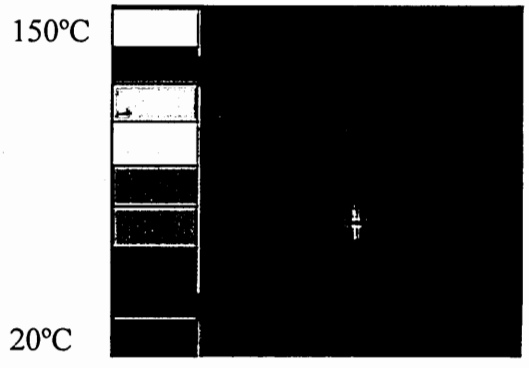

(b)

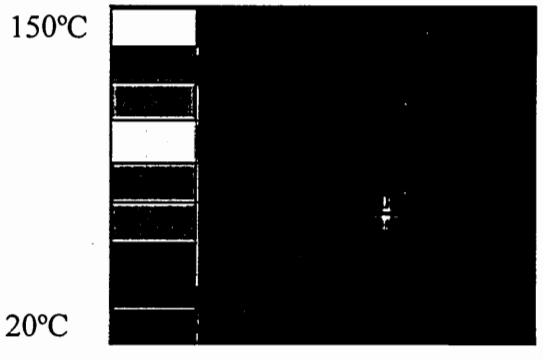

(c)

Figure 44. Temperature distribution on PWB substrate bottom surface in one cooling test cycle (a) state I: without jet, heater at 100 °C (b) state II: with jet, heater at 70 °C (c) state III: with jet, heater at 100 °C

Based on the temperature distribution at the steady state II and III during a cooling performance test, the local heat transfer coefficient at the heater location can be calculated by Equation (11):

$$P_h = \overline{h_1} A_1 (\overline{T_1} - T_0) + \overline{h_2} A_2 (\overline{T_2} - T_0) \tag{11}$$

$$\overline{T_2} = \frac{\int T_2 dA}{A_2} \tag{12}$$

where P_h is the heat dissipated from the heater array which can be calculated by the current through the heater and the voltage across the heater. At steady state II and III, because of the energy conservation, the power input to the heater is finally dissipated from all the surfaces of the ACS device through convection. $\overline{h_1}$ is the local average heat transfer coefficient at the heater location, A_1 is the surface area of the heater, $\overline{T_1}$ is the heater average temperature based on the measurement of the heater resistance, T_0 is the bulk flow temperature which is selected as the room temperature, A_2 is the ACS surface area excluding the heater area, $\overline{h_2}$ is the local average heat transfer coefficient on the area of A_2, $\overline{T_2}$ is the average temperature on the area of A_2. $\overline{T_2}$ is calculated by Equation (12) which requires gridding the surface area into small elements and reading the individual element temperature from the thermal contour maps. The heater dimensions

are selected as the reference length scales which are accurately known as 8 mm×1.2 mm. Having two steady states (II and III) and two unknowns $\overline{h_1}$ and $\overline{h_2}$, Equation (11) can be solved to obtain the local average heat transfer coefficient at the heater location. This method depends on the assumption that the fluid mechanics of a specific synthetic jet defines certain jet heat transfer capability (i.e. the flow pattern dominates the heat transfer phenomena and the jet heat convection is independent of the heater temperature). This assumption is valid because the heater temperature difference between the two steady states is not large enough to dramatically change the airflow physical properties (i.e. density and viscosity) and the bulk airflow reference temperature is selected as the room temperature, independent of the heater temperature. Major errors of this heat transfer coefficient calculation are from the average temperature $\overline{T_2}$ because the accurate pixel by pixel temperature reading can not be obtained from the IR camera images. $\overline{T_2}$ is estimated based on larger temperature contour areas (compared with the IR camera pixel size) which may cause some errors. The relative errors are less than 10%.

The calculated local heat transfer coefficients are plotted in Figure 45. Observation of Figure 45 indicates the local heat transfer coefficients have two local maxims. The first maximum is the position near the exit which is the primary optimal cooling location. The high heat transfer coefficient is caused by the high linear velocity at the exit. The second maximum is the position where 6-10 mm away from the exit which is the secondary optimal cooling location. It is believed that the secondary optimal position is where the vortex ring is fully developed and transits to turbulent flow. The higher turbulence contributes to the local heat transfer. The secondary optimal location can be

related to a characteristic length scale L_0 which is referred to stroke length and defined by Equation (13):

$$L_0 = \int_0^{T/2} u_0(t)dt \tag{13}$$

where $u_0(t)$ is instantaneous velocity at the exit on the impingement stroke which is approximated by the velocity measured at the location of 0.8 mm away from exit by hot-wire. The calculated L_0 values for different channels are listed in Table 8. In addition, from Figure 45, the optimal channel width can be obtained at about 4.191 mm which has the best cooling performance. When the orifice dimension is small, the flow viscous effects become important (Rathnasingham et al., 1997). The effective flow area is smaller than the actual channel exit area. Therefore, the volumetric flow rate is reduced. When the orifice dimension is large, the viscous effects diminish. Mass conservation requires the flow velocity should decrease proportionally to the orifice area. Therefore, there is an optimal fluidic channel dimension for a given actuator design.

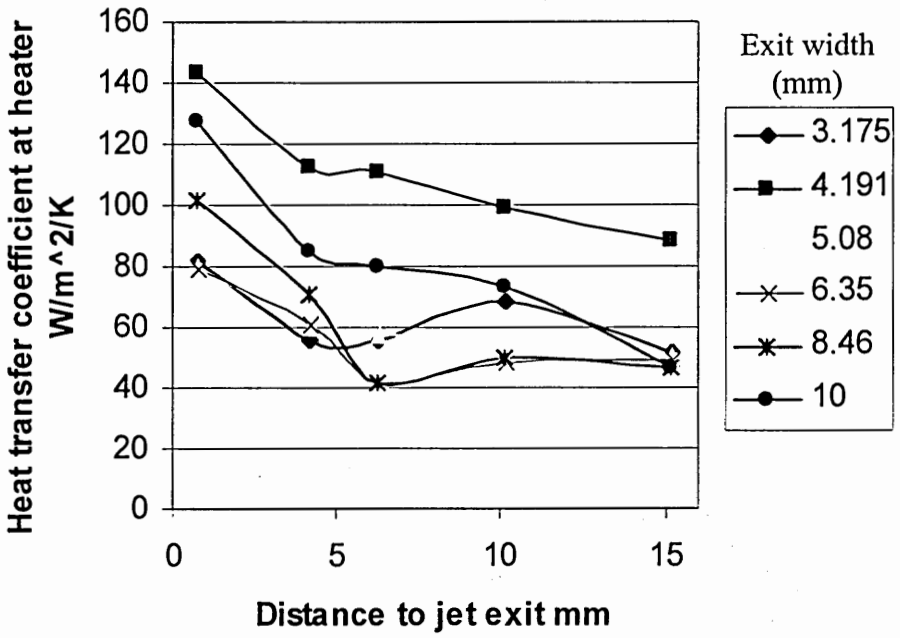

Figure 45. Local heat transfer coefficient

Table 8. Stroke lengths for different fluidic channels

Channel exit	1	2	3	4	5	6
Stroke Length (mm)	13.9	14.7	17.4	24	13.4	22.2

3.6.4 Empirical Correlation Equation

Since the local heat transfer coefficient is known, the local average Nusselt number can be calculated by Equation (14):

$$\overline{Nu} = \frac{\overline{h}_1 D_h}{k} \tag{14}$$

where k is heat conductivity. The calculated Nu is listed in Table 9.

For engineering applications, an empirical correlation of heat transfer (Nu) and fluid mechanics (Re) can be derived by dimensionless group analysis. Normally for forced convection, the Nusselt number (Nu) is the function of the Reynolds number (Re), the Prandlt number (Pr) and some dimension groups (i.e. D_h/L_0, L_x/L_0) as Equation (15):

$$Nu = f(\mathrm{Re}, \mathrm{Pr}, D_h / L_0, L_x / L_0) \tag{15}$$

$$\mathrm{Pr} = \frac{C_p \mu}{k} \tag{16}$$

where C_p is heat capacity and L_x is the distance from the heater to the jet exit. Since the airflow reference temperature is selected to be the constant room temperature, Pr is

constant (0.70) in all the cases and is dropped off from Equation (15). Hence, Nu is simplified as the function of Re, D_h/L_0 and L_x/L_0.

Table 9. Local average Nusselt number calculated from Equation (14)

Fluidic Channel	0.8 mm to Channel Exit	4.23 mm to Channel Exit	6.35 mm to Channel Exit	10.16 mm to Channel Exit	15.24 mm to Channel Exit
1	7.014	4.877	2.847	3.446	3.207
2	5.115	3.849	3.689	3.579	2.792
3	5.268	4.033	2.757	3.223	3.289
4	4.798	3.247	3.257	3.992	2.923
5	8.944	5.941	5.621	5.154	3.252
6	8.884	7.000	6.887	6.175	5.480

In this research, the simplest power law function is applied to curve fit the correlation of Nu and Re, D_h/L_0, L_x/L_0. The data from channel 2-6 are employed to fit the function. The analytical equation is derived as Equation (17):

$$\overline{Nu} = 3.1533\,\mathrm{Re}^{0.19006}\left(\frac{D_h}{L_0}\right)^{0.33214}\left(\frac{L_x}{L_0}\right)^{-0.1501} \tag{17}$$

The overall error of the curve fitting equation is less than 24% when compared with all the data obtained at different channel dimensions. Therefore, the correlation equation (17) is acceptable to demonstrate the relationship between the synthetic jets fluid mechanics and the heat transfer and is applicable to approximate the cooling performance of certain synthetic jets.

For example, this empirical equation is applied to predict the cooling performance of the ACS with fluidic channel 1. Figure 46 compares the model predicted results with the calculated results based on the definition. The deviation is about 16%. This empirical model shows a monotonically decreasing trend of the heat transfer capability as the jets move further away from the exit. It can not reflect the detailed fluctuations at the downstream which is caused by the complicated vortex ring development. The simple power law functions for Reynolds number and the dimension groups (D_h/L_0 and L_x/L_0) are the reason for missing some local disturbance information. A more complicated correlation between Reynolds number and the dimension groups as the work by Petukhov (1970) and Whitaker (1972) may improve the accuracy of the empirical equation.

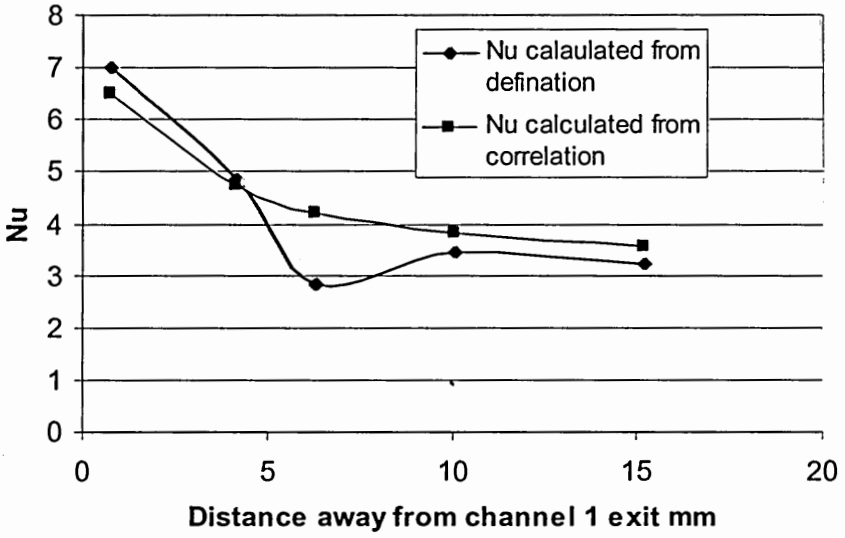

Figure 46. Comparison between the empirical correlation prediction and the calculated results from the definition

A magnitude analysis can be performed on Equation (17) to extract the dimensional impacts on the heat removal. In the following text, the variables in [ ] denote the magnitudes of the variables. Based on the definitions of Nu (Equation (14)) and Re (Equation (10)), $[\overline{Nu}]$ is proportional to the local heat transfer coefficient at the heater $[\overline{h_1}]$ and D_h, $[Re]$ is proportional to u (average velocity over one vibration cycle) and D_h. u can have the same magnitude as u_{im} which is the average velocity over the impingement stroke if u_{in} the average velocity over the intake stroke is small and therefore can be neglected. This assumption is not valid near the jet exit. $[L_0]$ is proportional to u_{im}/f according to its definition (Equation (13)) where f is the AC driving circuit frequency.

Combining the expressions for $[\overline{N_u}]$, $[Re]$ and $[L_0]$ into Equation (17), $[\overline{h_1}]$ can be determined by the following equation:

$$[\overline{h_1}] = \frac{u_{im}^{0.00802} f^{0.18204}}{D_h^{0.4778} L_x^{0.1501}} \tag{18}$$

Based on mass conservation, u_{im} can be simplified as $Q/(t_h w)$. Volumetric flow rate Q can be calculated by Equation (2). D_h is defined in Equation (8). Therefore, Equation (18) can be expressed as

$$[\overline{h_1}] = \{(a^2 + ab + b^2)^{0.00802} D^{0.00802} f^{0.19006}\} \cdot \{\frac{1}{L_x^{0.1501}}\} \cdot \{\frac{(1+\frac{w}{t_h})^{0.4778}}{t_h^{0.49384} (\frac{w}{t_h})^{0.48582}}\} \tag{19}$$

Equation (19) is split into three groups (as indicated by the brackets). The first group includes the parameters related with the diaphragm design (i.e. the diaphragm radius (a), the diaphragm rigid center radius (b), the diaphragm deflection (D) and the excitation frequency (f)). The excitation frequency has a stronger influence on improving the cooling performance than the diaphragm dimensions and deflection. The diaphragm dimensions, frequency and deflection are all related through the Equation (3) which is the

criterion for minimizing the driving force. Therefore, it is necessary to design the diaphragm such that the terms within the first bracket of Equation (19) are maximized and the driving force (Equation (3)) is minimized. At the same time, the diaphragm can not be so large that it occupies too much space in PWB, and hence limits the device density on the board.

The second group shows $\overline{h_1}$ is inversely proportional to the distance between the heater and the jet outlet. Thus, the model indicates that it is better to place the heat generating components close to the jet exit. However, a local minimum of the heat transfer coefficient may exist between the primary optimal cooling location and the secondary optimal cooling location (as shown in Figure 45). This local minimum must be taken into account when placing the heater close to the jet exit.

The third group is related with the fluidic channel dimensions (i.e. the channel thickness (t_h) and width (w)). The channel thickness t_h is normally small due to the low profile design requirement. t_h is assumed to be a constant and factored out in Equation (19). Figure 47 is the plot of function $(1+\frac{w}{t_h})^{0.4778}/(\frac{w}{t_h})^{0.48582}$ versus the ratio of w/t_h. This figure indicates heat transfer becomes weaker as the fluidic channel width increases. However, if the channel width is too small, the jet flow rate would be reduced due to the strong viscous effects. Figure 48 shows the local heat transfer coefficient measurements for different channel widths at 15.24 mm and 0.8 mm away from the jet exit. In these measurements, the channel thickness, the diaphragm dimensions, the driving current magnitude and frequency are the same. Figure 48 indicates a regime for the optimal channel width is between $3t_h$ and $5t_h$ where $\overline{h_1}$ can obtain a high value and the viscous

effects are not dominant. From Figure 48 (a), when the heater is located at 15.24 mm away from the exit, before reaching the optimal channel width, $\overline{h_1}$ increases with the increasing channel width due to the viscous effects. When the channel width exceeds the optimal value, $\overline{h_1}$ decreases as the channel width increases which has the same trend as indicated in Figure 47. However, Figure 48 (b) which is the measurement conducted at the 0.8 mm away from the jet exit reveals a different trend after the optimal channel width $4t_h$ is exceeded. The local heat transfer coefficient increases as the channel width increases. This phenomenon is caused by the intake stroke. In the magnitude analysis, the time average velocity, u is replaced by the impingement average velocity, u_{im}, and the intake average velocity is neglected. The existence of the intake stroke offsets the heat removal caused by the impingement stroke due to a portion of hot air entrainment back into the jet cavity. The offset becomes less important as the channel width increases because of the lower intake stroke velocity. Therefore, as a net cooling result of both impingement stroke and intake stroke, $\overline{h_1}$ increases as the channel width increases after the optimal channel width is exceeded in Figure 48 (b). This intake stroke impacts become weaker as the heater location is further away from the jet exit as indicated in Figure 48 (a). Thus, the data taken at the further downstream have better consistence with the magnitude analysis. Although the magnitude analysis only takes into account the impingement stroke, the resolved optimal channel width shows a global maximum cooling performance in a wide jet coverage range (as shown in Figure 45). Therefore, the conclusions drawn from the magnitude analysis are valid.

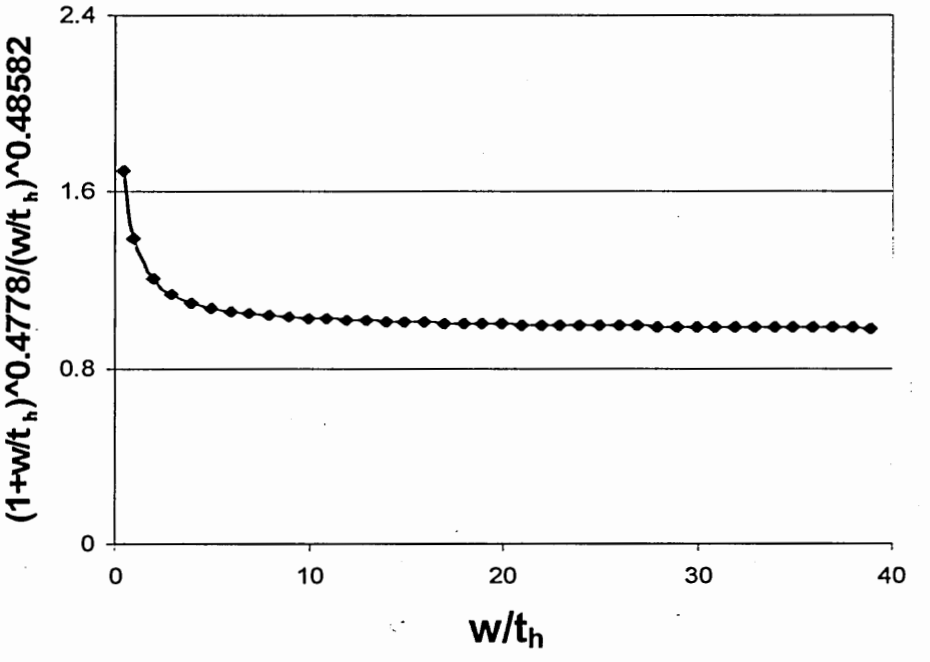

Figure 47. The fluidic channel width impacts on heat transfer

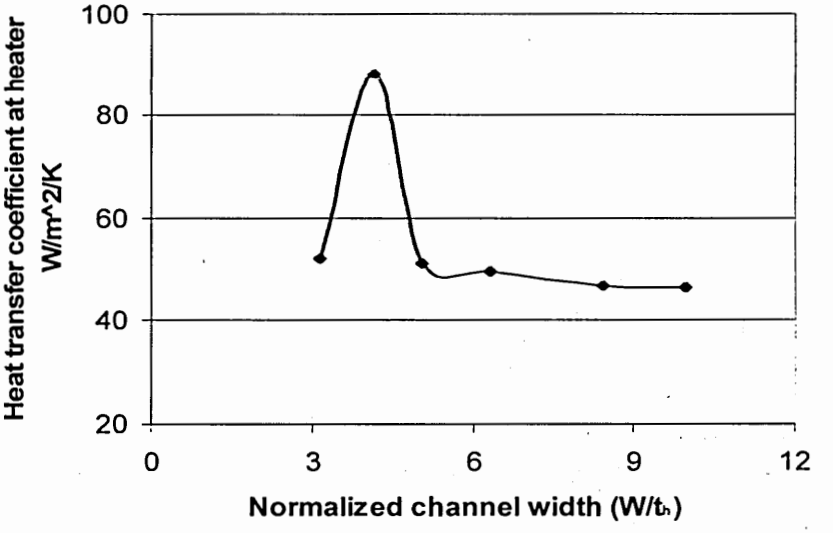

(a)

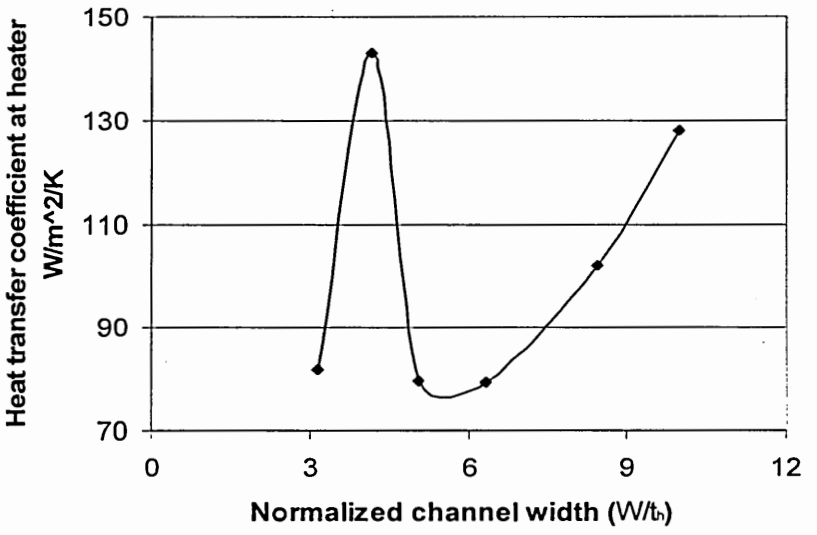

(b)

Figure 48. Heat transfer coefficient vs. normalized channel width (a) measurement at 15.24 mm away from the jet exit (b) measurement at 0.8 mm away from the jet exit

3.7 System Integration

In the prior sections, the detailed design and characterization of the ACS device have been discussed. This section will be a review of the fabrication and assembly of the entire system.

As mentioned before, the main fabrication steps are compatible with the current PWB lamination process. The microfluidic structure is assembled by using multilayer epoxy-glass printed wiring board material. The fabrication sequence is shown in Figure 49(a). The starting material consists of individual epoxy prepreg element layers. These

layers are appropriately patterned using laser cutting. The layers are stacked together and are placed in a hot press for lamination. A temperature of 177 °C is maintained to ensure interlayer bonding. A fabrication sample with multiport distribution is demonstrated in Figure 49(b). The minimum fluidic channel sizes can reach 1000 μm in width and 300 μm in thickness.

In order to realize the goal of ACS development, this fluidic technology must be combined with the synthetic jet driver as described above. Figure 50 presents an ACS device with silicon chip heater at its exit port. The ACS has a cavity with a diameter of 33 mm, a depth of 5 mm, a fluid passage with length of 10 mm, width of 10 mm, thickness of 1 mm, and a rectangular exit port of 10 mm by 1 mm. A coil is mounted on the epoxy prepreg rigid center of the diaphragm. The coil leads are routed out through copper vias drilled in the PWB internal layers.

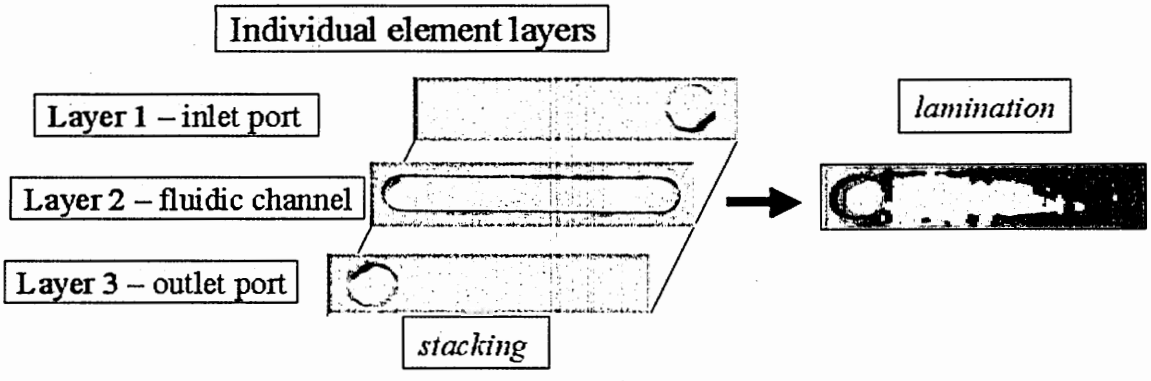

(a)

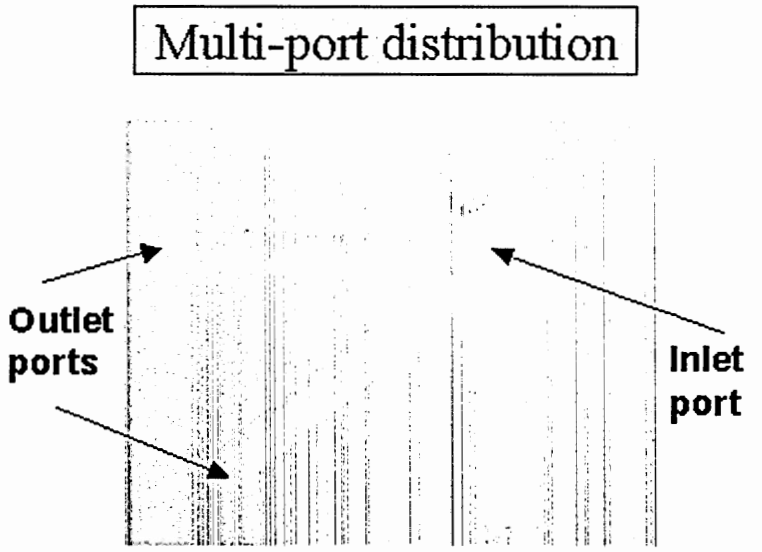

(b)

Figure 49. Lamination process (a) fabrication sequence (b) fabrication samples

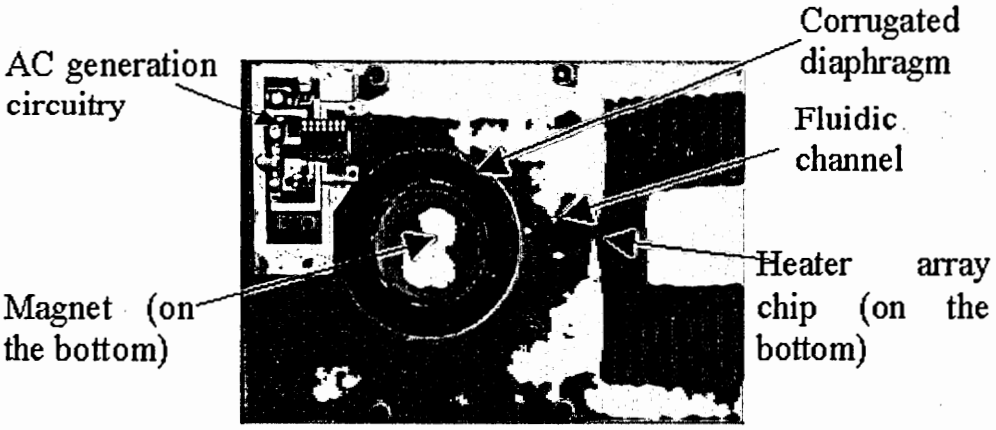

Figure 50. ACS device with silicon heater

An on board AC generation circuitry is designed and integrated with the ACS device. The AC current is generated by an astable multivibrator circuit as shown in Figure 51 (Sedra et al., 1998). This circuit consists of two active components-two op amps (*U1*, *U2*), six passive components-three resistors (*R1*, *R3*, *R4*), two potentiometers (*R*, *R2*) and one capacitor (*C*). *L* is the coil loaded at the output. The first op amp *U1* and *R1*, *R2* form a bistable multivibrator. When *V1o* is positively saturated at *Vsat*+, *V1*+ will keep constant at (*Vsat*+)*R1*/(*R1*+*R2*), the capacitor will be charged through *R*, so *V1*- increases exponentially; when *V1o* is negatively saturated, the capacitor will be discharged so *V1*- decreased exponentially. The second op amp *U2* is the output stage which works as a buffer amplifier to drive the load. Two resistors *R3*, *R4* help to reduce signal distortion when op amps are not so ideal. This circuit has no stable states and thus is named an astable multivibrator. Period *T* of this circuit is defined by Equation (20):

$$T = 2RC\ln[\frac{1+R1/(R1+R2)}{1-R1/(R1+R2)}] \tag{20}$$

This driving circuit is selected because of its simplicity, even though it cannot generate perfect sine wave. By changing *R2* and *R*, a pseudo-sine wave can be generated as shown in Figure 52 and also frequency and magnitude of the output voltage are controllable.

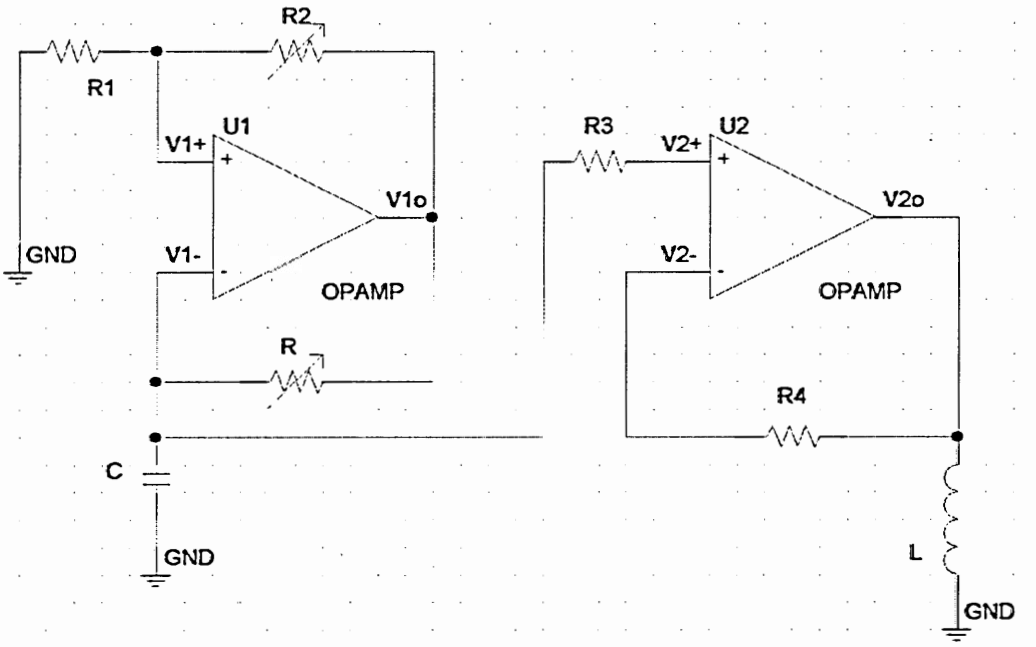

Figure 51. Astable multivibrator driving circuit schematic

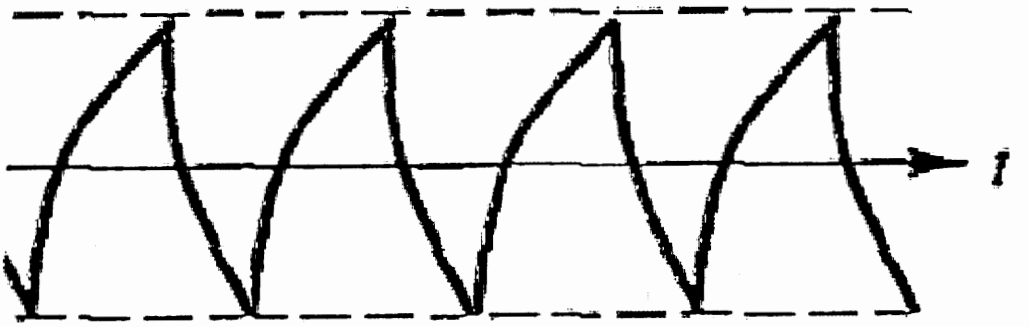

Figure 52. Waveform generated from the astable multivibrator circuit

The astable multivibrator driving circuit consists of active and passive components. Capacitors, resistors and potentiometers are individual packaged chips. The two op amps are in a commercialized National Semiconductor chipset-CLC5623. This is a triple, high output chip fabricated by an advanced complementary bipolar process. Its connection diagram is shown in Figure 53. Only two of them are connected in the coil driving circuit. The highest output current can reach 130 mA.

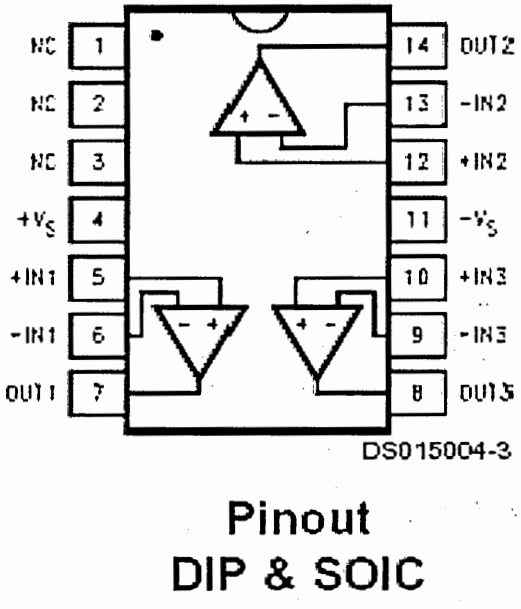

Figure 53. Connection diagram of National Semiconductor CLC5623 chip

All the components are surface mounted on the top surface of PWB with a copper interconnect pattern. Here the surface mounting is a simplified reflow process which is

performed in a Paragon 98 oven (BTU International). First, a solder mask is made from a mylar sheet by laser cutting. Only the windows for the solder bumps are opened on the sheet. Second, the solder mask is aligned with the copper trace pattern on the PWB substrate and the solder paste is screen printed on the board. Solder paste NC-SMQ 92 (Indium Corporation of America) is used which consists of 63% tin and 37% lead. Third, all of the components are placed on the board and all the pins are in good contact with the solder paste. Then, the board is laid on the conveyor of the reflow oven. As the board passes through the oven, the solder paste is heated to melting and then cooled to solidification. There are seven heated zones with the total length of 249 cm and only one cooling zone with the length of 71 cm in the oven. Temperatures above and beneath the board are controlled by KIC thermal profiling system. The temperature profile along the oven is listed in Table 10. The conveyor speed is controlled at 0.0055 m/s (13 inches per minute). At the end of the cooling zone, the integrated ACS is completed from the last fabrication step and ready for test. Hence, if a ±5 V DC supply is fabricated on the board, the diaphragm could be driven to generate synthetic jets. This fully integrated ACS is also tested by cooling performance. Having the same coil driving current, frequency and the same fluidic channel design, this ACS system demonstrates a similar heat removal of 3.3 W/cm^2 even though the AC driving current waveform is slightly different from the perfect sine wave. Therefore, the ACS fluidic device is functional and is fully integrated with the printed wiring board.

Table 10. Temperature profile along the reflow oven

Temperature (°C)	Heated Zone							Cooling Zone
	1	2	3	4	5	6	7	1
Top	100	150	150	170	200	250	250	25
Bottom	100	150	150	170	200	250	250	25

3.8 Summary

In this chapter, the ACS design, fabrication and test are discussed in detail. Two prototypes of ACS devices are demonstrated. The vertical ACS has the advantage of the air entrainment. The tangential ACS has a more compact structure. In practice, the tangential orientation is preferred.

The corrugated polymeric diaphragm ensures a quiet, low power and efficient actuator. The diaphragm is fabricated using a fluoroelastomer. The elastomer pellets are molded into the optimal designed shapes. The diaphragms are excited by electromagnetic drivers. A simplified pseudo-sine wave AC generation circuit is integrated on the ACS substrate as well. The circuit components are surface mounted on board by a reflow process.

Fluid channel optimization is investigated by a testbed. The optimal dimension and optimal cooling locations are identified. A correlation equation is derived to represent the relationship between the fluid mechanics and heat transfer. It can guide the future synthetic jet design and predict the fluid or cooling behaviors.

Chapter 4

CFD SIMULATIONS

In this chapter, a computational fluid dynamics (CFD) software package, Fluent, is employed to solve the synthetic jet fluid mechanics and heat transfer problems. A fundamental understanding of the ACS fluid mechanics and cooling mechanism is achieved, and a predictive model is accomplished by the numerical approach.

CFD is the study of fluids in flow by numerical simulation. The basic idea is to use appropriate algorithms to find solutions to the equations describing the fluid motions. More complicated cases which may combine heat transfer or mass transfers with certain fluid motions can also be treated.

In this research, CFD simulations focus on engineering analysis, where flow characteristics need to be predicted in equipment design phase. The goal is not to provide data for analyzing the flow dynamics itself, but rather to predict certain of the flow characteristics or, more precisely, the values of physical parameters that depend on the flow. The modeling can reduce the cost and time needed to develop a prototype. The quality of the prediction improves with the richness of the physical model.

4.1 Synthetic Jet Simulations

Synthetic jets are zero net mass flux jets. Fluid ejected by the pulsing jets rolls upward into vortices that propagate due to their mutually induced velocity and the initial

momentum given by the pulse. To capture the unique flow features of the synthetic jets, the pulsating boundary condition must be set.

The flexible diaphragm is a pulsating boundary. Rizzetta et al. (1999) simulated the membrane motion by varying the position of appropriate boundary points. Lee et al. (2000) used a virtual surface to define the moving wall. This approach imposes a localized body force along desired points in the computational mesh to bring the fluid there to a specified velocity so that the force has the same effect as a solid boundary. The desired velocity is incorporated in an iterative feedback loop to determine the appropriate force. This technique allows for fairly complex geometries and/or moving boundaries to be incorporated in a regular domain without the usual complexities of mapping. Another simplified alternative is to apply an analytical velocity profile on the boundary region. Kral et al. (1997) directly applied a suction/blowing type velocity boundary on the region corresponding to the jet orifice. The perturbation on the flow field is introduced through the wall normal component of velocity as shown in Equation (21):

$$\overline{u_n}(\xi = 0, \eta, t) = U_0 f(\eta) \sin(\omega t) \tag{21}$$

where U_0 is the magnitude of the velocity, ξ denotes the streamwise direction, η denotes the cross-stream direction, and $\overline{u_n}$ is the streamwise component of velocity. $f(\eta)$ represents different spatial variations over the orifice. The validity of this approach has been confirmed by the moving wall technique. Therefore, this simplified boundary

condition can dramatically reduce the computational time compared to the conventional boundary condition of a solid moving surface.

The second challenge of the synthetic jet simulations is to combine fluid mechanics with heat transfer. In this research, synthetic jets are employed in thermal management. Thus it is necessary to make clear the impact of fluid physics on heat transfer. Chiriac et al. (2001) simulated the heat removal of the unsteady impinging jets. A uniform heat flux boundary is added to the simulation model. Compared to the steady impinging jets, the unsteady jet becomes distorted and buckles beyond a critical Reynolds number of 600, which leads to a sweeping motion of its tip. As a result of the combined buckling/sweeping jet motion, the cooled area is significantly enhanced. The impinging jet is similar to the vertical ACS device. Here the tangential ACS jet is also a research topic of great interest.

In some prior simulation work (Kral et al., 1997, and Lee et al., 2000), a two-dimensional (2-D) simulation model was used. 2-D model simplifies the physical model and reduces the computational time. Other work (Rizzetta et al., 1999) employed three-dimensional (3-D) model, and the results indicated that the external flow breakdown into a turbulent jet observed in experiments is a result of 3-D instabilities, which also explain why no such phenomena are observed in any strictly 2-D simulations. In this study, a 3-D model is preferred because the fluidic channels added to the cavity lead to a non axis symmetric structure. Therefore, a 3-D model is more suitable than a 2-D model.

The near flow field of the synthetic jets is dominated by the formation of vortex rings. Further away from the jet outlet, the vortex cores vanish due to turbulent diffusion. Hence, selection of an appropriate turbulence model is critical.

Kral et al. (1997) solved the incompressible, unsteady 2-D Reynolds Averaged Navier-Stokes (RANS) equations with the Spalart-Allmaras (SA) turbulence model. The Reynolds-averaged Navier-Stokes (RANS) equations represent transport equations for the mean flow quantities only, with all the scales of the turbulence being modeled. The approach of permitting a solution for the mean flow variables greatly reduces the computational effort. If the mean flow is steady, the governing equations will not contain time derivatives, and a steady-state solution can be obtained economically. A computational advantage is seen even in transient situations, since the time step will be determined by the global unsteadiness in the mean flow rather than by the turbulence. The Spalart-Allmaras model is one of the models implementing the RANS approach. It is a relatively simple one-equation model that solves a modeled transport equation for the kinematic eddy (turbulent) viscosity. This embodies a relatively new class of one-equation model in which it is not necessary to calculate a length scale related to the local shear layer thickness. The Spalart-Allmaras model is designed specifically for aerospace applications involving wall-bounded flows and has been shown to give good results for boundary layers subjected to adverse pressure gradients. It is also gaining popularity for turbomachinery applications. In its original form, the Spalart-Allmaras model is effectively a low-Reynolds-number model, requiring the viscous-affected region of the boundary layer to be properly resolved. It may be the best choice for relatively crude simulations on coarse meshes where accurate turbulent flow computations are not critical.

In addition, this model is less sensitive to numerical error when non-layered meshes are used near walls. On a cautionary note, however, the Spalart-Allmaras model is still relatively new, and no claim is made regarding its suitability to all types of complex engineering flows. For instance, it cannot be relied on to predict the decay of homogeneous, isotropic turbulence. Furthermore, one-equation models are often criticized for their inability to rapidly accommodate changes in length scale, such as might be necessary when the flow changes abruptly from a wall-bounded to a free shear flow.

Rizzetta et al. (1999) and Lee et al. (2000) used a direct numerical simulation (DNS) approach to solve the unsteady, compressible Navier-Stokes equations. Direct numerical simulations seek the solution to the Navier-Stokes equations by directly resolving the whole spectrum of turbulent scales without any modeling. DNS is not, however, feasible for practical engineering problems. It is restricted to simple and low Reynolds number simulations. To understand the large computational cost of DNS, consider that the ratio of the large (energy-containing) scales to the small (energy-dissipating) scales is proportional to $Re_t^{3/4}$, where Re_t is the turbulent Reynolds number. Therefore, to resolve all the scales, the mesh size in three dimensions will be proportional to $Re_t^{9/4}$. Simple arithmetic shows that, for high Reynolds numbers, the mesh sizes required for DNS are prohibitive. The ratio of characteristic times also varies as the magnitude of $Re_t^{3/4}$. Therefore, in order to calculate the evolution of the solution in a volume for a duration equal to the characteristic time of the most energetic scale, the Navier-Stokes equations have to be solved for Re_t^3 times. This type of computation for large Reynolds numbers

requires computer resources very much greater than currently available supercomputer capabilities, and is therefore not practicable.

In this study, the large eddy simulation (LES) approach is proposed to simulate the synthetic jet flow. Large eddy simulation is situated somewhere between DNS and the RANS approach (e.g. SA model). Basically, in LES, large eddies are resolved directly, while small eddies are modeled. Solving only for the large eddies and modeling the smaller scales results in mesh resolution requirements that are much less restrictive than with DNS. Furthermore, the time step sizes will be proportional to the eddy-turnover time, which is much less restrictive than with DNS. In contrast to RANS approach, LES does not have a large number of parameters to parameterize the turbulent effects. Moreover, in the LES approach, approximation errors inherent in the smaller scale models are of less importance than errors in the RANS models. In practical terms, however, extremely fine meshes are still required for the LES approach. It is only due to the explosive increases in computer hardware performance coupled with the availability of parallel processing that LES can even be considered as a possibility for engineering calculations. In the next section, the LES approach will be introduced in detail.

4.2 Large Eddy Simulation

Large eddy simulation is a promising approach for simulation of complex, high Reynolds number turbulent flows. In the LES approach, the turbulent scales are decomposed into large resolved scales (which are likely to be anisotropic) and subgrid unresolved scales (which may or may not be isotropic) by applying a spatial filter to the Navier-Stokes equations. The filtered Navier-Stokes equations represent the transport of

the low frequency modes in the resolved scale velocity field and include the contribution of the unresolved high frequency small scales through subgrid scale stress (SGS). This is illustrated in Figure 54. The impact of the subgrid scales on the resolved scales is parameterized by the so-called subgrid scale model. Since only the large energy containing scales have to be resolved in LES, in principle, turbulent flows can be simulated at a higher Reynolds number and/or on a coarser grid resolution when compared to the DNS approach. This is a main virtue of the LES approach.

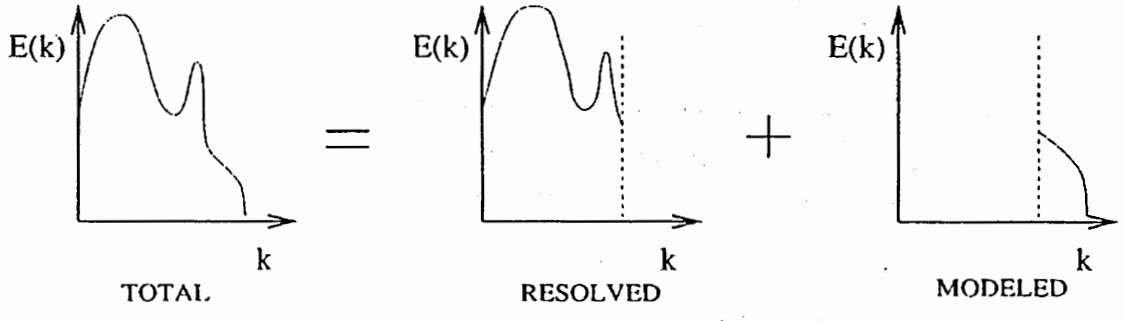

Figure 54. Decomposition of the energy spectrum in the solution associated with LES

Over thirty years have passed since the first large eddy simulation results by Deardorff (1970) were published. Deardorff (1970) simulated the turbulent flow in a channel at infinite Reynolds number and parameterized the effect of the subgrid scales on the large scales by using the algebraic eddy viscosity model introduced by Smagorinsky (1963) and further developed by Lilly (1966). In Deardorff's simulations, approximated

boundary conditions were used to ensure that the logarithmic law-of –the-wall is obeyed. The dynamics of the wall layer in which most of the turbulence is produced were not computed. The mean velocity and Reynolds stress profiles were within 30-50% of the experimental values. In the wake of the interest raised by Deardorff's work, considerable effort has been spent in developing theoretical foundations for large eddy simulations. Moin and Kim (1982) performed simulations of turbulent channel flows in which the wall layer is resolved. To force the SGS stresses to vanish at the solid boundary and to account for the decreased size of the small scale structures due to the presence of the wall, the length scale in the Smagorinsky model has to be modified. Moin and Kim (1982) also divided the SGS stresses into a locally isotropic part and an anisotropic part. The mean velocity, Reynolds stresses, turbulent intensities and higher order statistics predicted by Moin and Kim (1982) agreed well with experimental results. Horiuti (1987) suggested using the conservative skew symmetric scheme by Arakawa (1966). His results compared better with experiments than did those of Moin and Kim (1982). Yoshizawa (1986) used the direct interaction approximation by Kraichnan (1964) to derive a Smagorinsky-type SGS model valid in mildly compressible flows.

In LES approach, there are two key characteristics. One is the filter function; the other is the SGS model. To apply the LES approach, first the flow variables are decomposed into large scale components (denoted by an overbar) and small subgrid scale components by employing a filtering operation:

$$\bar{\phi}(x) = \int_{Dom} \phi(x')G(x,x')dx' \tag{22}$$

where *Dom* is the fluid domain, and *G* is the filter function which determines the scale of the resolved eddies. Commonly used filter functions are the Gaussian, the Fourier cut-off, and the top hat in physical space (Leonard, 1974). Applying the filtering operation, the incompressible Navier-Stokes equations for the evolution of the large scale motions are obtained. The resulting governing equations are:

$$\frac{\partial \rho}{\partial t} + \frac{\partial \rho \bar{u}_i}{\partial x_i} = 0 \tag{23}$$

$$\frac{\partial}{\partial t}(\rho \bar{u}_i) + \frac{\partial}{\partial x_j}(\rho \bar{u}_i \bar{u}_j) = \frac{\partial}{\partial x_j}(\mu \frac{\partial \bar{u}_i}{\partial x_j}) - \frac{\partial \bar{p}}{\partial x_i} - \frac{\partial \tau_{ij}}{\partial x_j} \tag{24}$$

where i (=1,2,3) indicates the spatial dimension, and $\bar{u}_i(x_i,t)$ is the resolved velocity field. τ_{ij} is the subgrid scale stress defined by:

$$\tau_{ij} = \overline{\rho u_i u_j} - \rho \bar{u}_i \bar{u}_j \tag{25}$$

As suggested by Leonard (1974), using Equation (26), the SGS stresses can be decomposed into three parts as shown in Equation (27-29).

$$u_i = \bar{u}_i + u'_i \tag{26}$$

$$L_{ij}^{grid} = \rho(\overline{\bar{u}_i \bar{u}_j} - \bar{u}_i \bar{u}_j) \tag{27}$$

$$C_{ij} = \rho(\overline{\bar{u}_i u'_j} + \overline{u'_i \bar{u}_j}) \tag{28}$$

$$R_{ij}^{sgs} = \rho\overline{u'_i u'_j} \tag{29}$$

where L_{ij}^{grid} is the grid scale stresses, C_{ij} is the cross stresses, R_{ij}^{sgs} is the SGS Reynolds stresses. However, as noted by many researchers (e.g. Germano, 1992), if the terms are modeled separately, the Galilean invariance property may be lost. Therefore, it is better to model τ_{ij} as a whole.

The subgrid scale stresses resulting from the filtering operation are unknown and require modeling. The majority of the subgrid scale models in use today are eddy viscosity models. The models assume proportionality between the anisotropic part of the SGS stress tensor $\tau_{ij} - \frac{1}{3}\delta_{ij}\tau_{kk}$ and the resolved scale strain rate tensor $\bar{S}_{ij}$ as Equation (30):

$$\tau_{ij} - \frac{1}{3}\delta_{ij}\tau_{kk} = -2\mu_t \bar{S}_{ij} \tag{30}$$

where μ_t is the subgrid scale turbulent viscosity, and $\bar{S}_{ij}$ is defined by:

$$\bar{S}_{ij} = \frac{1}{2}\left(\frac{\partial \bar{u}_i}{\partial x_j} + \frac{\partial \bar{u}_j}{\partial x_i}\right) \tag{31}$$

The most basic of subgrid scale models is proposed by Smagorinsky (1963) and further developed by Lilly (1966). In the Smagorinsky-Lilly model, the eddy viscosity is simulated by:

$$\mu_t = \rho L_s^2 \left|\bar{S}\right| \tag{32}$$

$$\bar{S} = \sqrt{2\bar{S}_{ij}\bar{S}_{ij}} \tag{33}$$

where L_s is the mixing length of subgrid scales. Most of the other SGS models are the Smagorinsky type variations.

In this study, a commercial CFD software package, Fluent, is used to perform the simulations. In Fluent, a finite volume method is applied to solve the differential equations. The finite volume discretization implicitly provides the filtering operation:

$$\bar{\phi}(x) = \frac{1}{V}\int_{V} \phi(x')dx', \qquad x' \in V \tag{34}$$

where V is the volume of a computational cell. The filter function, $G(x, x')$ implied here is then:

$$G(x,x') = \begin{cases} 1/V, & x' \in V \\ 0, & otherwise \end{cases} \tag{35}$$

As to the Smagorinsky-Lilly model, in Fluent, the mixing length for subgrid scales L_s is computed using Equation (36):

$$L_s = \min(\kappa d, C_s V^{1/3}) \tag{36}$$

where $\kappa = 0.42$, d is the distance to the closest wall, C_s is the Smagorinsky constant, and V is the volume of the computational cell. Lilly derives a value of 0.23 for C_s from the homogeneous isotropic turbulence in the inertial subrange. However, this value is found to cause excessive damping of large-scale fluctuations in the presence of mean shear or in transitional flows. C_s=*0.1* has been found to yield the best results for a wide range of flows and is the default value in Fluent. Based on the filter function and the Smagorinsky-Lilly SGS model, LES approach in Fluent can be applied to simulate complex fluid flows.

4.3 Synthetic Jet Fluid Mechanics Simulations

The Fluent simulations are divided into two steps. The first step is focused on the fluid mechanics only. The boundary conditions are investigated, and the modeling results are compared with experimental data. The second step further explores the application of synthetic jets in thermal management which is a simulation case of fluid mechanics combined with heat transfer. The thermal boundary condition is applied and the energy governing equations are added. This section will only discuss the fluid mechanics simulations.

4.3.1 Vertical ACS Jet Simulations

There are two governing equations for fluid mechanics simulations which have been shown above as Equation (23) and (24). Equation (23) is the law of conservation of mass. Equation (24) is the Navier-Stokes equations which represent the momentum conservation.

There are two basic steps involved in a CFD simulation: (1) drawing and gridding the physical model; (2) applying boundary conditions and solving the problem. Fluent Inc. offers another software package, GAMBIT, to accomplish the model drawing and meshing. Figure 55 shows the symmetric cross section view of the 3-D meshed model for the vertical ACS device with the outlet size of 4.09 mm in diameter. The dimensions are exactly the same as the real device. Above the jet outlet, there is an added virtual hemisphere dome. This dome does not exist in a real case. However, it is added to investigate the flow field at the downstream of the jet outlet. The flow pattern developed in the dome is the focus of the CFD simulations. To eliminate the edge effect of the dome on the jet behavior, the dome radius is selected as 20 times larger than the diameter of the jet outlet. The entire physical model is meshed into triangular finite volume elements. The total number of element nodes is approximately 90,000. The model is not uniformly meshed. The center region close to the jet outlet is gridded much finer than the edge of the dome which facilitates the higher accuracy at the near jet exit region which is of great interest. Two boundary surfaces are marked by GAMBIT. One is the inlet boundary surface where the flexible vibration diaphragm is located. The other one is the outlet boundary surface which is the outside surface of the hemisphere dome.

After the GAMBIT preprocess, the meshed model is imported into Fluent which is the CFD solver. At this step, the boundary conditions are defined, the suitable simulation models are selected, and finally the problem is solved. With the limitation of Fluent version 5.5, there is no moving wall boundary condition which can be applied at the vibration diaphragm. Kral's method (Kral et al., 1997), a velocity boundary condition, is used here instead. As shown in Equation (21), $f(\eta) = 1$ is set. The magnitude of the

velocity U_0 is determined from the laser vibrometer experimental result. With the measurement of the diaphragm deflection, the volumetric flow rate in a half vibration cycle (i.e. the impingement cycle) can be calculated by Equation (2). Then linear velocity magnitude U_0 at the diaphragm can be determined by the volumetric flow rate with respect to the diaphragm surface area. From Equation (21), the velocity boundary condition varies not only with space, but also with time. Therefore, an unsteady simulation is applied in the study. In one cycle, the averaged velocity is zero to ensure zero net mass flux at that surface which meets the inherent nature of a synthetic jet. The second boundary condition is the outlet boundary condition which is set as the atmospheric pressure at the dome of the hemisphere.

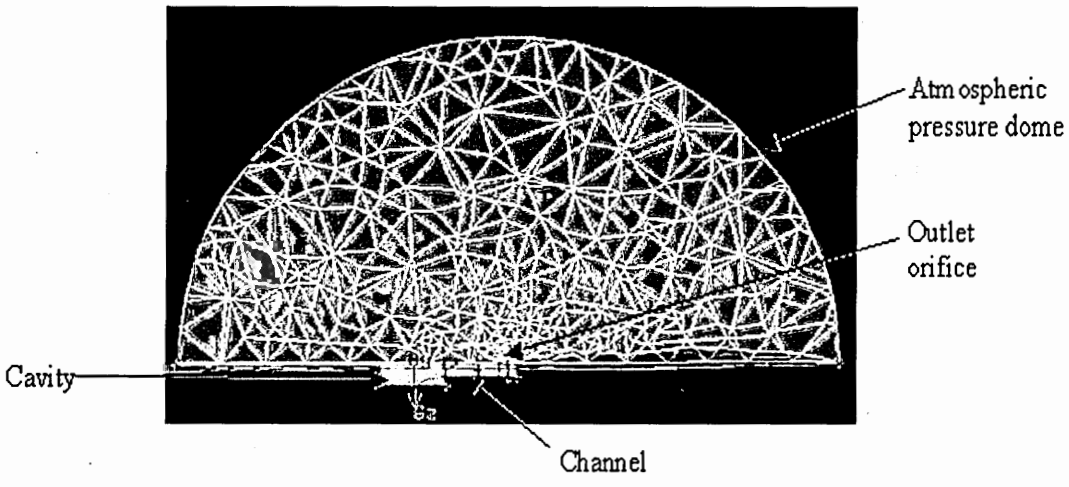

Figure 55. Cross section view of the mashed model for vertical ACS

Large eddy simulation is selected as the turbulence model to perform the simulations. First, grid and time step independence investigation are conducted. This investigation ensures to capture most accurately the flow physics within a reasonable computational time. Three different grid nodes: 50,000, 90,000 and 150,000 are tested. With 90,000 grid nodes, the simulation demonstrates a satisfactory result (i.e. the velocity magnitude are independent of the grid density). Thus 90,000 nodes is refined enough to capture the fluid physics, yet not too detailed to increase unnecessarily the computational volume and CPU time as the 150,000 nodes. Since this an unsteady simulation, the time step independence study is necessary to determine how many time steps should be applied in one cycle. Three different time steps: 12, 16, 24 are tested. 16-time-step shows a satisfactory result which is independent of the time steps selection. Therefore, 90,000 grid nodes and 16 time steps in a cycle are adequate for the unsteady simulation. With a personal computer (PC) of CPU frequency 1.5 GHz and a memory of 512 MB, it takes about 10 minutes to complete one time step simulation. After one cycle, namely, 16 time steps, the simulation starts to reach convergent cycling results.

The simulations (i.e. velocity profile and magnitude) are compared with the experimental results. First, the downstream synthetic jets development is compared with the PIV image as shown in Figure 56. The images presented here are on the symmetrical cross section cut plane. The velocity vector direction is indicated by the arrow direction. The velocity magnitude is represented by the arrow length in PIV result, while it is indicated by different colors in Fluent simulations. Figure 56(a) illustrates the full impingement stroke. The vortex rings are formed around the jet core. Figure 56(b) demonstrates the full intake stroke. The prior jet vortices lose coherence and propagate

to the far jet outlet region. Air surrounded the exit outlet is entrained into the cavity. The Fluent simulations are able to represent the main flow features of the synthetic jet.

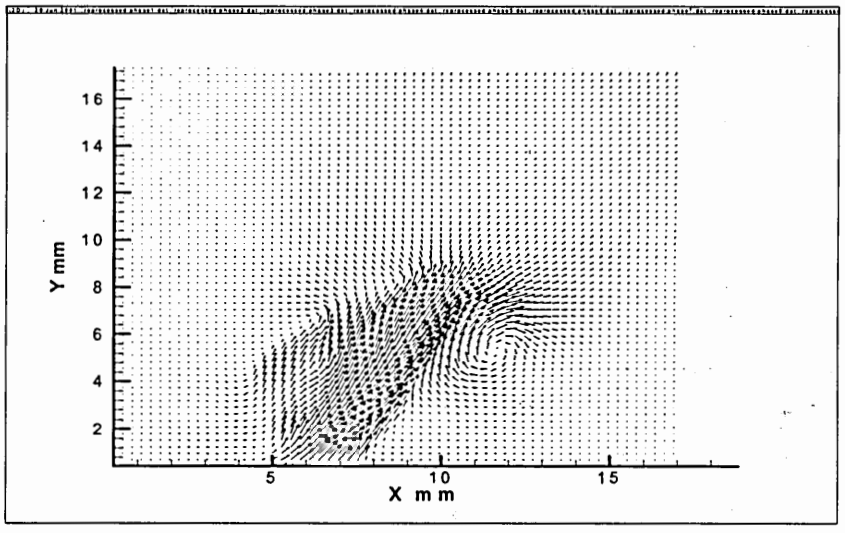

(a)

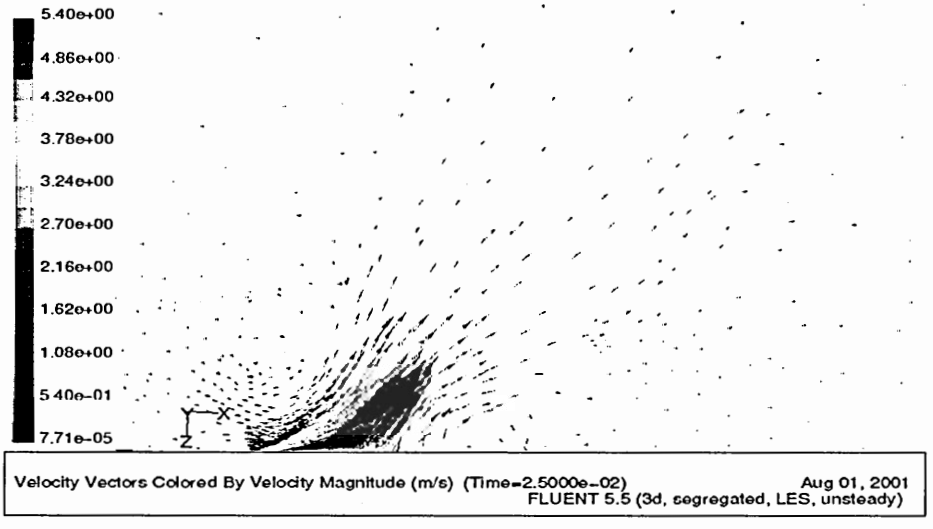

(b)

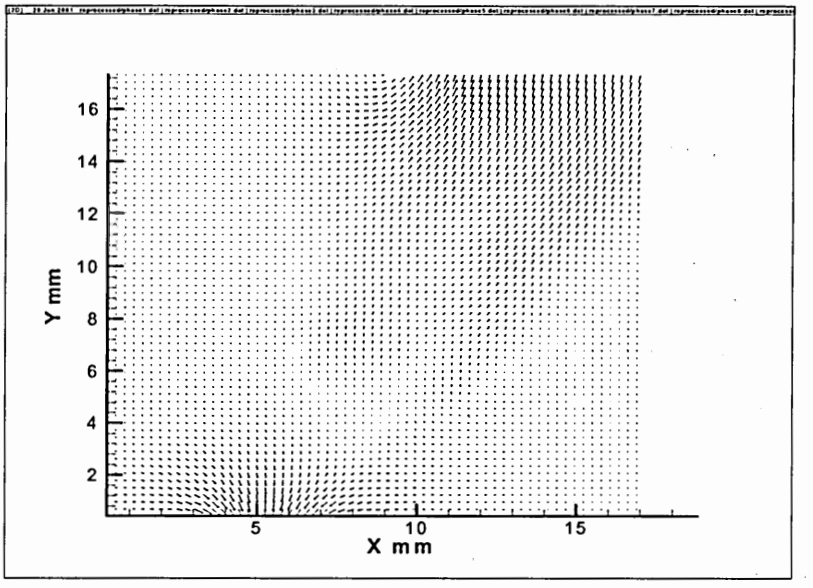

(c)

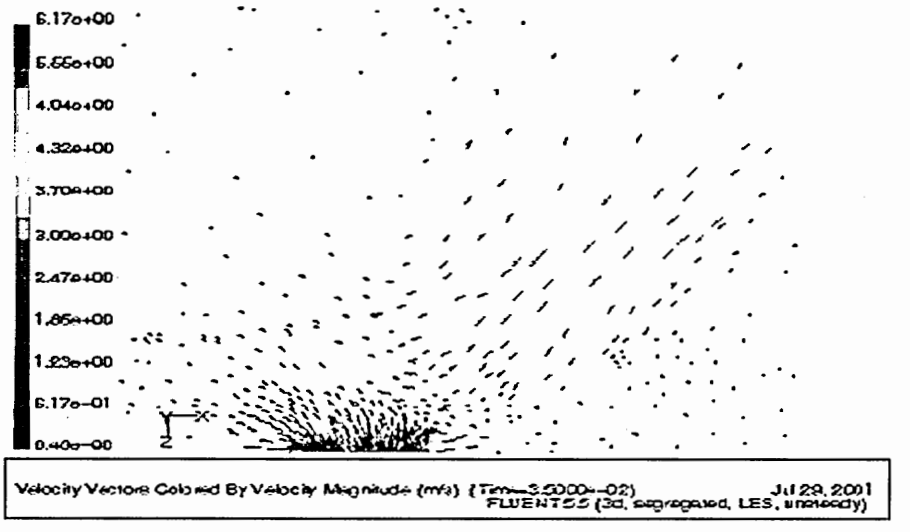

(d)

Figure 56. Vertical ACS flow field comparison between PIV images and Fluent simulation at position above the outlet (orifice diameter=4.09 mm) (a) PIV at full impingement stroke (b) CFD simulation at full impingement stroke (c) PIV at full intake stroke (d) CFD simulation at full intake stroke

To further validate the fluid mechanics simulations, it is also compared with the hot-wire result. The pinpoint comparison position is picked at the 0.8 mm away from the jet outlet. As shown in Figure 57, the centerline velocity magnitudes closely reflect the real experimental data. Based on the flow field and pinpoint velocity magnitude comparisons, the large eddy simulation model is sufficiently accurate to reflect the fluid mechanics features of the synthetic jets.

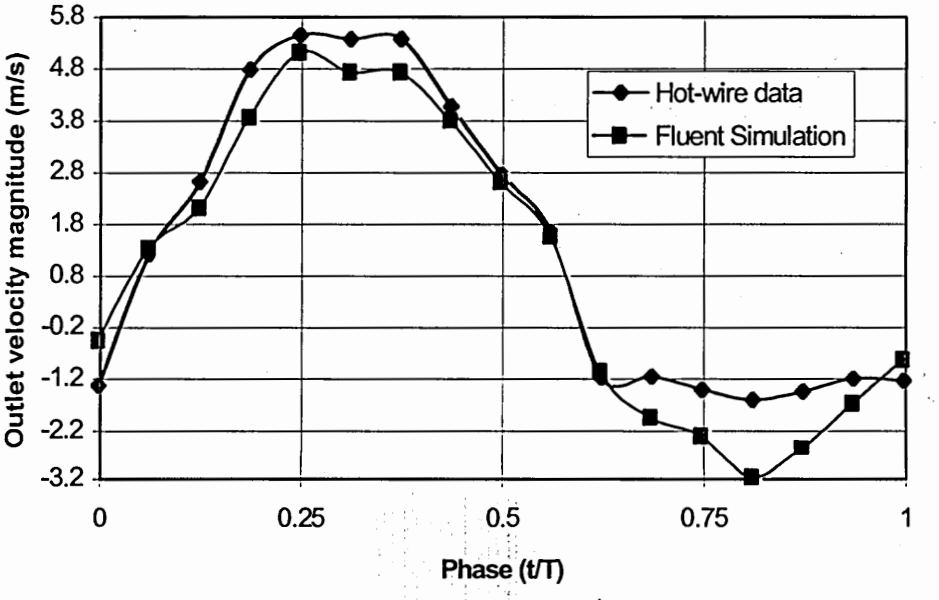

Figure 57. Vertical ACS phase-averaged maximum velocity magnitude in one cycle at the position of 0.8 mm above the outlet, orifice diameter=4.09 mm, frequency=50 Hz, and coil driving current 180 mA

4.3.2 Tangential ACS Jet Simulations

Fluent CFD simulations are performed on the tangential ACS devices as well. Figure 58 is the meshed model for the tangential ACS. The physical model has the same dimensions as the real device with a rectangular exit of 10 mm by 1 mm. A major difference between the models for the tangential device and the vertical device is the virtually added vole. Instead of a hemisphere dome, a quarter of a sphere is attached at the jet outlet to explore the jet development at the downstream. Figure 58 shows the model with 90,000 meshed nodes.

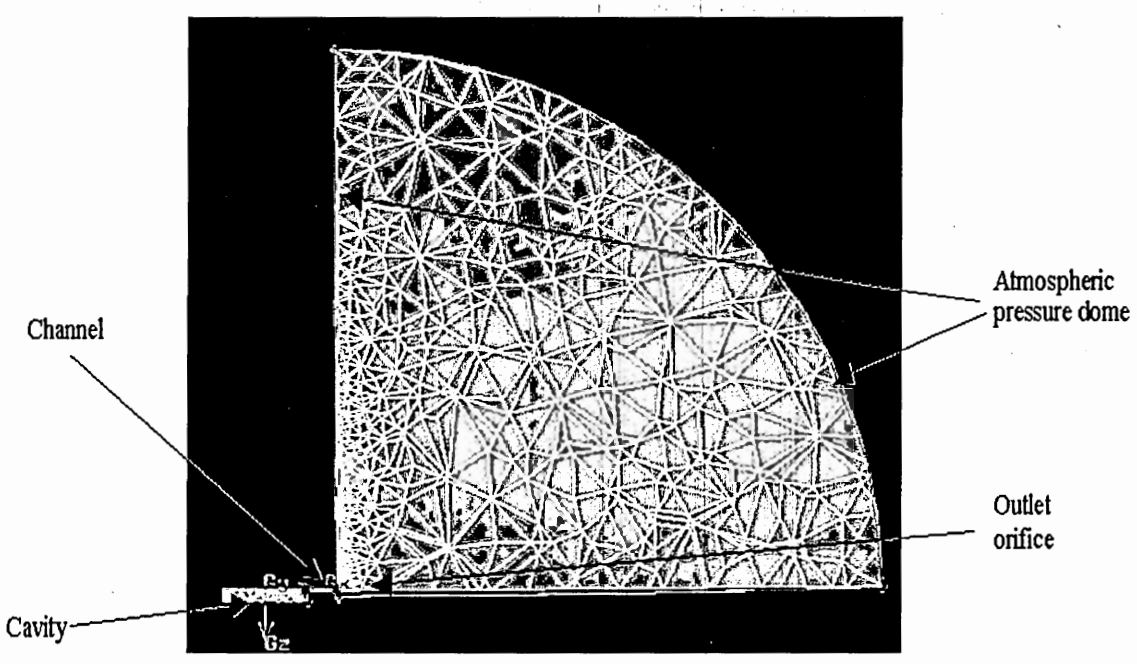

Figure 58. Cross section view of the meshed model for tangential ACS device

The tangential ACS model is meshed non-uniformly. The region near the jet outlet has much denser meshing than the region far from the jet outlet. The grid and time step independence study are conducted on the model. Grid and time step independent simulation results are obtained with 90,000 meshed nodes and 16 times steps in one cycle. The simulations are compared with PIV and hot-wire date. Figure 59 presents the simulated jet flow field pattern. Figure 59(a) is the full impingement stroke with a vortex generated at the exit. Figure 59(b) is the full intake stroke with the surrounding air drawn back into the cavity. Figure 60 compares the centerline velocity magnitude at the 0.8 mm away from the exit. The simulations show consistent results with the hot-wire measurement. Therefore, the tangential ACS simulations are also verified. Hence, the two simulation cases validates that the velocity boundary condition, and the LES turbulence model are suited for synthetic jet fluid mechanics simulations.

4.4 Fluid Mechanics Coupled With Heat Transfer

The energy boundary condition is added to the CFD model to solve the fluid mechanics coupled with heat transfer problem. With the energy consideration, temperature varies with space and time. Temperature variations also affect the fluid properties. Modifications on the model setup, boundary conditions and problem solving method are necessary. This section discusses the solution of this complicated simulation case.

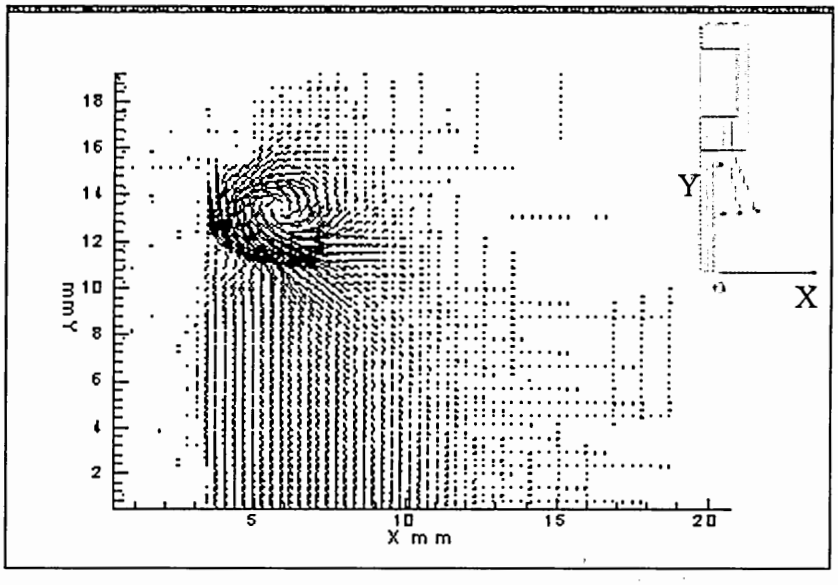
18
16
14
12
10
8
6
4
2
Y mm
5
10
15
20
X m m
Y
X

(a)

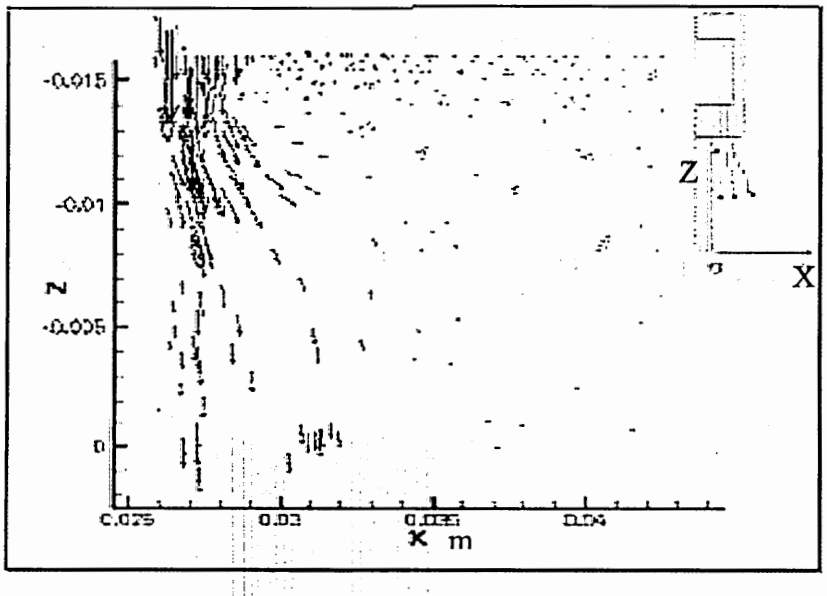
-0.015
-0.01
-0.005
0
Z
0.025
0.03
0.035
0.04
X m
Z
X

(b)

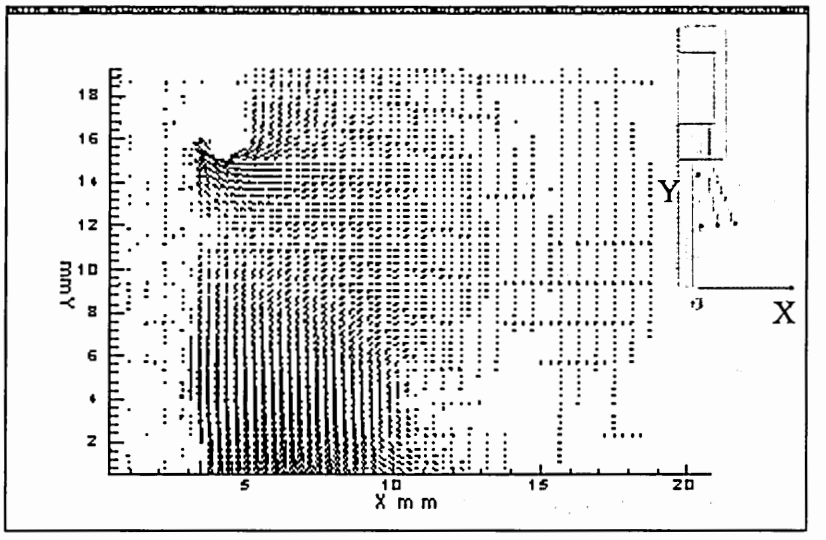

(c)

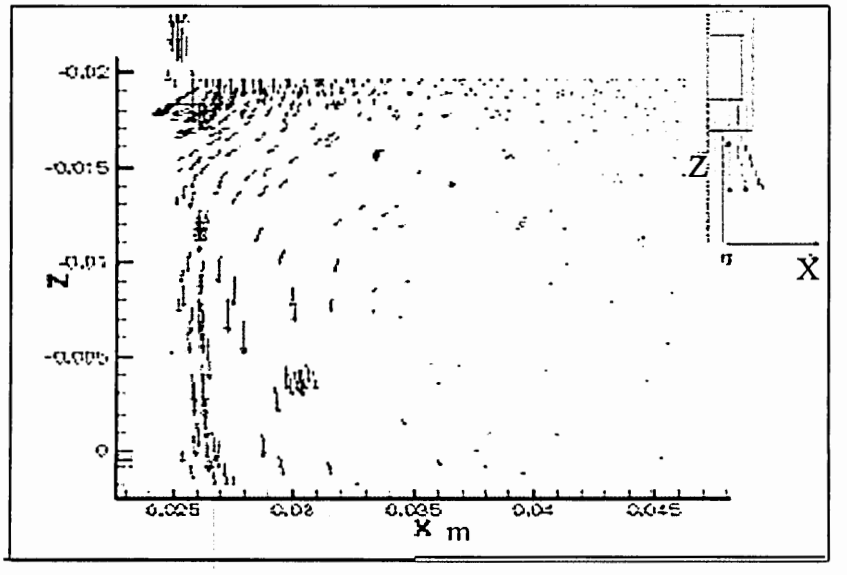

(d)

Figure 59. Tangential ACS flow field comparison between PIV images and Fluent simulation at the downstream of the jet outlet (a) PIV at full impingement stroke (b) CFD simulation at the full impingement stroke (c) PIV at full intake stroke (d) CFD simulation at full intake stroke

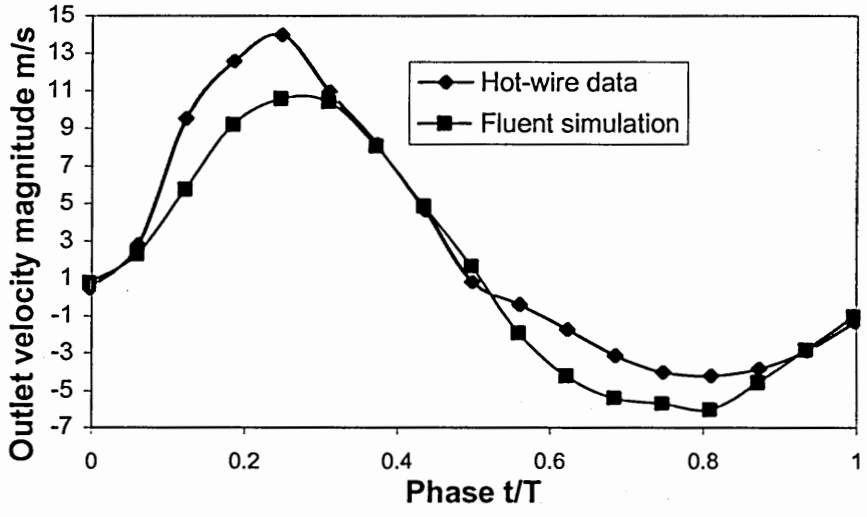

Figure 60. Tangential ACS phase-averaged maximum velocity magnitude in one cycle at the position of 0.8 mm away from the outlet, rectangular orifice of 10 mm×1 mm, frequency=100 Hz, and coil driving current 70 mA

4.4.1 Simulation Model Setup

In Fluent, the governing equation for energy conservation is Equation (37):

$$\frac{\partial}{\partial t}(\rho E)+\frac{\partial}{\partial x_i}(u_i(\rho E+P))=\frac{\partial}{\partial x_i}(k_{eff}\frac{\partial T}{\partial x_i}-\sum_{j'}h_{j'}J_{j'}+u_i(\tau_{ij})_{eff})+S_h \tag{37}$$

$$E=h_g-\frac{P}{\rho}+\frac{u_i^2}{2} \tag{38}$$

$$h_g = \sum_{j'} m_{j'} h_{j'} + \frac{P}{\rho} \tag{39}$$

$$h_{j'} = \int_{T_{ref}}^{T} C_{p,j'} dT \tag{40}$$

where k_{eff} is the effective thermal conductivity, $J_{j'}$ is the diffusion flux of the species j', τ_{ij} is the subgrid scale stress defined by Equation (25). The first three terms on the right hand of Equation (37) represent energy transfer due to conduction, species diffusion, and viscous dissipation, respectively. S_h includes heat of chemical reaction and any other volumetric heat sources, h_g is enthalpy of ideal gases, $m_{j'}$ is the mass fraction of species j', T_{ref} is 298.15 °K.

In this study, a silicon based heater array is used for cooling performance test. The heater is adhered to the printed wiring board substrate. Then the I/Os on chip are wire bonded on the copper patterns coated on a substrate board to connect off board power supplies and testing equipments. This board is 1.6 mm in thickness, 76 mm in width, and 48 mm in length. The board is attached on the ACS substrate to perform the cooling test. When the cooling test is conducted at different locations of the jet downstream, the board is simply moved to the desired location and the gap between the jet outlet and heater substrate is filled with another piece of printed wiring board of the same thickness (i.e. 1.6 mm). With this experiment setup, when the DC current is supplied to the heater, the heat generated from the chip is dissipated from the top surface by heat convection and the

bottom surface by heat conduction. Thus, both conduction and convection should be considered in the simulations.

To account for heat conduction, the physical model should include the substrate. In the prior section, when the fluid mechanics model is investigated, the model is applied only in the region where jet flow occurs (i.e. the cavity, the fluidic channel and the virtual dome). However, to explore the heat transfer phenomena, three solid regions should be added. The first region is the heater which is the heat source; the second one is the heater board where the heater is sitting; the third part is the ACS substrate where the heater board is attached. Hence, the physical model has two material states: fluid and solid. The model illustrated in Figure 61 is the tangential ACS testbed structure with fluidic channel 2 (channel width of 5.08 mm). All the volumes in the model should be meshed. In the simulations, approximately 150,000 meshed nodes are used.

Since different materials are involved in the simulations, the determination of the material physical properties is important. In the fluid mechanics modeling, only air is applied in the flow field. Its room temperature properties are employed in the simulations. In heat transfer modeling, for simplicity, the room temperature properties are used as well. It should be noted that air properties i.e. density, specific heat, thermal conductivity and viscosity vary with temperatures. However, accurate expressions of the variations at different temperatures are not available, and the introduction of such temperature dependent variables into the simulations may cause the calculation to become more complicated. Table 11 demonstrates the thermophysical properties of air at 20 °C and 100 °C (Chapman, 1987). In the worst scenario, this property is off by 22%.

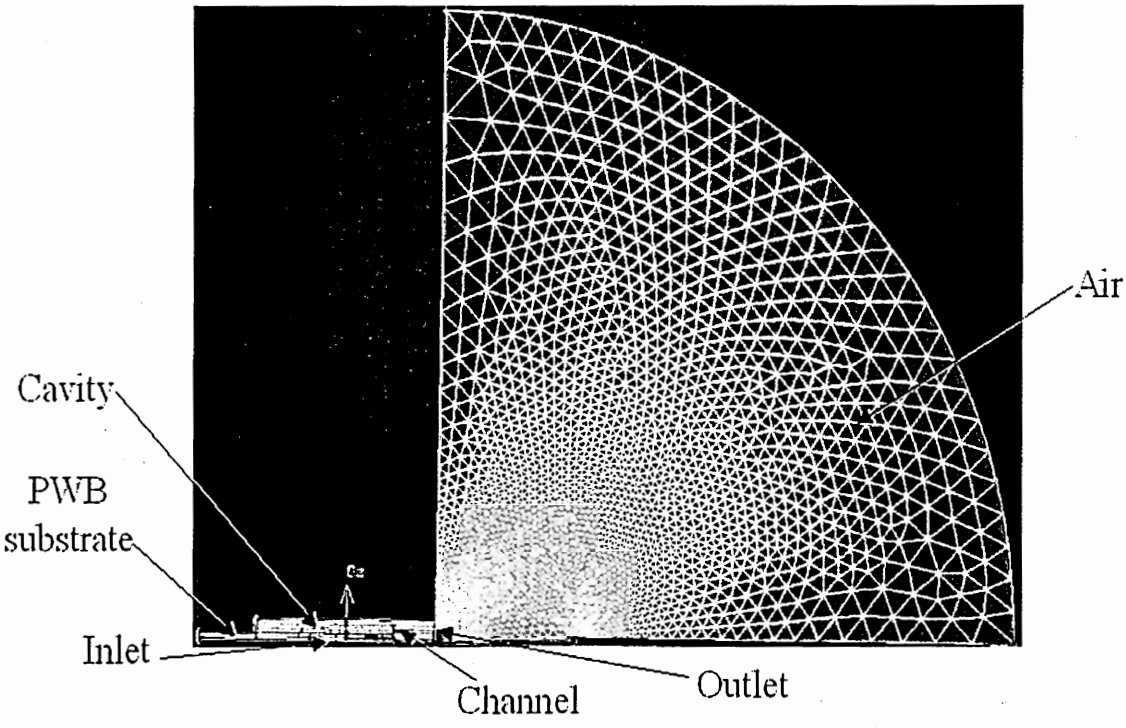

Figure 61. CFD model for heat transfer simulation

There are three other solid materials. The heater is silicon based, thus silicon material properties are used. The ACS PWB substrate is a FR4 (flame retardant) epoxy glass fiber composite material. From literature (Tummala, 2001), its thermal conductivity is about 0.23 W/m·K, specific heat is 1000 J/kg·K, and density is 1500 kg/m^3 at room temperature. Physical properties of FR4 epoxy glass fiber may vary with temperature. However, the data at temperatures other than room temperature are not available. Thus, the room temperature properties are applied in the simulations. The heater board is different from the PWB substrate due to the copper trace pattern on the board which can change the value of the thermal conductivity. The thermal conductivity is corrected by Equation (41) (Sergent, et al., 1998):

$$k_{SUBS} = \frac{0.25t_B + 13.65C_c t_t}{t_B} \tag{41}$$

Where k_{SUBS} is the thermal conductivity of the substrate, t_B is the substrate thickness in mm, C_c is the decimal percent conductor coverage, t_t is the trace thickness in oz (1 oz =35.6 microns) of copper. On the heater board, the copper trace has the thickness of 22 microns and covers about 50% of the board area. The board thickness is about 1.6 mm. Thus, the thermal conductivity of the board is calculated to be about 3 W/m·K.

Table 11. Properties of dry air at atmospheric pressure

Temperature °C	Specific heat kJ/kg·°C	Density kg/m^3	Viscosity $\times 10^6$ kg/m·s	Thermal conductivity $\times 10^3$ W/m·°C
20	1.0061	1.2042	18.17	25.64
100	1.0113	0.9460	21.78	31.27
Difference based on 20 °C	0.52%	21%	20%	22%

Boundary conditions on this model are similar to those for the fluid mechanics simulations. The input velocity boundary condition is applied on the vibrating diaphragm, and the atmospheric pressure condition is applied on the outside wall of the added dome. One more thermal boundary is added at the heat source. During the cooling performance test, the current through the heater and the voltage drop are monitored. Thus the power consumption on the heater (i.e. the heat generated by the heater) is known. In Fluent, this boundary condition is defined as the heat generation rate which is calculated by the power consumption density. All the interfaces between the solid (e.g. PWB) and fluid (e.g. air) are defined as the coupled walls. The substrate outside walls exposed to the stationary air are defined as the walls with natural convection. The same turbulence model, large eddy simulation, is selected to carry out the simulations.

4.4.2 Simulation Results

Initially the fluid mechanics and heat transfer calculations were performed at the same time. However, it was determined that the simulations take a long time to achieve a convergent result. With the meshed nodes of 150,000, and simultaneous performance of fluids transport and heat transfer simulations, it takes more than 30 minutes to finish one time step. If one cycle is divided into 16 time steps, it will take at least 8 hours to complete one cycle. If the power input to the heater array is changed, it takes at least 15 minutes for the system to reach a steady state. Based on the 15-minute response time and the one vibration period of 0.01 seconds, it will take 90,000 cycles, or 720,000-hour computational time to reach a steady state. This is not practical. It is believed that the long thermal conduction time causes the convergence problem.

In this research, a convergence acceleration approach, addition of complexity, is applied. This improves the solver performance by sequentially imposing the required complexities in the problem. For the fluid mechanics and heat transfer problems, the heat conduction is a time limiting step if the two calculations are performed simultaneously. As a result, heat transfer can be carried out first without fluid mechanics. After certain time (i.e. 625 seconds was used in these simulations), fluid mechanics is added to the calculation and both of them are conducted simultaneously. This approach can dramatically reduce the heater temperature ramping up time, and speed up the convergence process without losing the accuracy. Note that this addition of complexity approach exactly matches the experimental sequences. First, the heater is heated up without the jet; second, the jet is turned on and the system reaches a steady state. By applying the addition of complexity approach, the simulations can be completed much more rapidly.

As with the fluid mechanics simulations, the grid and time step independence tests are performed. 150,000 meshed nodes and 16 time steps per cycle can show satisfactory results which ensure the grid and time step independent. Due to the use of the addition of complexity approach, the first time step has a long time interval (i.e. 625 seconds). Then starting from the second time step, the time interval is reduced down to 0.000625 seconds to capture the detailed periodic fluid physics of the synthetic jets. To increase the accuracy, a 3-D double precision solver is applied to perform the fluid mechanics and heat transfer combined simulations.

During the course of the simulations, two variables are monitored. One is the local average heat transfer coefficient on the top surface of the heater array. The other one is

the centerline velocity magnitude at 0.8 mm away from the jet exit. The results are shown in Figure 62 and Figure 63, respectively. From both figures, it is observed that the simulation results become convergent almost after the first cycle. The local heat transfer coefficient has a small fluctuation within one cycle. The average is about 97 $W/m^2 \cdot K$. The experimental value from infrared thermography is about 80 $W/m^2 \cdot K$. The discrepancy is about 21% which is acceptable. The discrepancy may be a result of the assumed temperature independence of the materials properties. The room temperature assumption "exaggerates" the cooling capacity of the air jets (i.e. in reality the air is heated as it passes above the heater). That may be why the simulated heat transfer coefficient is higher than the experimental result. In addition, the incompressible gas assumption may not be accurate for the gases existing in the cavity. The error induced from the fluid mechanics simulations and the inherent errors from the model and the solver scheme can also lead to the discrepancy.

Figure 63 illustrates that the centerline velocity magnitude is cycling periodically. The simulation results are also compared with the experimental data as shown in Figure 64. There are a good match at the impingement stroke, and a larger discrepancy at the intake stroke. This is acceptable because the major contribution of the heat dissipation is from the impingement stroke.

The heat transfer simulations can be compared with the experimental data by the temperature distribution. Figure 65 shows good agreement between the simulations and the experiments on the temperature distribution along the centerline of the board top surface. The origin point is located at the center of the cavity. This temperature

comparison plus the local heat transfer coefficient data verify that heat transfer simulations also have the ability to reflect the experimental data.

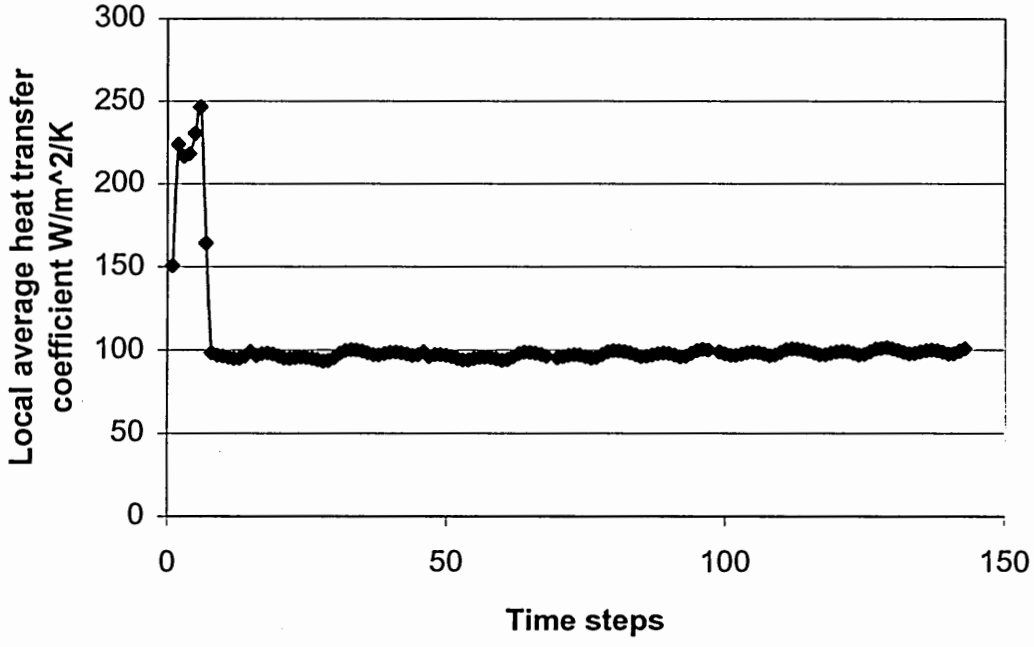

Figure 62. Local average heat transfer coefficient on the heater during the simulation for testbed with fluidic channel 2

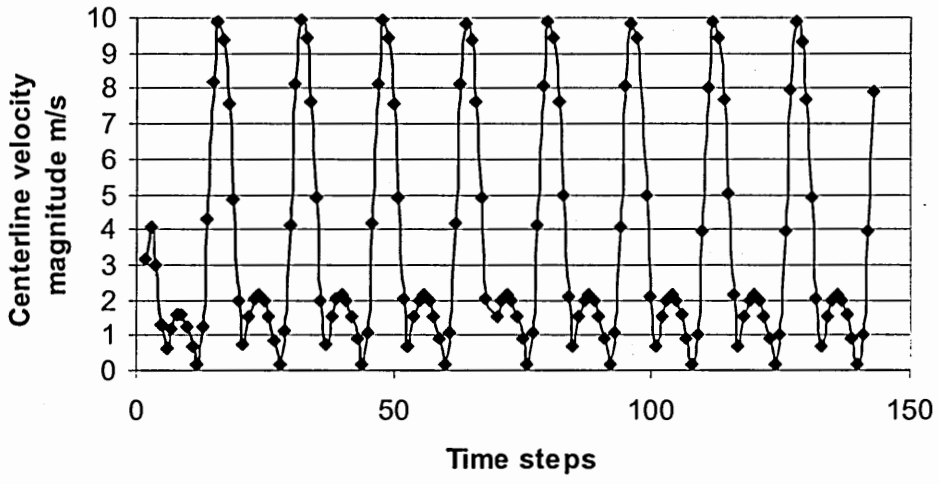

Figure 63. Centerline velocity magnitude at the location of 0.8 mm away from the exit during the simulation process for testbed with fluidic channel 2

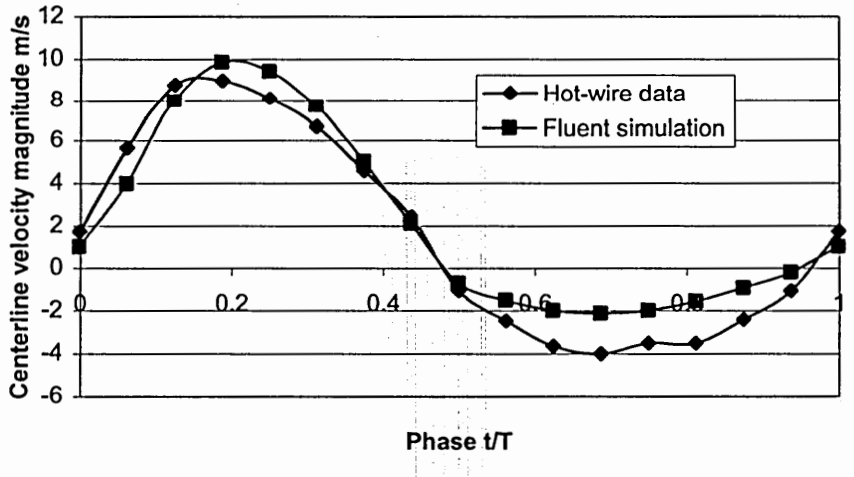

Figure 64. Comparison between Fluent simulation and hot-wire measurement for testbed with fluidic channel 2 (w=*5.08* mm)

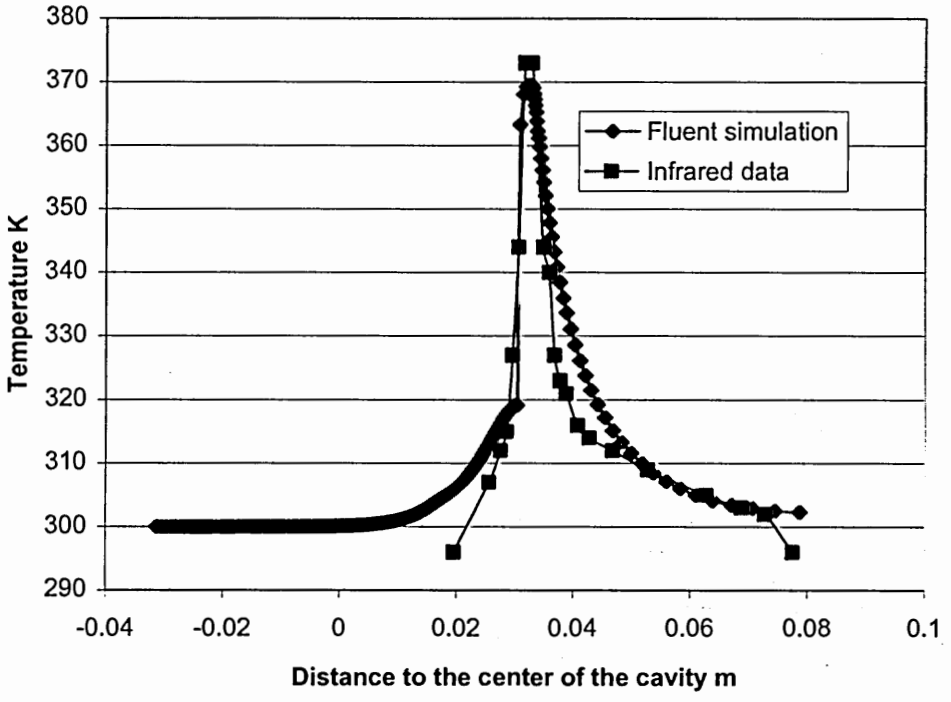

Figure 65. Comparison of temperature distribution on the device top surface for testbed with fluidic channel 2 (w=*5.08* mm)

CFD simulations can facilitate the understanding of the fluid mechanics. For instance, the vorticity Ω is easy to be calculated in the simulation tool. The vorticity is a point function, equal to twice the average angular velocity of a fluid particle. It is related to the spatial derivatives of the velocity by Equation (42):

$$\Omega = curl(u) \tag{42}$$

The flux of vorticity, circulation Γ, is an important derived quantity for vortex dynamics. It can be calculated by Equation (43):

$$\Gamma = (1/2)\int_0^T u^2 dt \tag{43}$$

Figure 66 shows the time development of the vorticity over one simulation cycle. Different colors denote the magnitudes of the vorticity. *t/T=0* is the starting point of a vibration cycle. *t/T=0.25* is the full impingement stroke. It seems there is a pair of vortices starting to form at the exit. Highest vorticity is at the near exit region. *t/T=0.5* is the midpoint of a cycle. The upper vortex still propagates to entrain more air into it. However, the lower vortex is strongly stretched due to the blockage of the heater board. It can be observed that the lower vortex helps break up the boundary layer and form a high vorticity region at the downstream of the exit (about 6 mm away from the exit). *t/T=0.75* is the full intake stroke. There is still a high vorticity region at the downstream close to the heater board. The high vorticity regions facilitate heat removal. From this perspective, it is easy to explain why there are a primary optimal cooling zone close to the exit and a secondary optimal cooling zone at the downstream of the exit. The conclusions exactly match the experimental results (Figure 45).

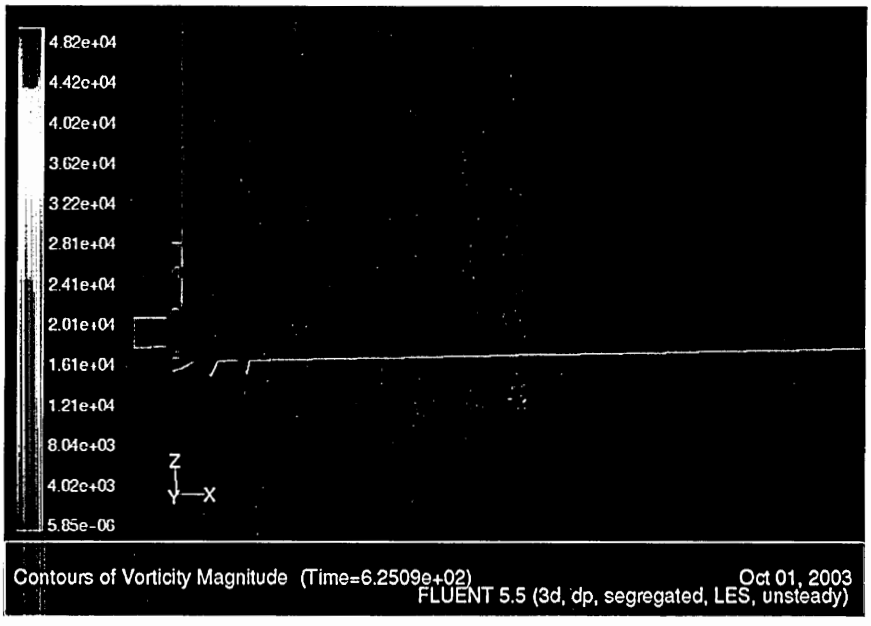
4.82e+04
4.42e+04
4.02e+04
3.62e+04
3.22e+04
2.81e+04
2.41e+04
2.01e+04
1.61e+04
1.21e+04
8.04e+03
4.02e+03
5.85e-06
Z
Y
X
Contours of Vorticity Magnitude (Time=6.2509e+02)
Oct 01, 2003
FLUENT 5.5 (3d, dp, segregated, LES, unsteady)

(a) *t/T=0*

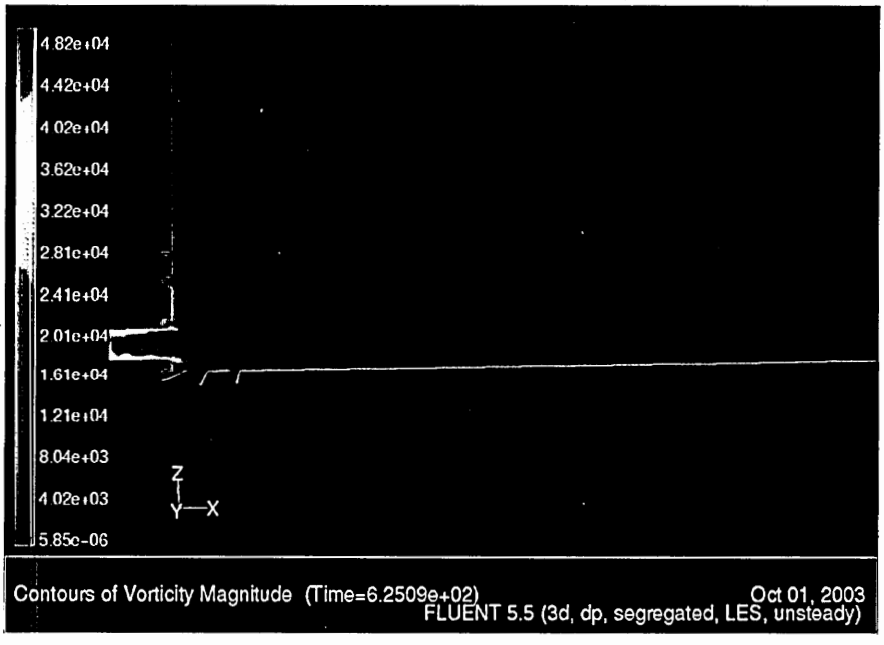
4.82e+04
4.42e+04
4.02e+04
3.62e+04
3.22e+04
2.81e+04
2.41e+04
2.01e+04
1.61e+04
1.21e+04
8.04e+03
4.02e+03
5.85e-06
Z
Y
X
Contours of Vorticity Magnitude (Time=6.2509e+02)
Oct 01, 2003
FLUENT 5.5 (3d, dp, segregated, LES, unsteady)

(b) *t/T=0.25*

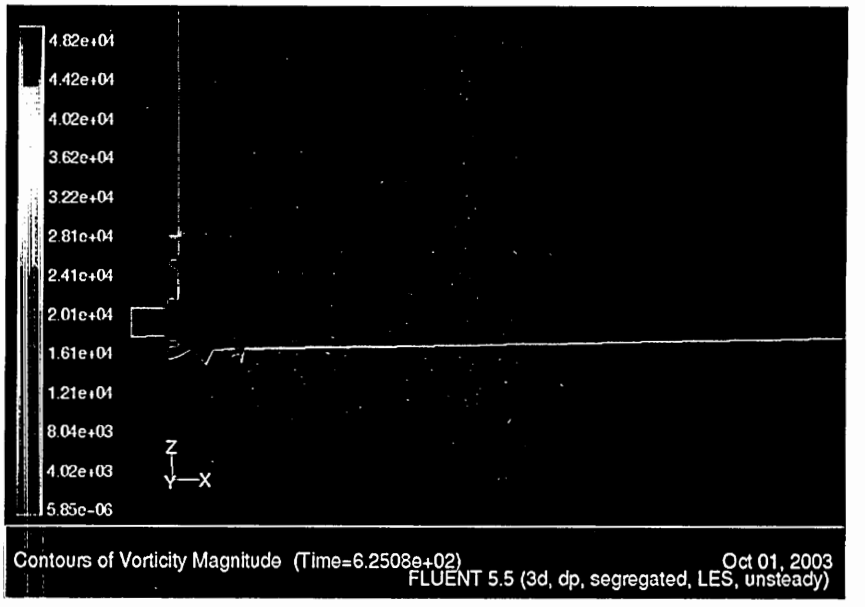

(c) *t/T=0.5*

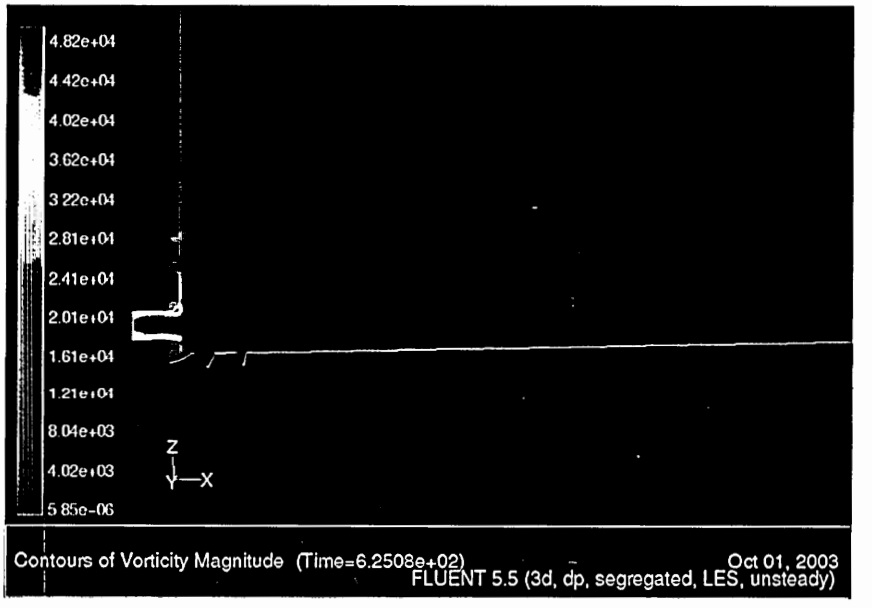

(d) *t/T=0.75*

Figure 66. Time evolution of the vorticity in a simulation cycle

4.4.3 CFD Predictive Model

One major application of CFD simulations is to use the developed model in the engineering predictions. The model developed in the prior work is applied to predict the behavior of another testbed structure, fluidic channel 5, in this section.

The testbed ACS with fluidic channel 5 is drawn as the real dimensions, meshed with about 150,000 nodes. The velocity boundary condition is defined in the same way as discussed in section 4.3. The material properties, LES turbulence model, and the addition of complexity solving approach are the same as the previous section. Figure 67-70 present the simulation results. Figure 67 and Figure 68 demonstrate that after the first cycle, the simulation is stabilizing to a convergent result. Figure 69 shows the centerline velocity magnitude comparison at 0.8 mm away from the exit. Figure 70 is the temperature distribution comparison on the top surface of the ACS substrate. All the comparisons show consistent results with the experiments. The final local average heat transfer coefficient on the heater is about 123 $W/m^2 \cdot K$. The experimental result is 127 $W/m^2 \cdot K$ which is a good match. Therefore, this simulation case verifies that the CFD approach can be employed to predict the synthetic jet behavior.

To obtain more confidence on the CFD predictive model, it is applied to simulate the cases further downstream of channel 5. In the experiments, the heater is positioned at variety of distances away from the jet outlet (see Table 12). In each case, the region between the jet outlet and the heater is uncladded (i.e. copper) PWB. This will change the thermal conductivity of the heater board because the copper pattern surface coverage is changed. The thermal conductivity can be calculated again according to Equation (41).

The calculated results are listed in Table 12. All the other material properties and the boundary conditions are same as before.

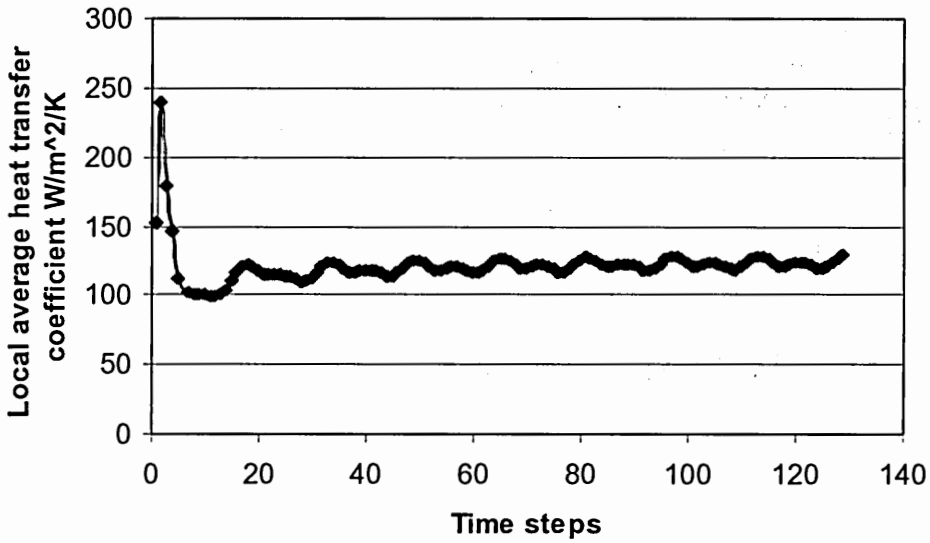

Figure 67. Local average heat transfer coefficient on the heater during the simulation for testbed with fluidic channel 5

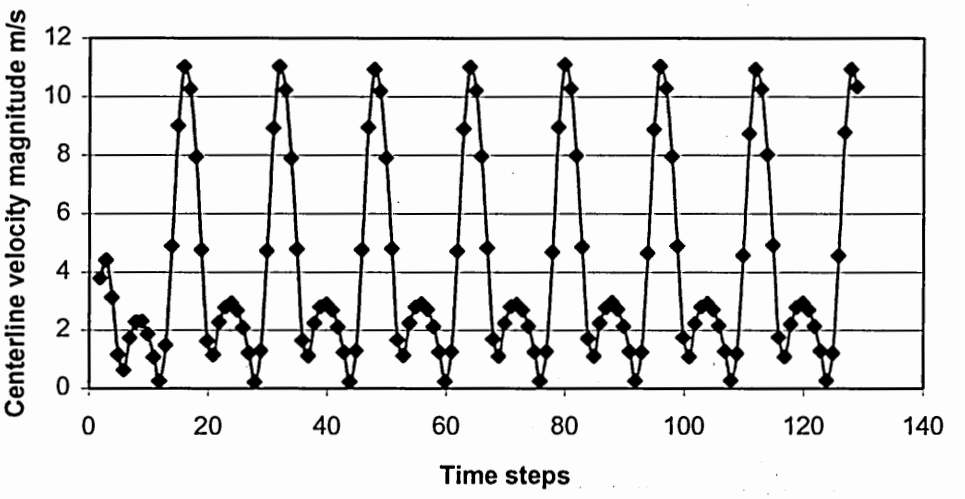

Figure 68. Centerline velocity magnitude at the location of 0.8 mm away from the exit during the simulation process for testbed with fluid channel 5

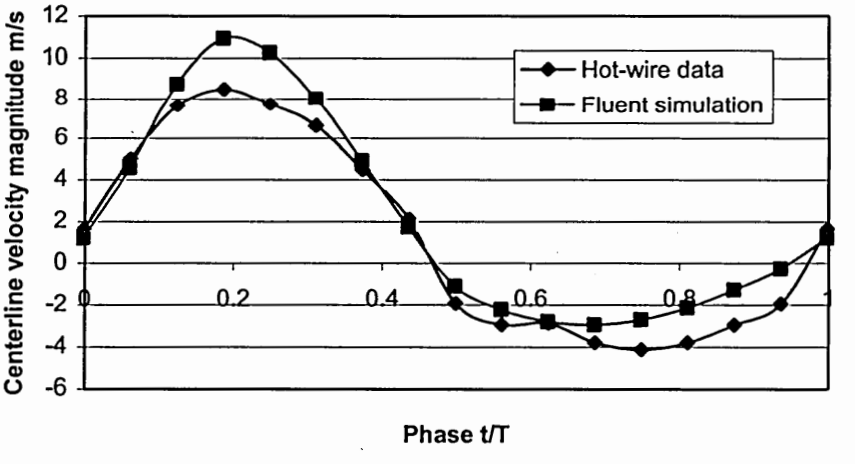

Figure 69. Comparison between Fluent simulation and hot-wire measurement at 0.8 mm away from exit for testbed with fluidic channel 5 (*w=10* mm)

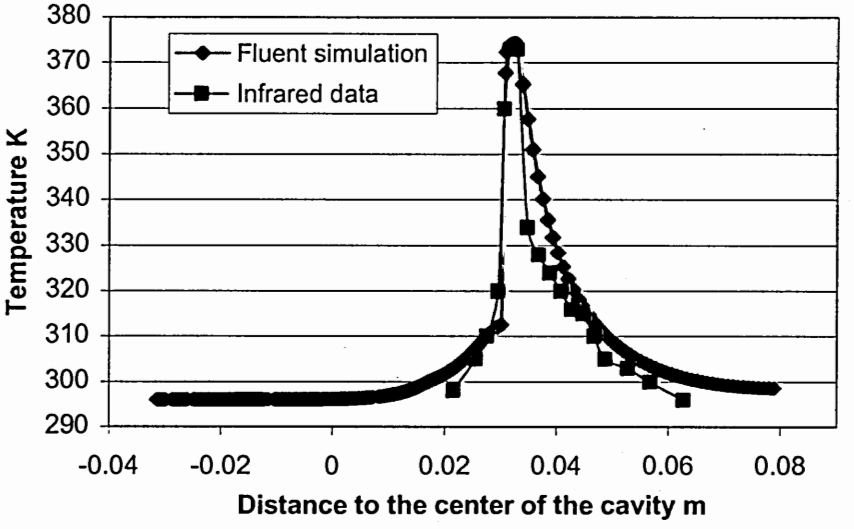

Figure 70. Comparison of temperature distribution on the device top surface for testbed with fluidic channel 5 (*w=10* mm) when heater is 0.8 mm away from the exit

Table 12. Thermal conductivity of the heater board

Heat distance to jet exit (mm)	0.8	4.23	6.35	10.16	15.24
Copper pattern coverage (%)	50	47	44	40	38
Thermal conductivity (W/m·K)	3	2.8	2.6	2.3	2.2

Figure 71-74 show the temperature distribution comparisons when the heater is located at 4.23 mm, 6.35 mm, 10.16 mm and 15.24 mm away from the exit, respectively. All the four simulation cases have good consistency with experimental results. The local heat transfer coefficients are compared in Figure 75 for all the five cases of channel 5. The overall discrepancy is approximately 25%. Once again the CFD predictive model is proved to be valid.

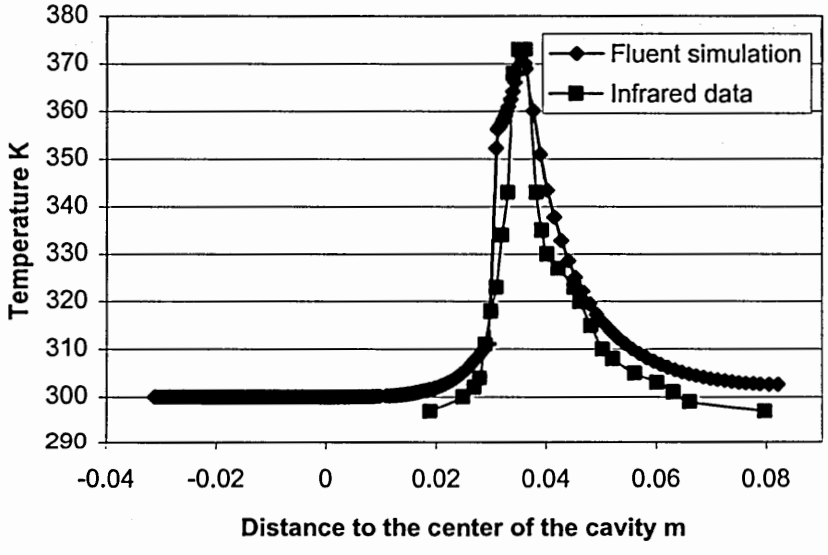

Figure 71. Comparison of temperature distribution on the device top surface for testbed with fluidic channel 5 ($w=10$ mm) when heater is 4.23 mm away from the exit

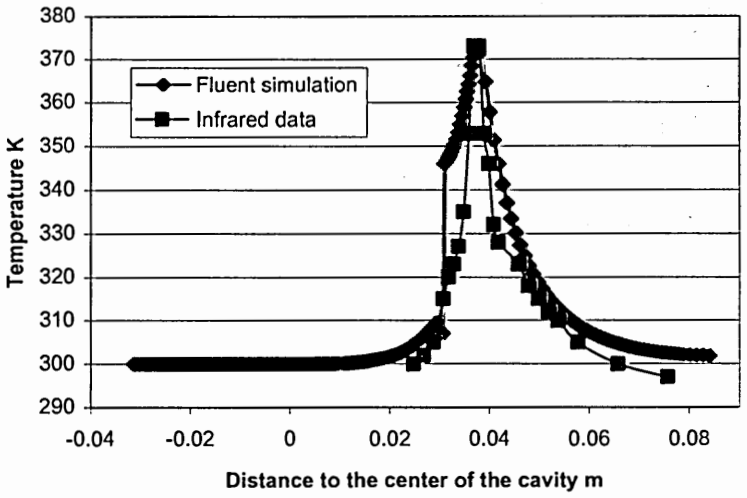

Figure 72. Comparison of temperature distribution on the device top surface for testbed with fluidic channel 5 (*w=10* mm) when heater is 6.35 mm away from the exit

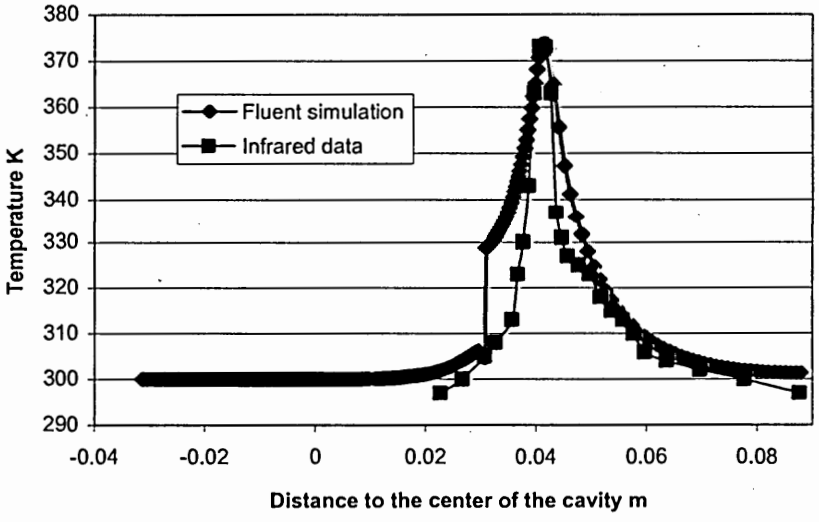

Figure 73. Comparison of temperature distribution on the device top surface for testbed with fluidic channel 5 (*w=10* mm) when heater is 10.16 mm away from the exit

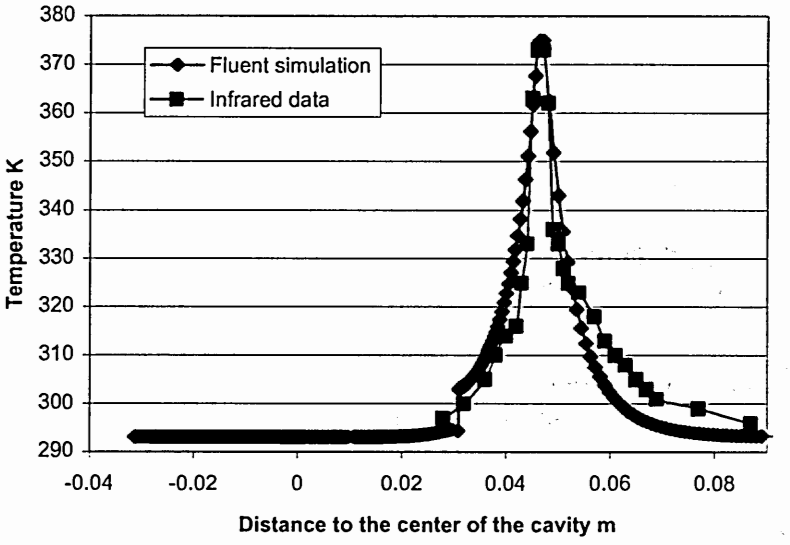

Figure 74. Comparison of temperature distribution on the device top surface for testbed with fluidic channel 5 (*w=10* mm) when heater is 15.24 mm away from the exit

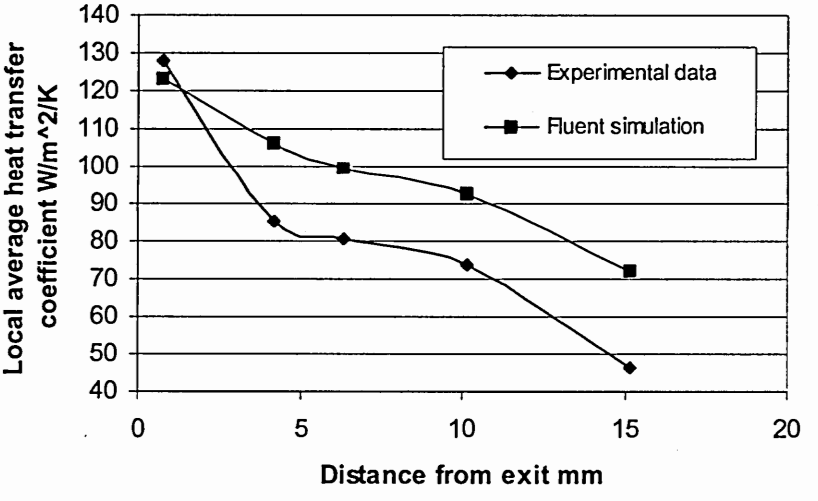

Figure 75. Local average heat transfer coefficient comparison for testbed with fluidic channel 5 (*w=10* mm)

4.5 Summary

CFD can provide a better understanding of the fluid physics. Some information which can not be directly observed from experiments (i.e. the vorticity contour) can be easily obtained from the simulation results. It can also provide satisfactory predictions to some complex fluid phenomena which seem impossible to the analytical approaches.

In this study, CFD software, Fluent, is employed to solve the complicated synthetic jet fluid mechanics coupled with heat transfer problem. To accomplish the numerical simulations, some necessary simplification assumptions are applied. The vibration diaphragm boundary condition is simulated as a sine wave velocity boundary. The physical properties of air and PWB are assumed to be temperature independent. The LES turbulence model is used instead of a direct numerical simulation. All the simplifications may result in some errors in the simulation results. However, the simulations still exhibit satisfactory accuracy. The convergence acceleration scheme, addition of complexity, has the advantages of both shorter computation time and higher accuracy. Addition of complexity allows the simulations to be accomplished in a reasonable computation time. Therefore, this chapter provides a valid and practical CFD numerical approach to solve the synthetic jet fluid mechanics and heat transfer problem.

Chapter 5

CONCLUSIONS AND FUTURE WORK

In this research, the synthetic jet technology is implemented in a printed wiring board substrate (a multilayer epoxy prepreg board) to enhance thermal management of the microsystem packaging. A microfluidic device embedded into the PWB is fully compatible with the lamination process to realize mass production. Due to its active heat convection feature, the microfluidic structure is called an active cooling substrate.

The vibrating diaphragm is the "heart" of the device to pump air in and out of the cavity. A polymeric diaphragm is developed and driven by electromagnetic force. A corrugated structure is molded into the diaphragm. In contrast to the traditional flat diaphragm, the corrugated polymeric diaphragm is more sensitive to the external force. Less force is required to generate a larger deflection. The optimal frequency is obtained for the diaphragm design. Lower frequencies are possible for the vibration system to minimize the noise level. Therefore, low power consumption, low noise, and larger deflection are the main features of the polymeric diaphragm.

The application of the MEMS device is for thermal management in electronic system packaging. Saving the "real estate" on the PWB board is one of the targets. Therefore the device is fabricated in the thickness of the board. Jet outlets are facing the heat generating components. Other electrical components can be surface mounted on the area embedded the ACS device to make full use of the board footprint.

Two different synthetic jet orientations have been prototyped. The first design is the vertical ACS with the jet impinging vertically. This orientation facilitates the fresh air entrainment due to the vortex rings generated at the jet outlet. However, the hot chips have to be flipped and mounted above the jet exit which may suppress the low-profile design. The second design is the tangential ACS with the jet blowing horizontally. With the tangential orientation, the hot chips can be mounted on the same substrate as the ACS device. A low profile design is ensured. The jet can only entrain the fresh air from the upper space, since the lower half space is blocked by the substrate. At the beginning of the impingement cycle, there are vortex pairs at the jet exit. The lower vortex tapers off downstream of the jet exit which disturbs the boundary layer close to the substrate surface. The upper vortex develops and entrains more air into the jet core. Therefore, the tangential ACS has a good combination of boundary layer disturbances and air entrainments which dramatically reduce the temperature gradient and enhance the heat convection.

The fluidic channel optimization is also performed. The optimal channel width is obtained. Two optimal cooling locations are identified. The primary optimal cooling zone is near the exit region. The secondary optimal cooling zone is located downstream of the exit. The hot components can be placed at the two locations depending on the dimensions of the heat generating components. With the optimal design and optimal location, the local heat transfer coefficient can reach 140 $W/m^2 \cdot K$. If the temperature difference between the designated heater array (with surface area of 9.6 mm^2) and the bulk air is 77 °C, the heat removed from the top surface by convection is approximately 103 mW. This is due to the contribution of the synthetic jet forced heat convection. The

amount of heat removed by the jets is about one fourth of the total heat dissipated by the heater array. Therefore, the synthetic jets significantly enhance the local heat convection.

CFD simulations are conducted on the ACS device to achieve theoretical understanding of the fluid behavior. The velocity boundary condition, the large eddy simulation turbulence model and the addition of complexity technique are the three key components of this complex simulation problem. They help to simplify the vibrating diaphragm boundary condition, provide accurate simulation results and make the simulations computationally practicable, respectively. Based on the simulations, a better understanding of the fluid physics and additional information which are not accessible from the experiments are obtained. The impacts of the fluid mechanics on the heat transfer are investigated. The CFD numerical model is available to predict the heat transfer performance with certain fluid mechanics conditions.

The final goal of this research work is to develop a methodology to fulfill other thermal engineering application by using the synthetic jet technology. Figure 76 illustrates the idea. The research work is conducted in the forward direction of the block diagram. First, the MEMS device is designed and fabricated. Then the fluid mechanics are characterized. Finally the heat transfer performance is evaluated. There are two bridges to connect these three "islands" to form an integrated system. Each bridge has two routes. One is an empirical method; the other is a numerical solution. For instance, the characteristic Equation (3) and ANSYS simulation tool are applied to design the diaphragm structure to realize certain volumetric flow rate or velocity requirement for the ACS device. The dimensionless group analysis Equation (17) and Fluent simulation tool are employed to find the relationship between the fluid mechanics and heat transfer. In

the future application, the block diagram is used in a backward direction. First, certain heat removal goals are defined. Then the required synthetic jet fluid characteristics are derived. Finally the device is designed to meet the fluid targets. Empirical methods provide a coarse consideration of the design problem because they can reflect the trend of the design parameters while without great accuracy. The numerical tools are used to refine the design parameters and finalize the design. Then a sophisticated methodology can be developed for future thermal management application.

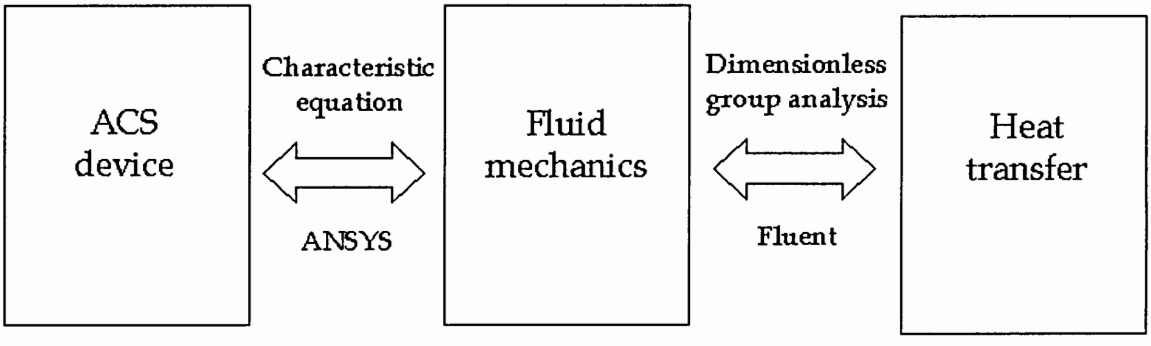

Figure 76. Block diagram of synthetic jet technology application methodology

An attractive feature of synthetic jet is that a small power input can induce a large influence on the fluid field. Thus, synthetic jets are good at providing on-demand local cooling. As microsystems become more compact, it is possible to shrink down the device size in order to remove heat from even more constraint volume. Microjet array design and one cavity multiple exit port design are some options to enhance the cooling

performance for multi modules. In addition, the synthetic jet technology can be implemented into other packaging components, i.e. heat sinks, to enhance their cooling functionality. Synthetic jets are a promising technology to enlarge the heat removal capability of the air-cooling thermal management approach.

REFERENCES

Arakawa, A., "Computational Design or Long-term Numerical Integration of the Equations of Fluid Motion: Two-dimensional Incompressible Flow", Part I. J. Comput. Phys., **1**, 119 (1966).

Chapman, A.J., "Fundamentals of Heat Transfer", Macmillan Publishing Company, New York, NY (1987).

Chen, Y., Scarborough, D., Liang, S., Aung, K., and Jagoda, J., "Manipulating Pattern Factor Using Synthetic Jet Actuators", 38th Aerospace Sciences Meeting & Exhibit, AIAA 2000-1023 (2000).

Chiric, V.A., Lee, T.T., and Rosales, J.L., "A Novel Cooling Enhancement in Microelectronic Devices and Systems Using Oscillatory Impinging Air Jets", Proceedings of 2001 ASME International Mechanical Engineering Congress and Exposition, IMECE2001/HTD-24391 (2001).

Coles, D., "Prospects for Useful Research on Coherent Structure in Turbulent Shear Flow", Proceedings of Indian Academy of Sciences, Engineering Sciences, **4** (2), 111 (1981).

Deardorff, J.W., "A Numerical Study of Three-dimensional Turbulent Channel Flow At Large Reynolds Numbers", J. Fluid Mech, **41**, 453 (1970).

Fan X., Zeng G., Croke E., Robinson G., LaBounty C., Shakouri A., and Bowers J. E., "n- and p-type SiGe/Si Superlattice Coolers", ITherm 2000 Conference Proceedings (2000).

Gallantree, H.R., Quilliam, R.M., "Polarized poly (vinylidene fluoride)- Its Application to Pyroelectric and Piezoelectric Devices", The Marconi review, Fourth Quarter (1976).

Gelsinger, P., "Microprocessors for the Millennium: Challenges, Opportunities, and New Frontiers", Proceedings of 2001 IEEE International Solid-State Circuits Conference, 22 (2001).

Germano, M., "Turbulence: the Filtering approach", J. Fluid Mech., **238**, 325 (1992).

Giovanni, M.D., "Flat and Corrugated Diaphragm Design Handbook", Marcel Dekker Inc., New York, NY (1982).

Horiuti, K., "Comparison of Conservative and Rotational Forms in Large Eddy Simulation of Turbulent Channel Flow", J. Comput. Phys. **71**, 343 (1987).

Jacobs, J., James, R., Ratcliff, C., and Glezer, A., "Turbulent Jets Induced by Surface Actuators", AIAA Shear Flow Conference, AIAA 93-3243 (1993).

Kim, S., and Lee, S., "Air Cooling Technology for Electronic Equipment", CRC Press, Boca Raton, Florida (1996).

Kraichnan, R.H.,"Eddy Viscosity in Two and Three Dimensions", H. Atmos. Sci., **33**, 1521 (1976).

Kral, L.D., Donovan, J.F., Cain A.B. and Cary, A.W., "Numerical Simulation of Synthetic Jet Actuators", 28th AIAA Fluid Dynamics Conference/4th AIAA Shear Flow Control Conference, 97-1824 (1997).

Lee, C.Y. and Goldstein, D.B., "Two-Dimensional Synthetic Jet Simulation", 38th Aerospace Sciences Meeting & Exhibit, AIAA 2000-0406 (2000).

Leonard, A., "Energy Cascade in Large-eddy Simulations of Turbulent Fluid Flows", Adv. Geophys., **18**A, 237 (1974).

Lilly, D.K., "On the Application of the Eddy Viscosity Concept in the Inertial Subrange of Turbulence", NCAR Manuscript, 123 (1966).

Moin, P., and Kim, J., "Numerical Investigation of Turbulent Channel Flow", J. Fluid Mech., **118**, 341 (1982).

Moore, G.E., "Cramming More Components onto Integrated Circuits", Electronics, **38** (8), 114 (1965).

Moran, R.P., Washabaugh, P.D., Muller, M.O., Bernal, L.P., Parviz, B.A., and Najafi, K., "Numerical Simulation of Micromachined Acoustic Resonators", 38th Aerospace Sciences Meeting & Exhibit, AIAA 2000-0546 (2000).

Perry, A.E., "Hot-wire Anemometry", Oxford University Press, New York, NY (1982).

Petukhov, B.S., "Heat Transfer and Friction in Turbulent Pipe Flow with Variable Physical Properties", Academic Press Inc., New York, NY (1970).

Rathnasingham, R., and Breuer, K., "Coupled Fluid-structure Characteristics of Actuators for Flow Control", AIAA Journal, **35**(5), 382 (1997).

Rediniotis, O., Ko, J., Yue, X., and Kurdila, A., "Synthetic Jets, Their Reduced Order Modeling and Applications to Flow Control", 37th Aerospace Sciences Meeting & Exhibit, AIAA99-1000 (1999).

Rizzetta, D.P., Visbal, M.R., and Stanek, M.J., "Numerical Investigation of Synthetic-Jet Flowfields", AIAA Journal, **37** (8), 919 (1999).

Savas, O. and Coles, D., "Coherence Measurements in Synthetic Turbulent Boundary Layers", J. Fluid Mech., **160**, 421 (1985).

Sedra, A., and Smith, K., "Microelectronic Circuits", Oxford University Press, New York, NY (1998).

Sergent, J.E., and Krum, Al, "Thermal Management Handbook for Electronic Assemblies", McGraw-Hill, New York, NY (1998).

Smagorinsky, J., "General Circulation Experiments with the Primitive Equations. I. the Basic Experiment", Month. Wea. Rev., **91**, 99 (1963).

Smith, B., and Glezer, A., "The Formation and Evolution of Synthetic Jets", Phys. Fluids, **10** (9), 2281 (1998).

Sobhan, C.B., and Garimella, S.V., "A Comparative Analysis of Studies on Heat Transfer and Fluid Flow in Microchannels", Heat Transfer and Transport Phenomena in Microsystems Conference Proceedings, (2000).

Steinberg, D., "Cooling Techniques for Electronic Equipment", John Wiley & Sons, Inc., New York, NY (1991).

Stuart, J., "Double Boundary Layers in Oscillatory Viscous Flow", J. Fluid Mech., **24**, 673 (1966).

Tummala, R., Rymaszewski, E., and Klopfenstein, A., "Microelectronics Packaging Handbook", Chapman & Hall, New York, NY (1997).

Tummala, R., "Fundamentals of Microsystems Packaging", McGraw-Hill, New York, NY (2001).

Unger, R.Z., Van der Walt, N.R., "Linear Compressor for Non-CFC Refrigeration", International Appliance Technical Conference Proceedings, (1996).

Wang, H., and Menon, S., "Fuel-Air Mixing Enhancement by Synthetic Microjets", AIAA Journal, **39** (12), 2308 (2001).

Westerveldt, P., "The Theory of Steady Rotational Flow Generated by a Sound Field", J. Accous. Soc. Am., **25**, 50 (1953).

Whitaker, S., "Forced Convection Heat-Transfer Correlations for Flow in Pipes, Past Flat Plates, Single Cylinders, Single Spheres, and Flow in Packed Bids and Tube Bundles", AICHE J., **18**, 361 (1972).

Wu, C-F, Murthy, J.Y., and Yao, S.C., "Embedded droplet impingement for integrated cooling of electronics", SPIE International Symposium on Micromaching and Microfabrication (1999).

Yoon, Y.K. and Allen, M.G., "Pt Heater/Sensor Microarray for Distributed Fluidic Cooling Assessment", Proceedings of 2001 ASME IMECE/MEMS-23894 (2001).

Yoshizawa, A., "Statistical Theory for Compressible Turbulent Shear Flows, with the Application to Subgris Modeling", Phys. Fluids, **29**, 2152 (1986).

VITA

Yong Wang was born in Zibo, P.R. China on April 8, 1975. In 1997, he graduated from Tianjin University with a B.S. degree in Chemical Engineering and a secondary B.S. degree in Industrial Engineering. In 1999, he graduated from Tianjin University with a M.S. in Chemical Engineering. Then he began his graduate studies in the school of Chemical & Biomolecular Engineering at the Georgia Institute of Technology. He received his M.S. degree majoring in Electrical and Computer Engineering in May 2003 and his Ph.D. in Chemical & Biomolecular Engineering in December 2003 under the advisement of Sue Ann Bidstrup and Mark Allen. He then joined the Industrial Application and Health Care Division in Praxair Technology Center at Tonawanda, New York.